The Dissertation Committee for Andreas Enevold Mogensen
certifies that this is the approved version of the following dissertation:

Real-Time Navigation for Mars Final Approach using the Mars Network

Committee:

E. Glenn Lightsey, Supervisor

Todd A. Ely

Wallace T. Fowler

David G. Hull

Cesar Ocampo

Real-Time Navigation for Mars Final Approach using the Mars Network

by

Andreas Enevold Mogensen, M.Eng.

DISSERTATION

Presented to the Faculty of the Graduate School of

The University of Texas at Austin

in Partial Fulfillment

of the Requirements

for the Degree of

DOCTOR OF PHILOSOPHY

THE UNIVERSITY OF TEXAS AT AUSTIN

December 2007

Acknowledgments

Real-Time Navigation for Mars Final Approach using the Mars Network

Publication No. _____

Andreas Enevold Mogensen, Ph.D.
The University of Texas at Austin, 2007

Supervisor: E. Glenn Lightsey

Real-time navigation during the final approach phase of an interplanetary mission can significantly increase the accuracy of aerocapture and pinpoint landing. The Mars Network is a versatile telecommunications network that is ideally situated to provide spacecraft-to-spacecraft radiometric navigation during Mars final approach and entry, descent, and landing via the Electra UHF transceiver, which is capable of providing autonomous, on-orbit, real-time trajectory determination using two-way Doppler measurements between a Mars approach vehicle and a Mars Network orbiter.

A detailed dynamic analysis and link analysis of the final approach problem is presented, which seeks to determine the expected operating conditions of the Electra transceiver. In particular, the maximum Doppler shift and Doppler rate, which determine the transceiver tracking loop requirements, and the total received signal power and signal-to-noise ratio, which determine

the range at which the communications link can be closed, are investigated for a range of Mars Network orbital geometries. A model of the Electra signal is developed on the basis of the results of the dynamic analysis and link analysis and is used as input to a high-fidelity simulation of the Electra transceiver. A Monte Carlo analysis is performed to determine the performance of the Electra transceiver for a range of signal and tracking loop parameters. In particular, the performance analysis focuses on the maximum range at which the link can be closed and on the acquisition and tracking performance of the second-order tracking loop.

The analysis of the tracking performance is used to characterize and model the error in the Doppler measurement of the Electra transceiver. The error model is incorporated into the design of an extended Kalman filter, in order to improve the fidelity of the navigation filter design. The information content in the Doppler measurement and the observability of the estimated states are investigated for various orbital geometries and the accuracy of the navigation solution is analyzed.

Table of Contents

List of Tables

List of Figures

xiii

Chapter 1

Introduction

1.1 Introduction to Interplanetary Navigation

Navigation for lunar and interplanetary missions has evolved considerably throughout the last five decades. The first space navigation system was created in January 1958 as a network of portable tracking stations deployed in Nigeria, Singapore, and California and run by the Jet Propulsion Laboratory (JPL) under contract to the U.S. Army [41]. The system was designed to track the first U.S. satellite Explorer 1. With the creation of NASA in October 1958, JPL was transferred from the Army to NASA and the system of tracking stations became a separately managed and operated facility, known as the Deep Space Network (DSN). The DSN became the backbone of deep space navigation systems for interplanetary missions, providing tracking, telemetry, and command services.

Historically, deep space navigation techniques for interplanetary missions have consisted of a combination of radio and optical techniques [59]. In the 1960's, interplanetary navigation for the Mariner missions to Venus (Mariner 2 in 1962 and Mariner 5 in 1967) and Mars (Mariner 4 in 1964 and Mariner 6 and 7 in 1969) consisted solely of DSN radiometric data, which

included Doppler and range data. These were planetary-flyby missions and the information content in the radiometric data, analyzed by Hamilton and Melbourne [26], was sufficient to support the single midcourse correction maneuvers necessary to achieve the navigation performance requirements. As the missions changed from flyby missions to orbiter and lander missions in the 1970's, the navigation performance requirements increased and additional tracking data were needed to augment the DSN radiometric data. The additional data were provided by optical navigation techniques, where images of the target body or one of its satellites taken against a known star background were used to determine the relative spacecraft position. This was first demonstrated in an optical navigation experiment flown on Mariner 6 and 7 in 1969 [14] and later, successfully used on Mariner 9 in 1971. Mariner 9, which was the first spacecraft to enter orbit about another planetary body, used TV images of Phobos and Deimos taken against a known star field to enhance the navigation solution during the Mars orbit insertion phase [4], [13], [31].

Determination of spacecraft angular position from DSN Doppler and range data can be problematic for certain orbital geometries and poorly-modeled force fields, even when long arcs of data are collected [59]. This led to the addition of very long baseline interferometry (VLBI) measurements to the services provided by the DSN in the early 1980's. VLBI provides a direct geometric measure of spacecraft angular position from simultaneous measurements of the signal arrival time at two DSN stations. When a single source, such as a spacecraft signal is tracked, the differential arrival time is referred to

as differential one-way range (DOR); when a second source that is infinitely far away, such as a quasar, is tracked simultaneously, the delay is referred to as delta differential one-way range (ΔDOR). VLBI measurements were used to navigate the Mars Observer mission in 1992, in addition to several outer-planet missions such as Voyager, Galileo, and Ulysses [59].

In general, interplanetary navigation is now a combination of radiometric techniques and optical techniques, depending largely on where the spacecraft is located along its flight path. Typically, Earth ground-based radiometric data from the DSN is used during the cruise phase, from the time of interplanetary transfer orbit injection until approach to the target body. The radiometric data is typically augmented by onboard optical data during the approach phase. The optical images provide a direct measure of the spacecraft position relative to the target body, which improves the navigation solution, especially in cases where there are large uncertainties in the target-body ephemerides. Notable exceptions to this include the Mars Pathfinder, Mars Climate Orbiter, and Mars Polar Lander missions, which relied solely on DSN radiometric tracking due to tight cost constraints [59].

In the future, interplanetary missions will face increasingly tight targeting requirements to enable high-accuracy aerocapture maneuvers and precision landings. Future navigation systems will have to meet requirements that, in addition to accuracy, include such issues as robustness, reliability, timeliness, and cost. Currently, GPS provides such a navigation system for missions in low and medium Earth orbit [22]. GPS and other spacecraft-to-spacecraft ra-

diometric tracking techniques, such as the cross-link ranging capability demonstrated by the Gravity Recovery and Climate Experiment (GRACE) mission [58], can be used for precise relative navigation of spacecraft in Earth-orbit, as described by Holt [29]. These navigation techniques can be extended to interplanetary missions during the approach phase, whenever another spacecraft is already in orbit about the target body, as described by Thurman and Estefan for the Mars approach problem [60].

This is the case at Mars, where there exists a network of science orbiters, called the Mars Network [7]. The Mars Network is capable of providing spacecraft-to-spacecraft radiometric navigation data using the Electra UHF transceiver [20]. The Electra is manifested as baseline equipment for current and future Mars missions, including the Mars Reconnaissance Orbiter (MRO) that arrived at Mars in 2006 and the Mars Science Laboratory (MSL) that is scheduled for launch in 2009. A key service of the Mars Network is to provide communications using the Electra during mission critical events. Indeed, future relay orbiters that will make up the Mars Network, such as MRO, will have budgeted maneuvering capability to ensure coverage for a Mars mission during its critical event [18]. By design, the Electra is also capable of collecting Doppler data concurrent with data transmission while the link is active. Furthermore, the Electra has been designed with spare processing and memory capabilities that can be utilized for higher level processing. This will allow the Mars Network to provide precision navigation services for other Mars missions during approach and entry, descent, and landing (EDL).

1.2 Motivation for Mars Approach Navigation

Scientific goals for the next decade of Mars exploration include searching for water and characterizing the aqueous processes on Mars, studying the mineralogy and weathering of the Martian surface, and searching for preserved biosignatures in Martian rocks [2]. Achieving these goals will require placing landers at predefined locations of the greatest scientific interest. In recognition of this fact, the Mars Technology Program at NASA has identified pinpoint landing as a key advanced EDL technology for future Mars landers [2]. Pinpoint landing is defined for the purposes of this discussion as landing within 1 km of a preselected target. The capability to land within 1 km of a predefined landing site will improve safety and enable landing within roving range of sites of scientific interest while avoiding hazardous areas.

Precise trajectory knowledge is required in order for a guidance system to achieve pinpoint landing [19]. This is true, in particular, during the mission's final approach phase and EDL phase when the spacecraft is actively guiding itself. The final approach phase is defined as the period from 12 hours prior to atmospheric entry up to the point just before entry at the top of the atmosphere. The different mission phases are illustrated in Figure 1.1, including the initial approach phase, the final approach phase, and the EDL phase. Navigation during the initial approach phase, which is defined as the period from 30 days prior to atmospheric entry and leading up to the final approach phase, is mostly an Earth ground-based activity since there is sufficient time to relay telemetry and uplink commands to the spacecraft. Accurate trajectory
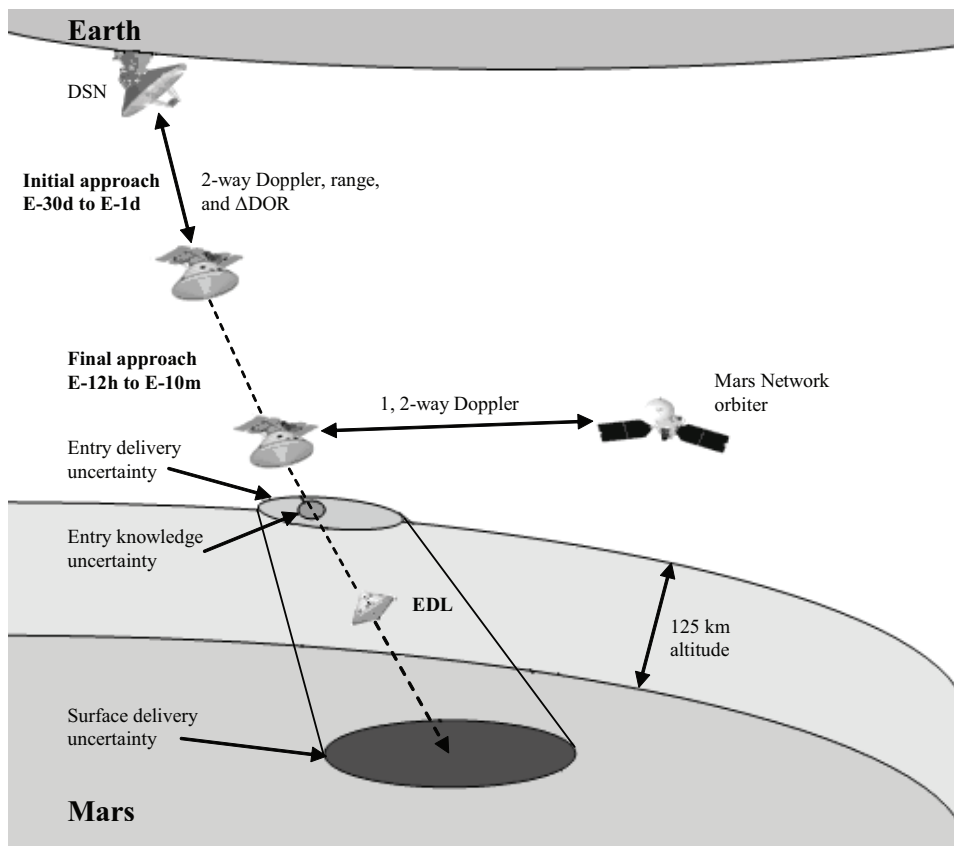
Figure 1.1: The final approach and EDL phases of a Mars mission with radio-metric tracking provided by the Mars Network (Credit: Ely [19])

knowledge during the initial approach phase is primarily useful for minimizing Mars targeting errors. It is during the final and most critical mission phases that precise trajectory knowledge provided to an onboard guidance system can be most useful for aiding pinpoint landing. However, the final mission phases are brief and must proceed without ground-based Earth support due to light-time delays. The implication is that trajectory knowledge updates past the

ground-based data cutoff, which is typically six hours prior to atmospheric entry, must be obtained in-situ and processed onboard.

The Mars Network is ideally situated to provide spacecraft-to-spacecraft radiometric navigation data that can be processed onboard the approaching spacecraft in real-time during the final approach and EDL phases [7], [27]. This will enable improvements in surface positioning error and improve the performance of entry guidance and aerocapture. Table 1.1 shows the performance of several navigation and guidance strategies for Mars landing [1]. The performance is given in terms of the size of the 3σ uncertainty ellipses. The current baseline strategy that uses only Earth ground-based radiometric data is represented in the first row, while an approach using Mars Network-based spacecraft-to-spacecraft radiometric data is represented in the second and third rows.

Note that in Table 1.1, entry knowledge uncertainty represents the trajectory uncertainty at the top of the atmosphere given the proposed tracking strategy stated in each row, while entry delivery uncertainty represents the trajectory uncertainty at the top of the atmosphere when the knowledge, up to a certain data cutoff time, is used with guidance. Also note that ballistic surface delivery represents an unguided entry, descent, and landing, such as was used on the Mars Exploration Rover (MER) missions. Finally, hypersonic guidance represents guidance in the upper atmosphere, while hypersonic and chute guidance represents guidance in the upper atmosphere and guidance while on the parachute.

7

Table 1.1: Atmosphere entry and surface delivery errors of a Mars lander for various tracking strategies (Credit: JPL [1])

Radio Navigation Capability	3σ Entry Uncertainty (km)		3σ Surface Delivery Uncertainty (km)			Comments
	Knowledge	Delivery	Ballistic (MER)	Hypersonic Guided Entry (MSL)	Hypersonic + Chute Guided Entry	
Ground-based X-band DSN radio-navigation (Doppler, Range, ΔDOR) with E-18 hr data cutoff, E-6 hr maneuver, and E-4 hr trajectory update.	1.5 × 1.5	9 × 1.5	80 × 12	10 × 5	10 × 5	Baseline tracking for MER and MSL. Chute guidance of no value without additional tracking
Row 1 with S/C to S/C UHF-band Doppler using the Mars Network. Autonomous processing begins at E-10 hr with maneuver at E-1 hr.	0.3 × 0.3	0.3 × 0.3	38 × 5	3 × 3	3 × 3	Improved entry knowledge improves MER and MSL case.
Row 2 with additional UHF data through EDL.	0.3 × 0.3	0.3 × 0.3	38 × 5	3 × 3	0.5 × 0.5	Improved entry knowledge with EDL navigation enabling for pinpoint landing.

The landing system used for the MER mission, shown in Table 1.1 as the three boxes in double outline, represents the current state of the art and yields final delivery error at the top of the Mars atmosphere of 9 km. These errors grow to 80 km at the surface of Mars since the MER entry is ballistic. Even with active guidance during entry, as is the case for the MSL mission, the surface delivery errors are on the order of 10 km and cannot decrease to less than the entry errors without further navigation sensor data that could consist of either in-situ radiometric tracking or optical navigation. In fact, to achieve pinpoint landing accuracies of less than 1 km requires that the approaching

spacecraft's guidance system has real-time trajectory updates at the same level of accuracy during final approach, unless the spacecraft has a significant fuel budget to allow for substantial maneuvers during EDL. Pinpoint landing that is aided by the Mars Network navigation data during both the final approach and EDL phases and integrated with active guidance is shown in the last row of Table 1.1. This case illustrates that final approach navigation is enabling for pinpoint landing for a system that minimizes fuel expenditures for maneuver during EDL.

1.3   Contributions

The goal of the Mars approach navigation task under the Mars Technology Program is to develop a real-time, embedded navigation filter for the Electra UHF transceiver to achieve 300-m or better atmosphere entry knowledge error, as highlighted in gray in Table 1.1. The resulting technology is enabling for pinpoint landing that minimizes maneuvering during EDL, as shown in the third row in Table 1.1. Ultimately, the navigation technology should be integrated with a spacecraft's onboard guidance system for complete closed-loop guidance and navigation. Doing so will achieve 300-m or better atmosphere delivery error.

The dissertation builds on the work of Thurman and Estefan [60], who extended the original radiometric navigation analysis of Hamilton and Melbourne [26] to examine the Mars approach navigation problem, and on the work of Ely [19], [20], Burkhart [11], and Quintanilla [43], who examined

the performance of a Mars approach and EDL navigation system based on the Mars Network's Electra UHF transceiver. The dissertation makes several general contributions to the field of spacecraft-to-spacecraft radiometric navigation, as outlined below. These contributions can be directly applied to the specific case of the Mars approach navigation task, mentioned above. In addition, the dissertation makes several contributions that are specific to the case of using the Electra UHF transceiver as a radiometric navigation sensor.

1.3.1 Orbital Dynamics Simulation Tool

A MATLAB simulation tool was created that models the generic target-body approach scenario. The orbital dynamics simulation tool facilitates the analysis of the relative approach dynamics between an approaching spacecraft and an orbiting spacecraft. The flexibility of the tool allows different model parameters, such as the target body, the orbital perturbations, and the orbital geometries, to be incorporated into the tool and their effects on the range rate, range acceleration, and Doppler shift analyzed. Furthermore, both the approaching spacecraft and the orbiting spacecraft are modeled as rigid bodies, which allows the effect of spacecraft attitude motion to be included in the analysis of the relative approach dynamics. Finally, the simulation tool includes an occultation model, which allows the periods of line-of-sight visibility between the approaching spacecraft and the orbiting spacecraft to be determined.

1.3.2 Link Budget Analysis Tool

A generic link budget analysis tool was created in parallel to the orbital dynamics simulation tool. The link budget tool determines the one-way or two-way link budget between a transceiver onboard an approaching spacecraft and a transponder onboard an orbiting spacecraft, given the range between the two spacecraft. The link budget tool allows the total received power and the signal-to-noise ratio (SNR) to be determined for various link parameters, including the transmitted power, the transmitter and receiver antenna gains, the data rate, and the tracking loop bandwidth. The tool includes a detailed model of the spacecraft attitude dynamics, which determines the off-boresight vectors, and a model of the antenna radiation patterns, which determines the antenna gain. This allows the interaction of the spacecraft attitude motion and the antenna gain characteristics, and their effects on the link budget to be investigated. Ultimately, the tool facilitates the analysis of the effect of the link parameters on the range at which the link can be closed and communication established between the two spacecraft.

1.3.3 Electra Modeling

The dissertation presents a detailed description of the Electra UHF transceiver and the high-fidelity MATLAB model of the Electra that was created by JPL. The numerous JPL Interoffice Memoranda that describe the Electra have, for the first time, been collected into a single comprehensive document that serves as a reference for the Electra MATLAB model. In addi-

tion, the dissertation verifies that the MATLAB model is in fact an accurate representation of the Electra flight design.

1.3.4 Electra Performance Analysis

The performance of the Electra transceiver is analyzed using the high-fidelity MATLAB model. In particular, the range at which the communications link can be closed and the ability of the Electra to acquire and track the transmitted signal during a Mars approach under the full range of dynamic operating conditions is analyzed. Realistic operating conditions, including the expected values of Doppler shift, Doppler rate, total received power, and SNR are determined from the orbital dynamics simulation tool and the link budget analysis tool. These results are then used in a Monte Carlo analysis to determine the acquisition and tracking performance for various signal and tracking loop parameters, such as the data rate, the data modulation scheme, and the tracking loop bandwidth.

1.3.5 Electra Error Modeling

The dissertation develops an error model of the Electra transceiver, when it is functioning as a navigation sensor. The error in the Doppler measurement is characterized and modeled for the first time based on high-fidelity receiver simulations. The tracking loop performance is analyzed using the high-fidelity MATLAB model and the dynamic response of the tracking loop is analyzed to determine the characteristics of the steady-state tracking error

as a function of the Doppler shift and the SNR. The analysis of the tracking error is used to develop a model of the mean error and the variance of the error in the two-way Doppler measurement as a function of the relative range between the approaching spacecraft and the orbiting spacecraft.

1.3.6   Navigation Filter Design

Finally, the dissertation develops an adaptive extended Kalman filter (EKF) that is suitable for the approach navigation problem. The Electra error model, based on the high-fidelity receiver simulations, is incorporated into the design of the EKF, in order to improve the fidelity of the navigation filter design. The resulting EKF design is adaptive, in the sense that the filter accounts for the changing characteristics of the Doppler measurement error as a function of the relative range. The information content in the Doppler measurement and the observability of the estimated states are investigated for various orbital geometries and the accuracy of the navigation solution for the adaptive EKF is analyzed and compared to that of a standard EKF.

1.4   Overview of Dissertation

The research work and the results are presented in the following chapters. Chapter 2 provides an overview of the concept of operations for using the Mars Network and the Electra UHF transceiver to support Mars approach navigation. The chapter defines the various approach scenarios and presents an analysis of the relative approach dynamics and the link budget for a range

of orbital geometries. Chapter 3 describes the Electra UHF transceiver in detail and documents the high-fidelity MATLAB model. The chapter analyzes the carrier tracking loop and the digital signal processing functions of the transceiver and describes the Electra measurements useful for navigation. Chapter 4 analyzes the performance of the Electra transceiver. The performance analysis is based on simulations of the Electra MATLAB model, using the results of the dynamic analysis and the link budget analysis, presented in the previous chapters. The chapter concludes with a description of the required hardware and experimental setup necessary to test the Electra engineering development unit (EDU) in the laboratory. Chapter 5 presents the development of an EKF that is appropriate for the Mars approach navigation problem. The chapter develops a model of the error in the Doppler measurement, which is incorporated into the EKF design, and analyzes the performance of the EKF. Finally, Chapter 6 summarizes the results and the contributions of the research and presents ideas for future work.

Additional information that is useful for understanding parts of the dissertation research is presented in the appendices. Appendix A presents an overview of the Electra modulation architecture, including the structure of the transmitted signals and the data encoding formats used by the Electra. Appendix B provides an introduction to the analysis of phase-locked loops (PLL) and Costas loops. The analysis focuses primarily on linear, continuous-time PLLs. Finally, Appendix C provides the partial derivatives that make up the Jacobian matrix that is used in the navigation filter.

Chapter 2

Concept of Operations

2.1 Introduction

The Mars Network is a telecommunications network that is in the process of being established around Mars [7]. The network will consist primarily of science orbiters, whose secondary mission is to serve as telecommunications relays, and possibly a dedicated telecommunications orbiter. The Mars Network will provide proximity telecommunications for increased science data return, critical event real-time telemetry capture, and navigation and timing services for in-situ navigation and surface positioning. Currently, the network consists of the 2001 Mars Odyssey orbiter, which carries the CE-505 radio developed by Cincinnati Electronics, and the 2005 MRO orbiter, which carries the Electra radio developed by JPL. Both orbiters contain enough propellant reserves to sustain operation through at least 2015 [3]. It is anticipated that future Mars missions, such as the 2009 MSL rover will carry some variant of the Electra radio, except for the 2007 Phoenix Mars lander, which for heritage reasons will carry the CE-505 radio.

The Electra is a programmable software-defined UHF radio that can be driven by an external oscillator, which for MRO is an ultra stable oscillator

(USO). The programmability extends from tracking loop design to onboard real-time measurement processing, making the device extremely flexible in its range of operation. The current Electra design features a space-qualified Sparc V-7 processor running at 24 MHz with 256 Mbits of storage and between 1 Mb (EEPROM) and 2 Mb (SRAM) of executable memory. It is estimated that about two-thirds of this processing and memory is available for use. The Electra radiates a binary phase-shift keying (BPSK) signal at varying output levels typically less than 10 watts as required for a particular mission. This can be accomplished in one of three modes: carrier-only, BPSK with residual carrier, and BPSK with suppressed carrier. Several forward error corrections schemes are available for use, including Manchester decoding for residual carrier operation and 3-bit soft decision Viterbi decoding for suppressed carrier operation. Data rates from 1 ksps to 2048 ksps are available.

The Electra can provide spacecraft-to-spacecraft radiometric navigation data between a Mars approach vehicle (MAV) and a Mars Network orbiter (MNO) by measuring the carrier phase of the Doppler shifted signal. The raw navigation measurement of the Electra transceiver is either one-way total count phase O^{1WTP} or two-way total count phase O^{2WTP} of the received carrier. The two-way total count phase is given by:

$$O^{2WTP}(t) = \phi^{tr}\big(t - \rho(t) - \delta_{2W}\big) - \phi^{tr}(t) - N \qquad (2.1)$$

where

$$
\begin{aligned}
\phi^{tr}(t) &= \text{Transceiver oscillator phase} \\
\rho(t) &= \text{Round-trip light time} \\
\delta_{2W} &= \text{Hardware delays} \\
N &= \text{Unknown phase ambiguity}
\end{aligned}
$$

In order to remove the unknown phase ambiguity, the one-way and two-way total count phase measurements are usually processed as integrated Doppler measurements that are the difference of two phase measurements separated by a specified count time T. For accurate integrated Doppler measurements, continuous tracking without cycle slips is required throughout the count time. It is the integrated Doppler observable that will ultimately be used in the navigation filter. The two-way integrated Doppler observable O^{2WID} is related to the two-way total count phase O^{2WTP} according to:

$$
O^{2WID}(t) = -\frac{O^{2WTP}(t) - O^{2WTP}(t-T)}{2\pi T} \tag{2.2}
$$

Note that in the actual filter implementation, the integrated Doppler observable is not divided by the count time T and is simply the difference of the two total count phase measurements. The measured count time is only approximate because the Electra clock will drift from the ideal count time T as the real clock progresses during the signal propagation. It is for this reason that the observable is not divided by the measured count time, as doing so would unnecessarily complicate the partial derivatives for the observable.

The Electra can operate in both a one-way and a two-way tracking mode. In the two-way tracking mode, a transceiver onboard the MAV trans-

17

mits a signal at 401 MHz to a transponder onboard the MNO that phase coherently retransmits the signal at 437 MHz back to the MAV, which then records the measurement. The advantage of the two-way measurement is that it eliminates the error contribution from the transponder's oscillator. The one-way measurement, on the other hand, includes error contributions from two independent oscillators, one on the transmitter and the other on the receiver. Full duplex communications with coherent two-way data is currently only supported when the Electra transceiver is on the MNO and the transponder is on the MAV or surface lander. Electra is capable of swapping transmit and receive bands, but is only able to do so in half-duplex mode, which does not support coherent turnaround [17]. This is primarily a software issue and it is anticipated that the capabilities of the Electra will be extended to support two-way Doppler measurements in either direction shortly.

2.2 Scenario Definition

A generalized software tool has been designed in MATLAB to simulate a planetary or lunar approach between an approaching spacecraft and an orbiting spacecraft. The tool will facilitate the characterization of the expected operating environment that the Electra transceiver will encounter during the final approach by analyzing the relative approach dynamics and link budgets. This will enable a high-fidelity signal model to be created, which will be used to assess the performance of the carrier tracking loop and characterize the error model associated with the Electra as a navigation sensor. The performance

18

Table 2.1: Nominal orbital elements of MSL, MRO, MGS, MOD, MEX, and MTO in Mars-centered inertial coordinates

Orbital Element	MSL	MRO	MGS	MOD	MEX	MTO
Semi-Major Axis (km)	−5432	3684	3781	3802	9354	8115
Eccentricity	1.617	0.010	0.007	0.009	0.607	0.464
Inclination (deg)	44.1	93.0	92.8	93.1	86.6	116.6
Longitude of Node (deg)	91.9	278.0	263.0	200.0	228.7	278.2
Argument of Periapsis (deg)	297.2	270.0	270.0	276.0	357.9	132.6

analysis used in this study is based on a standard Mars approach scenario for a representative MAV and several representative MNO's. Specifically, the analysis is based on the standard approach trajectory for the 2010 encounter at Mars between the MSL and MRO spacecraft. For purposes of comparison, several other potential MNO's will also be considered.

The MSL spacecraft, which will serve as the MAV in this analysis, is currently scheduled for launch in 2009 with arrival at Mars in the fall of 2010. Although the landing site has not been selected, analysis of cruise, final approach, and EDL has been performed by the MSL project for various combinations of launch date, arrival date, and landing site. The baseline approach trajectory used for this analysis is based on one of these cases studied by the MSL project and is given in Table 2.1. The atmospheric entry state for the selected MSL trajectory, which is listed in Table 2.2, corresponds to

Table 2.2: MSL entry state* in Mars-centered inertial coordinates

Component	Value (km)	Component	Value (km/s)
X	2509.459003	$\dot{X}$	-1.473129134
Y	377.697451	$\dot{Y}$	5.335713468
Z	-2442.509568	$\dot{Z}$	1.264687130

* Entry defined at an altitude of 125 km above the surface of Mars

the final condition of this valid Earth-Mars transfer trajectory that was used for approach navigation analysis [10]. When combined with an assumed entry body and EDL timeline, the entry state is also the initial condition for a trajectory that lands at the desired landing site, defined for this analysis as 41.45°S latitude and 286.74°E longitude. The details of this trajectory are not as important to this analysis as the fact that they represent a reasonable final approach and EDL trajectory for MSL.

The Mars Network will consist primarily of science orbiters, such as MRO, which entered its primary science orbit in 2006. The MRO orbit is a 255 km × 320 km near-polar orbit with periapsis frozen over the South Pole. The orbit is sun-synchronous with an ascending node orientation that provides a Local Mean Solar Time of 3:00 pm at the equator [30]. The nominal orbital elements of the MRO mission are summarized in Table 2.1. The MRO orbit is a typical science orbit that is chosen so as to ensure optimal conditions for its science instruments. As Table 2.1 shows, the MRO orbit is nearly identical

to the Mars Global Surveyor (MGS) and the Mars Odyssey (MOD) orbits, all of which can be characterized as low altitude, near-circular, near-polar orbits. Future science orbiters are likely to utilize similar orbits and consequently, MRO is a reasonable representative of the future orbiters that will make up the Mars Network.

The European Mars Express (MEX) mission offers a stark contrast to the typical science missions mentioned above. Although MEX will not participate directly in the Mars Network, future science orbiters that will participate in the Mars Network may utilize a similar orbit to MEX. As Table 2.1 shows, this orbit can be characterized as a medium altitude, high eccentricity orbit. The resulting relative dynamics between the MAV and the MNO during the final approach phase are significantly different compared to the dynamics associated with a typical science mission such as MRO and thus, the MEX mission offers a good model of comparison.

In addition to science orbiters such as MRO and MEX, the Mars Network may include a dedicated telecommunications orbiter, such as the Mars Telecommunications Orbiter (MTO), which was scheduled for launch in 2009 but canceled due to budgetary constraints. The MTO orbit, which is summarized in Table 2.1, was chosen so as to maximize coverage of approaching spacecraft during final approach and EDL. The orbit is significantly different from the nominal science orbits of MRO, MGS, and MOD, leading to significantly different relative approach dynamics. Interestingly, the MTO orbit is similar to the MEX orbit, the principal difference being that the MTO orbit

21
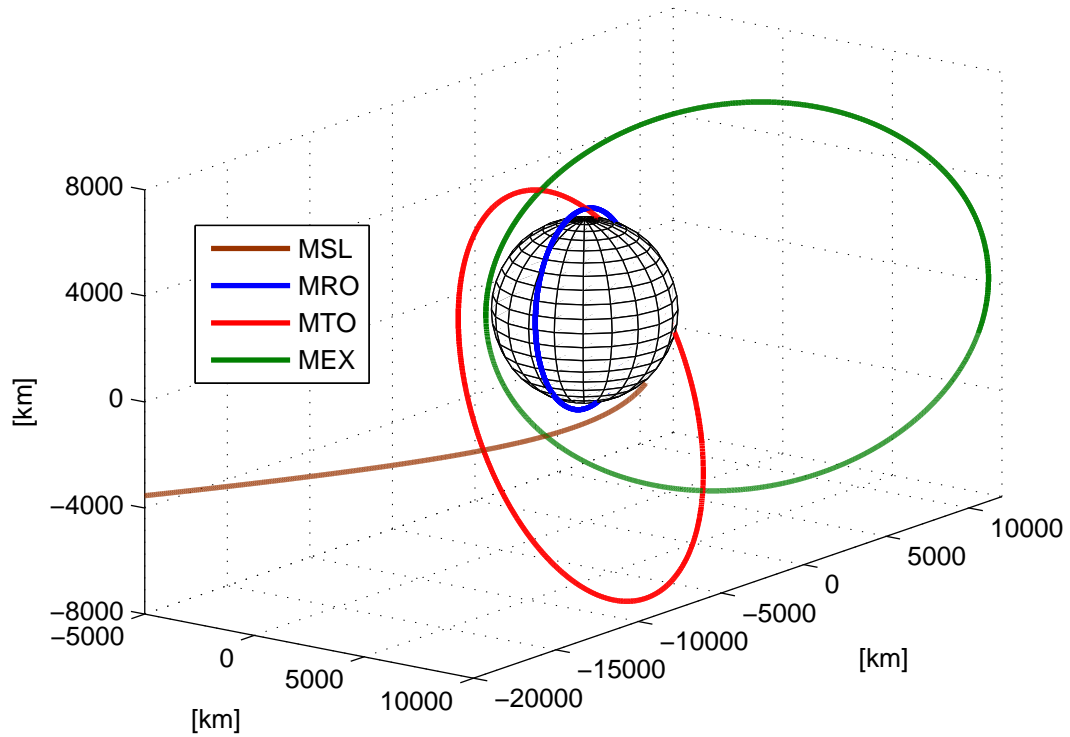
Figure 2.1: Nominal trajectories of MSL, MRO, MEX, and MTO

is retrograde while the MEX orbit is posigrade.

The nominal trajectories for MSL, MRO, MEX, and MTO just prior to atmospheric entry of MSL are shown in Figure 2.1. The figure clearly illustrates the differences in the various Mars Network orbits. In particular, the figure highlights the differences in the semi-major axis and eccentricity of the MRO, MEX, and MTO orbits. The result of these differences is that the orbital period of MRO is much shorter than the orbital period of both MEX

and MTO. Thus, when MRO is the Mars Network orbiter, it can be expected that the occultation of the Electra signal by Mars will be more frequent and the periods when line-of-sight visibility can be established will be shorter.

2.3 Dynamic Analysis

The performance of any navigation filter will depend on the performance of the carrier tracking loops and their ability to acquire and track the signal throughout the final approach and EDL phases. The regions of particular interest include (a) the maximum distance at which the link can be closed, (b) the region of greatest relative velocity, when the Doppler shift is a maximum, and (c) the region of greatest relative acceleration, when the change in Doppler shift is a maximum. In this study, a standard approach scenario between a MAV and a MNO is used to determine these regions and set bounds on the expected Doppler shifts and relative accelerations. Specifically, the standard approach trajectory for the 2010 encounter at Mars between MSL and MRO is used to determine the approach dynamics quantitatively. The hypothetical cases of an identical approach where MEX and MTO are acting as the Mars Network orbiter instead of MRO are also considered for purposes of comparison.

2.3.1 Spacecraft Model

The dynamic analysis is dependent on several assumptions regarding the attitudes of the MAV and MNO spacecraft, including the types of antennas

(a) Antenna pointing geometry   (b) Backshell location of UHF antennas
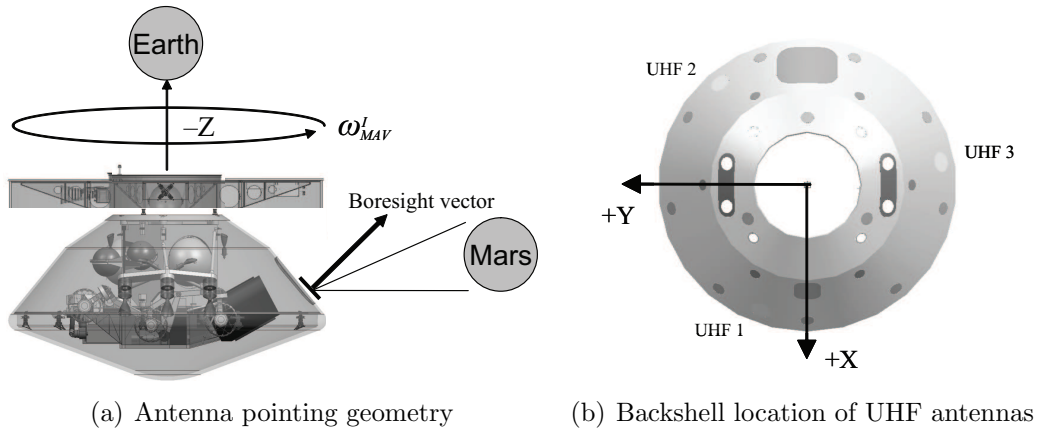
Figure 2.2: MAV antenna locations and pointing directions

used and their locations on the spacecraft. The MAV spacecraft is assumed to spin at a rate of 2 rpm about the +z axis of the spacecraft body-fixed frame. The attitude of the MAV spacecraft is constrained by the X-band link between the cruise, medium gain antenna (CMGA) and the DSN, which requires that the Earth lies within 5 deg of the −z axis as shown in Figure 2.2. The MAV spacecraft is assumed to have three UHF patch antennas, which are located on the lower cone of the backshell and separated by 120 deg. The lower cone of the backshell is inclined 50 deg to the −z axis of the body-frame. (Note that the current MSL design utilizes a single wrap-around antenna instead of the three patch antennas. The results of the analysis are still valid, however.)

It is assumed that the MNO spacecraft will have a dedicated antenna that can continuously track the approaching spacecraft. For a dedicated telecommunications orbiter such as MTO, this assumption is likely to be valid. However, for a science orbiter, the validity of this assumption is questionable.

If the MNO is a science orbiter, it will likely be nadir pointed and whether or not mission operations can or will allow it to maintain continuous tracking of an approaching spacecraft is uncertain. Current operations requirements for the MRO mission indicate that the spacecraft will not be able to track the MAV continuously. Instead MRO will track for upwards of 30 minutes in a given orbit before it will off-point for battery reasons. If continuous tracking is not feasible, then additional periods of signal outage are to be expected.

The inertial velocity and acceleration of the patch antennas on the MAV spacecraft are given by:

$$\dot{\boldsymbol{r}}^{I}_{MAV,antenna} = \dot{\boldsymbol{r}}^{I}_{MAV,cg} + \boldsymbol{\omega}^{I}_{MAV} \times \boldsymbol{r}^{B}_{MAV,antenna} \tag{2.3}$$

$$\ddot{\boldsymbol{r}}^{I}_{MAV,antenna} = \ddot{\boldsymbol{r}}^{I}_{MAV,cg} + \boldsymbol{\omega}^{I}_{MAV} \times \left(\boldsymbol{\omega}^{I}_{MAV} \times \boldsymbol{r}^{B}_{MAV,antenna}\right) \tag{2.4}$$

where

$$\boldsymbol{r}^{B}_{MAV,antenna} = \text{Location of the MAV antenna in the body frame}$$

$$\boldsymbol{\omega}^{I}_{MAV} = \text{Angular velocity of the MAV}$$

$$\dot{\boldsymbol{r}}^{I}_{MAV,cg} = \text{Inertial velocity of the MAV c.g.}$$

$$\ddot{\boldsymbol{r}}^{I}_{MAV,cg} = \text{Inertial acceleration of the MAV c.g.}$$

The range, range rate, and range acceleration between the MAV and the MNO are given by:

$$r = \left|\boldsymbol{r}^{I}_{MAV,cg} + \boldsymbol{r}^{B}_{MAV,antenna} - \boldsymbol{r}^{I}_{MNO,cg}\right| \tag{2.5}$$

$$\dot{r} = \left(\dot{\boldsymbol{r}}^{I}_{MAV,antenna} - \dot{\boldsymbol{r}}^{I}_{MNO,cg}\right)^{T} \hat{\boldsymbol{e}}^{I}_{r} \tag{2.6}$$

$$\ddot{r} = \left(\ddot{\boldsymbol{r}}^{I}_{MAV,antenna} - \ddot{\boldsymbol{r}}^{I}_{MNO,cg}\right)^{T} \hat{\boldsymbol{e}}^{I}_{r} \tag{2.7}$$

25

where

$$
\begin{aligned}
\boldsymbol{r}^I_{MAV,cg} &= \text{Inertial position of the MAV c.g.} \\
\boldsymbol{r}^I_{MNO,cg} &= \text{Inertial position of the MNO c.g.} \\
\dot{\boldsymbol{r}}^I_{MNO,cg} &= \text{Inertial velocity of the MNO c.g.} \\
\ddot{\boldsymbol{r}}^I_{MNO,cg} &= \text{Inertial acceleration of the MNO c.g.} \\
\hat{\boldsymbol{e}}^I_r &= \text{Unit vector from the MNO to the MAV}
\end{aligned}
$$

Note that the motion of the MNO antenna relative to the spacecraft center of mass is neglected in the dynamic analysis, because the MNO antenna is assumed to continuously track the MAV. Finally, the Doppler shift and the Doppler rate, which is the time rate of change of Doppler shift, are given by:

$$
\Delta f = f_R - f_T = -\frac{f_T \dot{r}}{c} \tag{2.8}
$$

$$
\dot{\Delta f} = -\frac{f_T \ddot{r}}{c} \tag{2.9}
$$

where f_R and f_T are the received and transmitted signal frequencies, respectively, and c is the speed of light.

2.3.2 Occultation Model

The communications link between the MAV and the MNO can only be established when line-of-sight visibility exists between the two spacecraft. A simple occultation model is used to determine the periods when line-of-sight exists [62]. The model is illustrated in Figure 2.3. The two half-angles θ_1 and θ_2 are given by:

$$
\theta_1 = \cos^{-1}\frac{R_{Mars}}{\mid \boldsymbol{r}_{MAV}\mid} \qquad \theta_2 = \cos^{-1}\frac{R_{Mars}}{\mid \boldsymbol{r}_{MNO}\mid} \tag{2.10}
$$
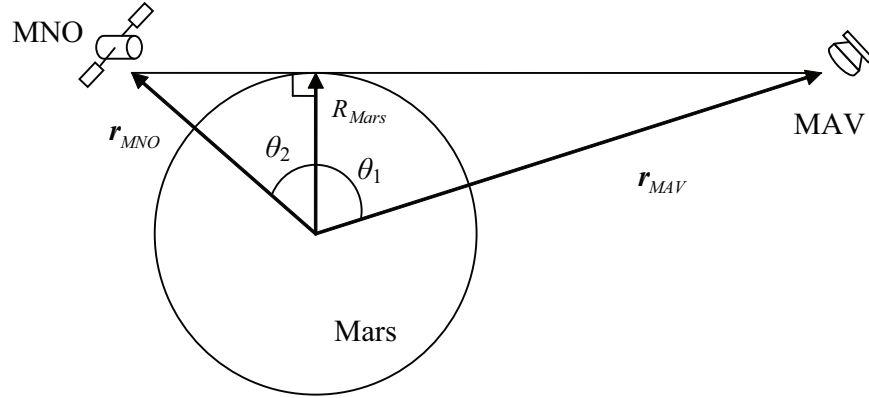
Figure 2.3: Occultation model for determining line-of-sight visibility

where R_{Mars} is the radial distance of Mars, and $\boldsymbol{r}_{MAV}$ and $\boldsymbol{r}_{MNO}$ are the position vectors of the MAV and the MNO spacecraft, respectively. The angle between the position vectors of the MAV and the MNO spacecraft is given by the scalar product:

$$\theta = \cos^{-1} \frac{\boldsymbol{r}_{MAV} \cdot \boldsymbol{r}_{MNO}}{|\,\boldsymbol{r}_{MAV}\,|\,|\,\boldsymbol{r}_{MNO}\,|} \tag{2.11}$$

Then in order for line-of-sight visibility to exist between the MAV and the MNO spacecraft, the following relationship must be satisfied:

$$\theta < \theta_1 + \theta_2 \tag{2.12}$$

2.3.3 Dynamic Results

The results of the dynamic analysis are shown in the following figures. Figure 2.4 verifies that the constraint imposed by the CMGA and DSN link

27

is satisfied throughout the final approach phase, where the angle from the $-z$ axis of the MAV body frame to the Earth is always less than 0.35 deg. The corresponding angle from the $-z$ axis to Mars is between 80–85 deg for the majority of the approach, though it increases rapidly to 120 deg towards the end of the approach phase.

More importantly, Figure 2.5 shows the angles between the antenna boresight vectors on the MAV and the MNO, during the first 60 seconds of the approach and during the last 60 seconds prior to atmospheric entry. The off-boresight angle, which is the angle between the antenna boresight vector and the direction of the incoming Electra signal, is determined by the attitude of the MAV spacecraft during approach and the locations of the UHF patch antennas on the backshell. As the figure shows, the off-boresight angle varies between 30–60 deg during the majority of the approach but increases to 50–70 deg during the last part of the approach. These angles determine not only which of the three patch antennas is actively tracking the Electra signal but also the gain of that signal. At a spin rate of 2 rpm, the antennas must be switched every 10 seconds, as shown in the figure.

The range, range rate, and range acceleration between the MAV and the MNO during the final approach phase are shown in Figure 2.6, while the Doppler shift and the Doppler rate are shown in Figure 2.7. Note that the effect of occultation of the line-of-sight vector between the MAV and the MNO due to the presence of Mars between the two spacecraft is included in the Doppler shift, resulting in periods of signal outage. The figures show the results for the
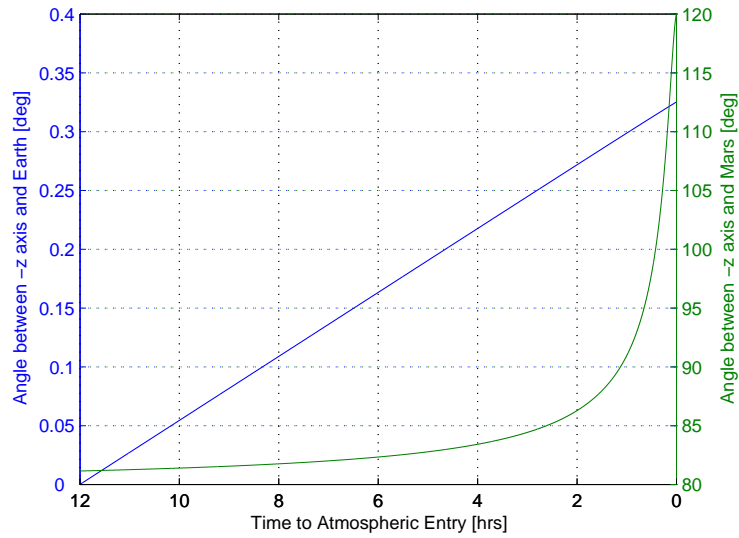
Figure 2.4: Angles between the MAV and the Earth and Mars
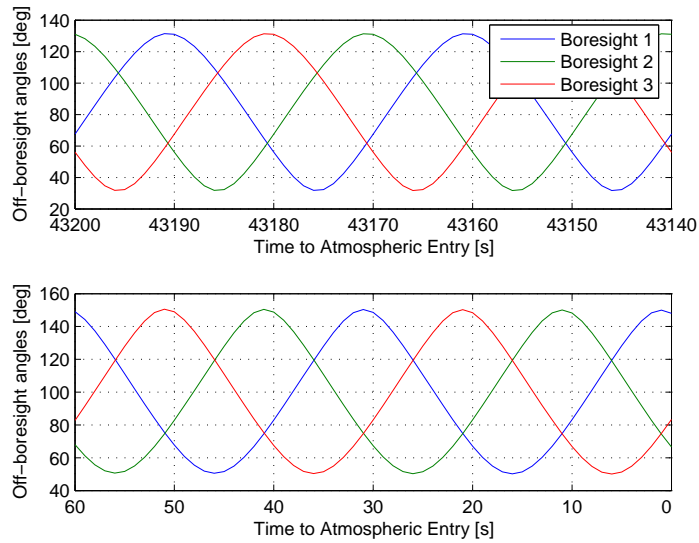
Figure 2.5: Antenna boresight vectors during the first 60 seconds (top) and the last 60 seconds (bottom) of the approach
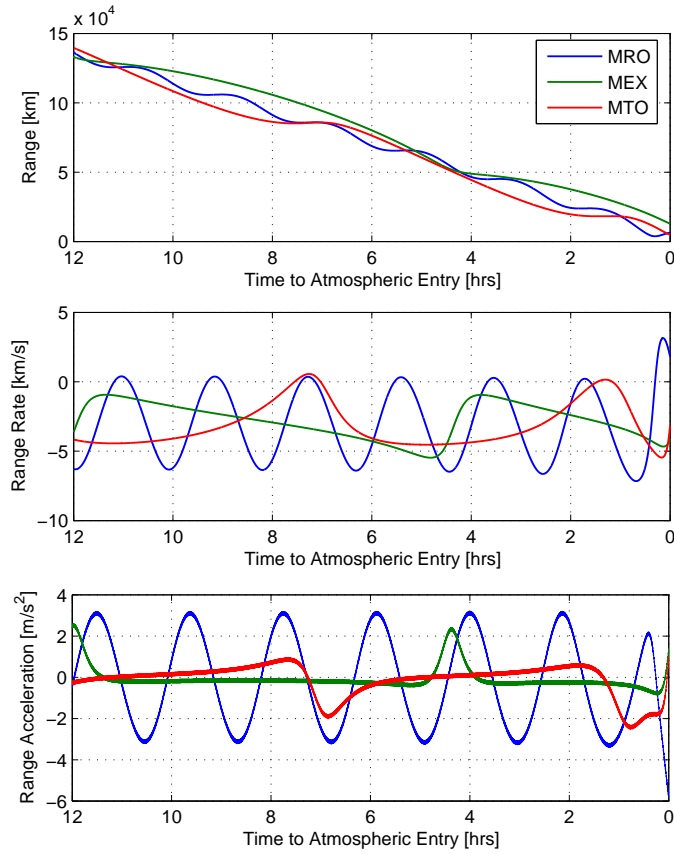
Figure 2.6: Range, range rate, and range acceleration during the final approach

three cases where the Mars Network orbiter is MRO, MEX, and MTO.

The results of the MRO case show that the Doppler shift peaks regularly at approximately 9.5 kHz throughout the majority of the approach, though just prior to atmospheric entry, the Doppler shift reaches its maximum value of 10.5 kHz. The oscillations in the Doppler shift are the result of the periodic orbit of MRO, which also causes the six periods of signal outage
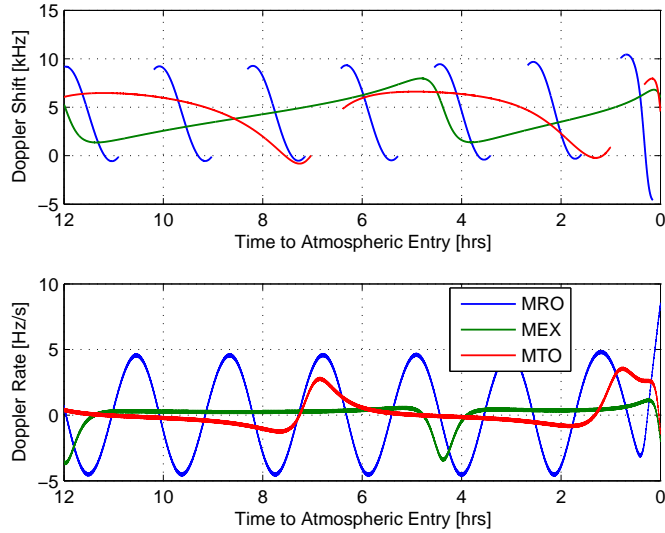
Figure 2.7: Doppler shift with occultation and Doppler rate during the final approach

that are the result of the occultation. The Doppler rate oscillates in a similar manner between approximately -4.5 Hz/s to $+4.5$ Hz/s throughout most of the final approach and increases to about $+8.5$ Hz/s just prior to atmospheric entry. This corresponds to a range acceleration between ± 3 m/s^2, with a peak acceleration of about -6 m/s^2.

The differences in the orbits of MRO, MEX, and MTO have a major influence on the relative approach dynamics. While MRO completes six orbits during the final approach phase, MEX and MTO complete only two orbits, with the result that there are far fewer oscillations in the Doppler shift and Doppler rate. The larger semi-major axis of the MEX and MTO orbits also means that the oscillations are much less severe. Although the peak Doppler

31

shift for both MEX and MTO is approximately 7.5 kHz, the Doppler shift is significantly less than this for the majority of the approach. More importantly, the range acceleration and hence, the Doppler rate, are much lower for both MEX and MTO than for MRO. This is clearly seen in Figure 2.6, where the range acceleration is nearly constant and less than ± 1 m/s^2 for the majority of the final approach for both MEX and MTO. This means that the requirements on the tracking loop to maintain signal lock will be less severe.

The maximum and minimum Doppler shift and range acceleration encountered during the final approach is a function of the differences in the geometries between the MAV and MNO orbits and the location of the MNO spacecraft in its orbit at certain critical times. Hence, the approach dynamics is a function of the three angles: the right ascension of the ascending node (RAAN), the argument of periapsis, and the true anomaly of the MNO. Note that it is not the absolute value of the RAAN that is the determining factor but rather the difference in RAAN between the MAV and MNO orbits.

For the case when the Mars Network orbiter is MRO, the maximum and minimum Doppler shift and range acceleration are primarily a function of the RAAN. This is due to the low eccentricity and hence, near-circular shape of the orbit, which means that the argument of periapsis has very little effect on the orbit characteristics. In addition, the low altitude and hence, short orbital period means that the true anomaly of MRO at the start of the final approach also has very little effect on the relative approach dynamics. The Doppler shift and range acceleration as a function of the difference in
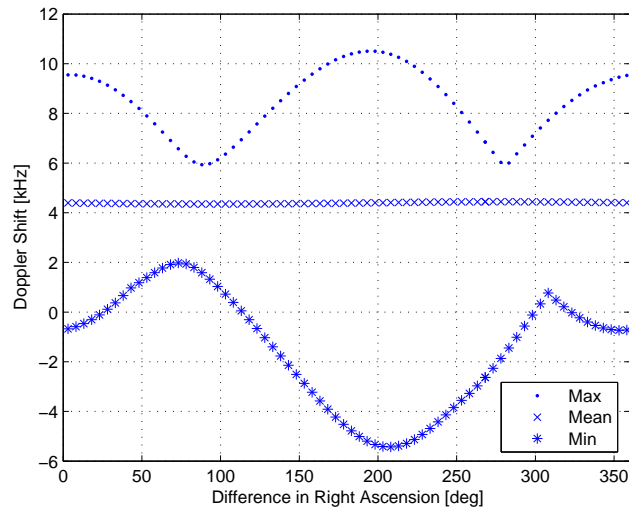
Figure 2.8: Maximum and minimum Doppler shift as a function of right ascension for MRO
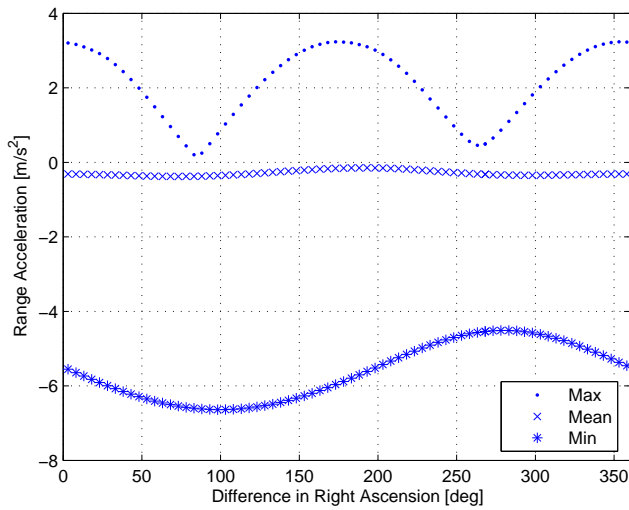
Figure 2.9: Maximum and minimum range acceleration as a function of right ascension for MRO

RAAN between the MAV and the MRO orbits are shown in Figures 2.8 and 2.9, respectively. Figure 2.8 shows that the maximum absolute value of the Doppler shift occurs when the difference in RAAN is close to 180 deg. This is what would be expected since, in this case, the velocity vectors of the MAV and the MRO spacecraft are as close to being colinear as possible. Similarly, Figure 2.9 shows that the maximum absolute value of the range acceleration occurs when the difference in RAAN is close to 90 deg. Again, this is what would be expected since the velocity vectors are now nearly perpendicular, meaning that the rate of change of the relative velocity is greatest.

The case is much more complicated when the Mars Network orbiter is either MEX or MTO. The large eccentricity of their orbits means that the argument of periapsis will have a significant effect on the relative approach dynamics. In addition, the large semi-major axis and hence, longer orbital period, means that the true anomaly of MEX and MTO at the start of the final approach phase will also have a significant effect on the relative approach dynamics. The complex interaction of the RAAN, the argument of periapsis, and the true anomaly on the relative approach dynamics means that it is difficult to make generalizations on the conditions which lead to maximum and minimum values of the Doppler shift and the range acceleration.

Figures 2.10–2.13 show the maximum and minimum Doppler shift and range acceleration when the Mars Network orbiter is MEX. The Doppler shift as a function of the difference in RAAN and true anomaly of MRO at the start of the final approach is shown in Figure 2.10. In this case, the argument of

34

periapsis is 0 deg. Similarly, the Doppler shift as a function of the difference in RAAN and argument of periapsis is shown in Figure 2.11, where the true anomaly of MRO at the start of the final approach is 0 deg. Equivalent plots that show the range acceleration as a function of RAAN, argument of periapsis, and true anomaly are shown in Figures 2.12 and 2.13. The figures show that the Doppler shift is bounded by $+10.8$ kHz and -9.8 kHz, while the range acceleration is bounded by $+3.3$ m/s^2 and -5.0 m/s^2.

Equivalent plots that show the maximum and minimum Doppler shift and range acceleration for MTO are given by Figures 2.14–2.17. The figures show that the Doppler shift is bounded by $+12.4$ kHz and -10.1 kHz, while the range acceleration is bounded by $+3.2$ m/s^2 and -5.8 m/s^2.

The peak values of Doppler shift and range acceleration, although important in determining the requirements on the tracking loop, are not as important as the distribution of the values of Doppler shift and range acceleration over time. The reason is that the peak values occur seldomly and then only briefly. Hence, it may be acceptable for the tracking loop to briefly lose signal lock during these periods of peak Doppler shift and range acceleration. The distributions of Doppler shift over time for all possible values of RAAN, argument of periapsis, and true anomaly for MRO, MEX, and MTO are shown in Figure 2.18. A similar plot for the distribution of range acceleration over time is shown in Figure 2.19. The results are summarized in Table 2.3, which shows the range of values of Doppler shift and range acceleration in which the MNO spends 75% and 95% of the final approach time.
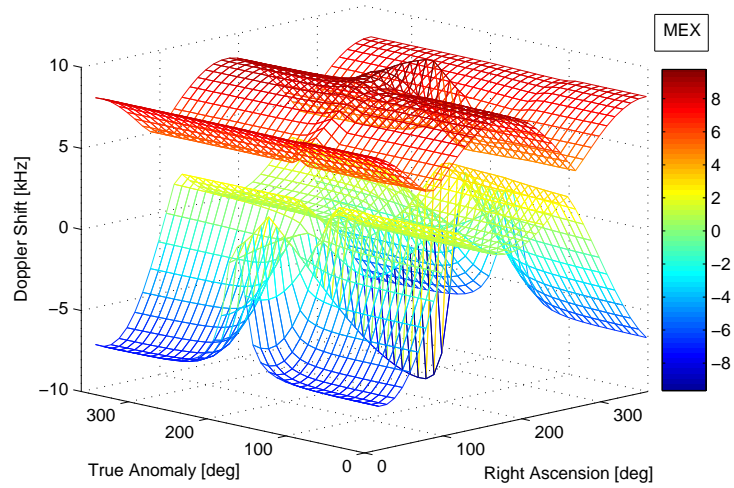
Figure 2.10: Maximum and minimum Doppler shift as a function of right ascension and true anomaly for MEX
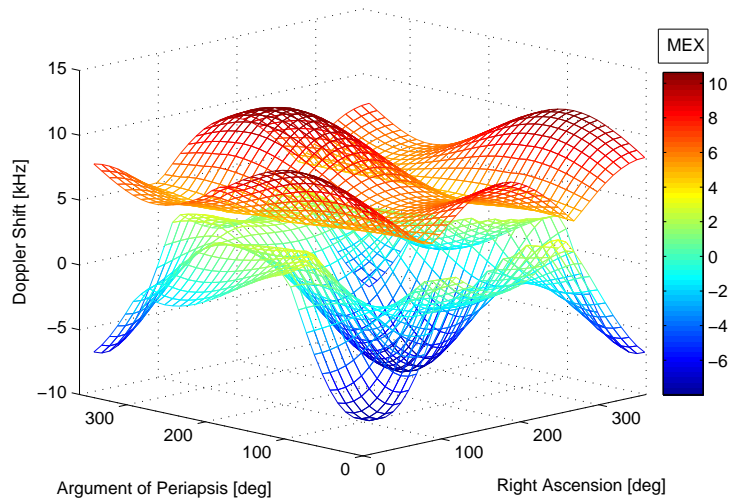
Figure 2.11: Maximum and minimum Doppler shift as a function of right ascension and argument of periapsis for MEX

36
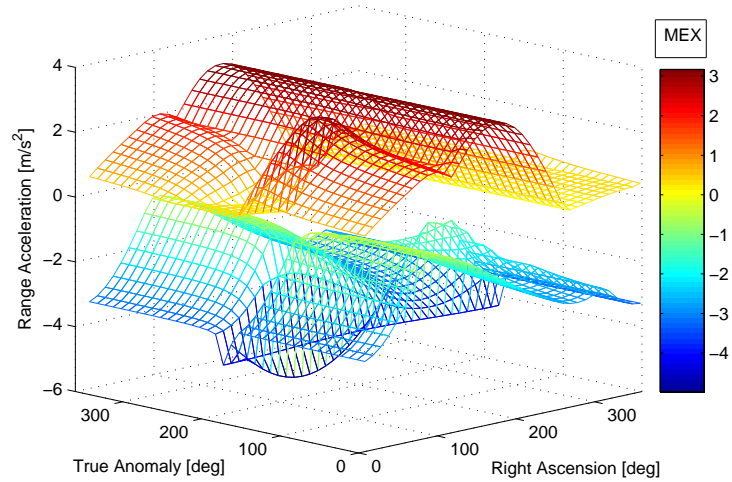
Figure 2.12: Maximum and minimum range acceleration as a function of right ascension and true anomaly for MEX
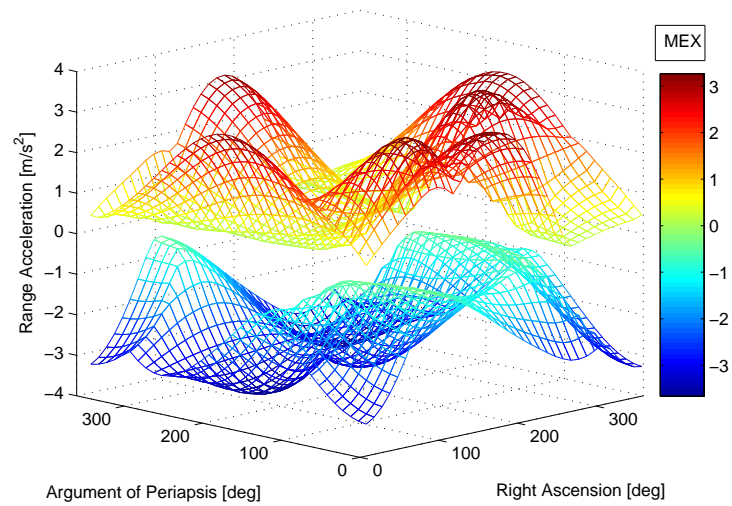
Figure 2.13: Maximum and minimum range acceleration as a function of right ascension and argument of periapsis for MEX
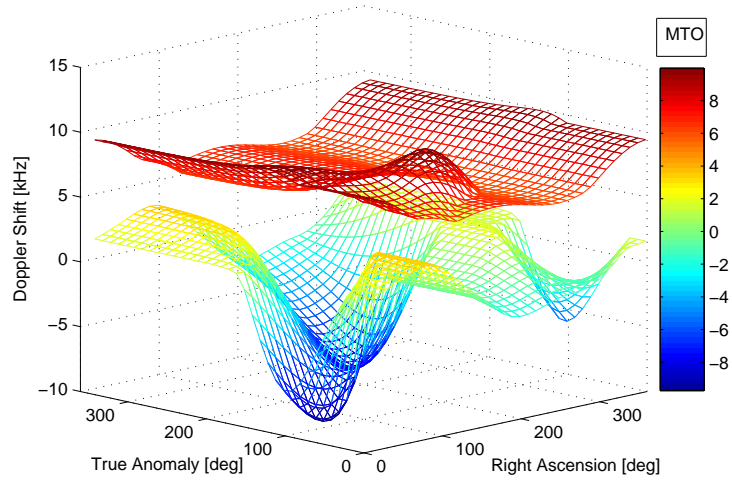
Figure 2.14: Maximum and minimum Doppler shift as a function of right ascension and true anomaly for MTO
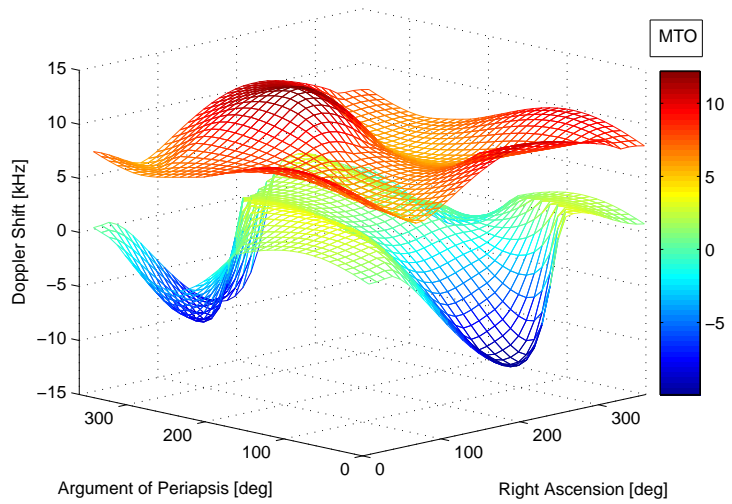
Figure 2.15: Maximum and minimum Doppler shift as a function of right ascension and argument of periapsis for MTO
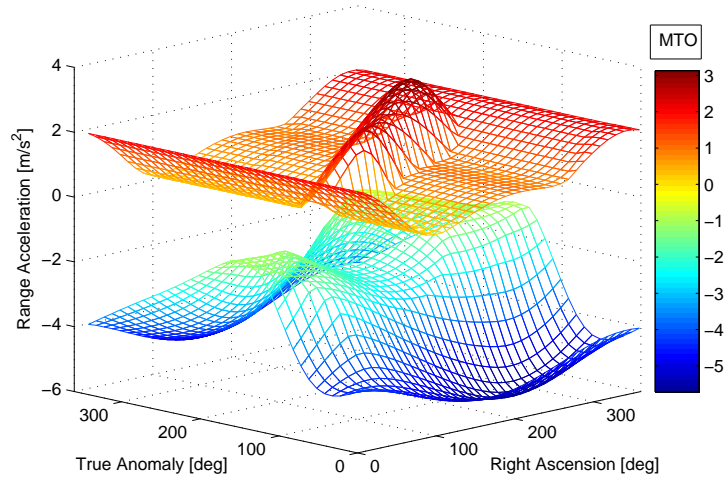
Figure 2.16: Maximum and minimum range acceleration as a function of right ascension and true anomaly for MTO
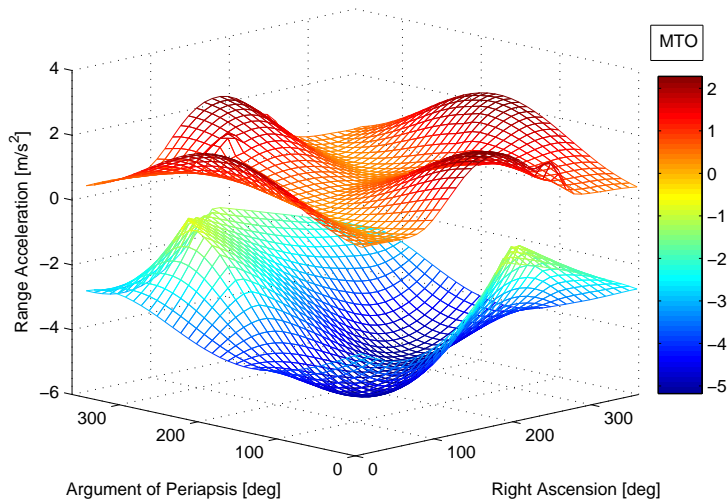
Figure 2.17: Maximum and minimum range acceleration as a function of right ascension and argument of periapsis for MTO
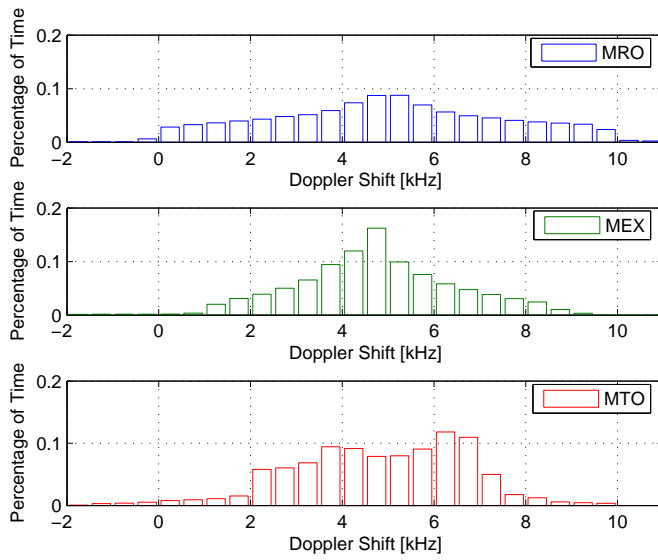
Figure 2.18: Distribution of the Doppler shift
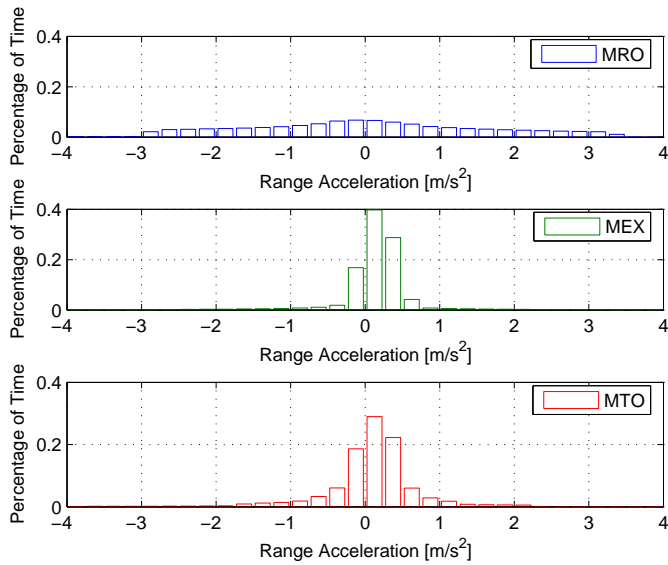
Figure 2.19: Distribution of the range acceleration

40

Table 2.3: Range of values of Doppler shift and range acceleration in which the MNO spends 75% and 95% of the time

	Time	MRO	MEX	MTO
Doppler shift	75%	$0.00 : 6.50$	$0.00 : 5.50$	$0.00 : 6.00$
(kHz)	95%	$0.00 : 9.00$	$0.00 : 7.50$	$0.00 : 7.00$
Range acceleration	75%	$-2.00 : +2.00$	$0.00 : 0.50$	$-0.25 : +0.50$
(m/s^2)	95%	$-2.75 : +3.00$	$-1.00 : +1.25$	$-1.50 : +1.25$

The data shows that the Doppler shift and range acceleration are distributed over a far wider range of values when the Mars Network orbiter is MRO than when it is MEX or MTO. This is particularly true for the range acceleration, where the range of values for MRO is twice the range for MEX and MTO. This is a consequence of the differences in their respective orbits, as previously discussed. Note that the range acceleration is directly related to the Doppler rate and is thus an important parameter for determining the tracking requirements of the tracking loop. Hence, when the Mars Network orbiter is MRO, the tracking loops must respond to a more dynamic operating environment.

Finally, the number of occultations and their average duration for the cases when the Mars Network orbiter is MRO, MEX, and MTO is illustrated in Figure 2.20. The figure shows that for MRO there are in general six occultations during the final approach, each lasting an average of 35–40 minutes. However, as would be expected, there are no occultations when the difference

41
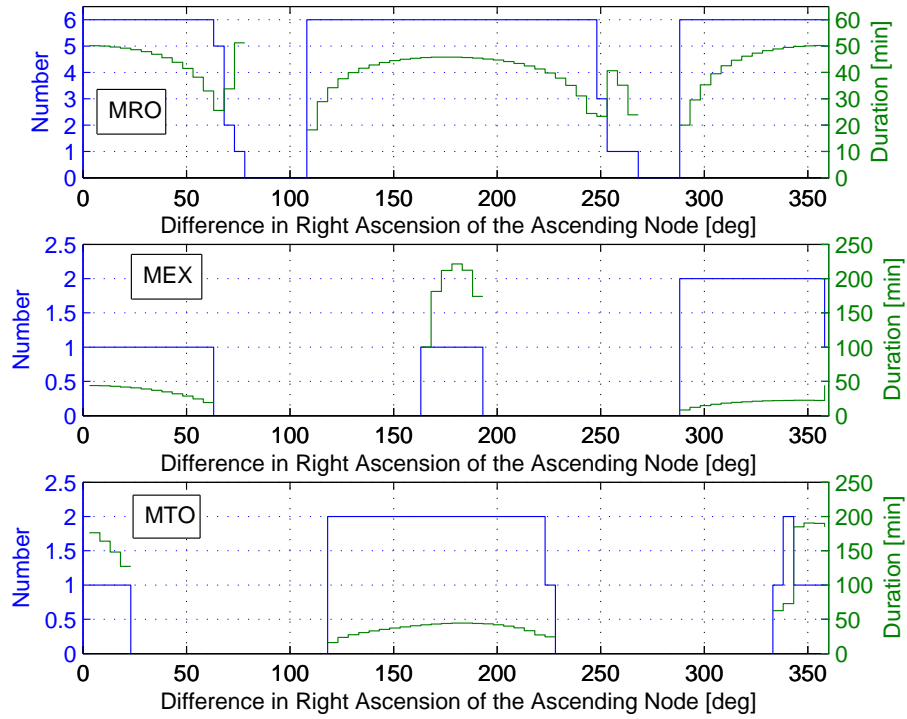
Figure 2.20: Number and duration of occultations

in RAAN between the MAV orbit and the MRO orbit lies in a narrow range of values close to either 90 deg or 270 deg. In this case, MRO is visible throughout the approach. In contrast, there are in general less than two occultations during the final approach when the Mars Network orbiter is either MEX or MTO. Furthermore, for a wide range of values of RAAN, there are no occultations at all. However, when a single occultation does occur, it may last up to 200 minutes.

The dynamic analysis has shown the effect that the orbit of the MNO

has on the relative approach dynamics and in particular, the effect it has on the Doppler shift, the Doppler rate, the range acceleration, the number of occultations, and their average duration. In general, the orbit of the MNO is determined by the type of orbiter. A typical science orbiter such as MRO will have a distinctly different orbit than a dedicated telecommunications orbiter such as MTO. This has a direct impact on the relative approach dynamics and consequently, on the dynamic operating environment of the transceiver tracking loops.

2.4   Link Budget Analysis

The complete two-way link budget used in the analysis begins with the output of the transceiver aboard the MAV and follows the link path to the transponder on the MNO, where the signal is retransmitted back to the MAV. A single transmit-receive leg of this link is analyzed in detail with the understanding that except for the transmit frequency (401 MHz v. 437 MHz) and the reversal of the antenna gains, the second half of the link is approximately the same.

2.4.1   Total Received Power

The transmitted power in decibel milliwatts (dBm) is given by [34]:

$$P = 30 + 10 \log P_{watts} \qquad (2.13)$$

where P_{watts} is the transmitted power in watts and 30 dBm is a product of the conversion from watts to milliwatts. The effective isotropic radiated power

43

(EIRP) of the transmitter is given by:

$$\text{EIRP} = P + G_t + L_t \tag{2.14}$$

where G_t is the transmitter antenna gain and L_t is the transmitter line losses. The power received by the receiver antenna is given by:

$$P_r = \text{EIRP} + L_s + L_p \tag{2.15}$$

where L_s is the space loss and L_p is the polarization loss. The space loss is calculated as:

$$L_s = \left(\frac{4\pi S}{\lambda}\right)^2 = \left(\frac{4\pi f S}{c}\right)^2$$

$$= -(20\log S + 20\log f + 32.45) \tag{2.16}$$

where S is the path length in km and f is the signal frequency in MHz. The term 32.45 dB results from

$$10\log\left(\frac{4\pi \times 10^9}{c}\right)^2$$

Note that the decision to include the frequency dependence as part of the space loss is a conventional accounting choice and that the minus sign preceding the right-hand side indicates that the term represents a loss. Finally, the total received power is given by:

$$P_{rt} = P_r + G_r + L_r \tag{2.17}$$

where G_r is the receiver antenna gain and L_r is the receiver line losses. Combining Equations 2.13–2.17 gives the following expression for the total received

power:

$$P_{rt} = 30 + 10 \log P_{watts} + G_t + L_t + L_s + L_p + G_r + L_r \qquad (2.18)$$

The total received power depends strongly on the receiver antenna gain G_r, which in turn, depends on the receiver antenna radiation patterns. It is assumed that the UHF patch antennas on the MAV are similar to the antennas used on the upcoming 2007 Phoenix Mars lander. These patch antennas are right-hand circularly polarized (RHCP) with a greater than 6 dB$_{ic}$ gain at the boresight. Note that the subscript ic indicates that the gain is referenced to a circularly polarized radiator. The polarization is elliptical, however, with a maximum axial ratio of -5 dB. Consequently, the alignment and rotation of the patch antennas with respect to the incoming signal can be such that the maximum effective boresight gain is 1 dB$_{ic}$. This is illustrated in Figure 2.21, which shows the assumed model of the antenna radiation patterns in (a) the horizontal plane and (b) the vertical plane. Note that only the main lobe is included in the model; the side lobes have been neglected. Since the actual alignment and rotation of the patch antennas are unknown, the worst case scenario is assumed in the analysis. Consequently, the maximum gain at boresight is assumed to be 1 dB$_{ic}$. Furthermore, the half-power beamwidth is assumed to be 80 deg and the gain at 90 deg is assumed to be -5 dB$_{ic}$. Finally, the voltage standing wave ratio at the frequencies of operation is 2:1. Note that the radiation patterns shown in Figure 2.21 are not based on actual measurements. Instead, they are models that have been derived from the design requirements, as stated above [32].

45

(a) Horizontal plane   (b) Vertical plane
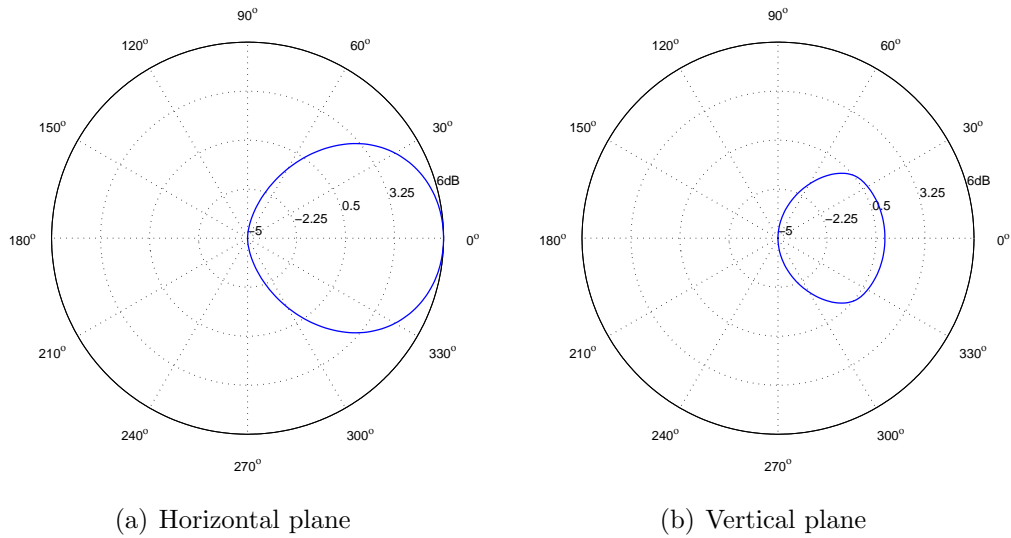
Figure 2.21: Antenna radiation patterns in two orthogonal planes. Only the main lobe is modeled.

The receiver antenna gain depends on the antenna off-boresight angles and is calculated using the radiation patterns shown in Figure 2.21. The off-boresight angles, which were calculated earlier and shown in Figure 2.5, vary between 30–60 deg during the majority of the approach but increase to 50–70 deg during the last part of the approach. Consequently, the Electra signal is received at approximately or slightly outside of the half-power beamwidth.

The total received power at each antenna is determined by the off-boresight angles. As the spacecraft rotates and the total received power at each antenna varies, a switching algorithm compares the power at each antenna and selects the antenna that is receiving the most power. The total received power during the final approach phase is shown in Figure 2.22 for MRO, MEX, and MTO. The parameter values that were assumed in the calculation of the total

46
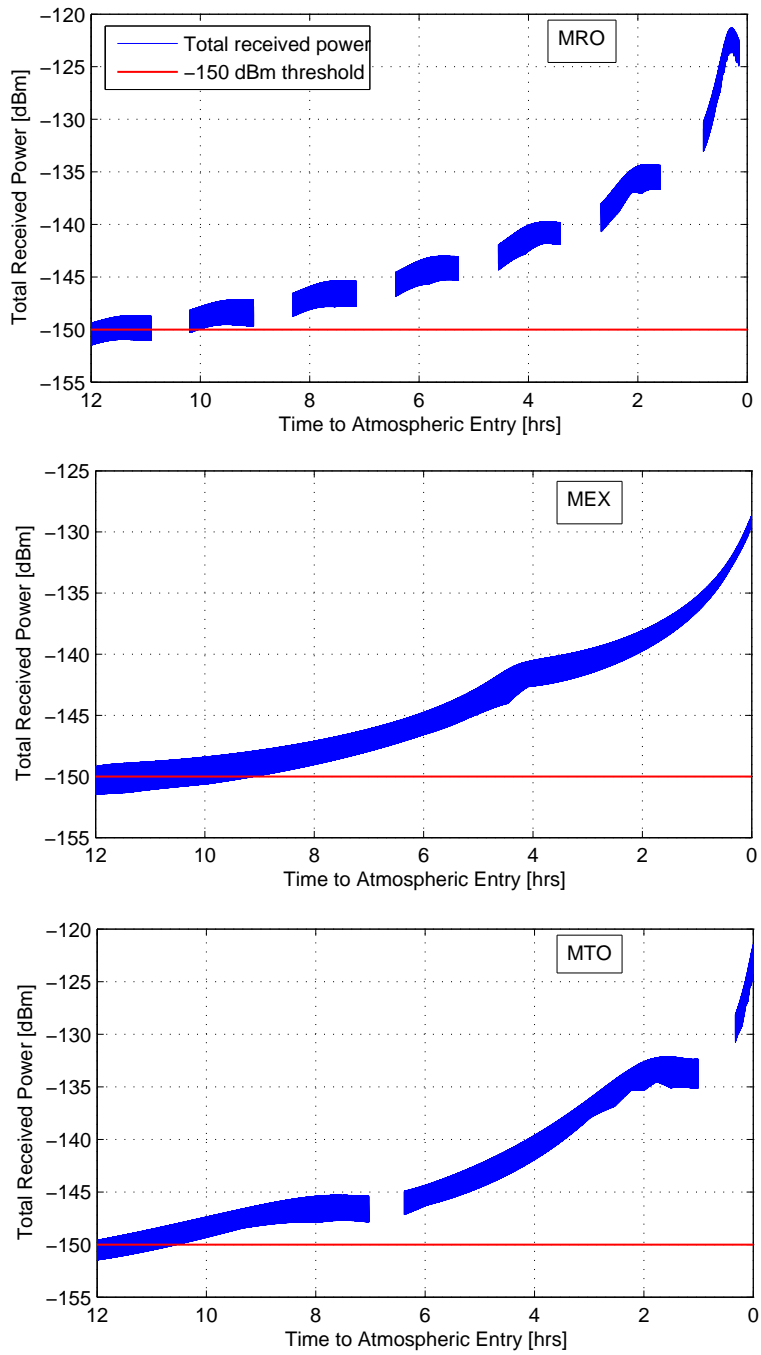
Figure 2.22: Total received power during the final approach for MRO (top), MEX (middle), and MTO (bottom)

Table 2.4: Link budget parameters used to calculate the total received power

Parameter	Value	Parameter	Value
Transmit power	8.5 W	Transmit frequency	437 MHz
Symbol rate	1 ksps	Transmitter antenna gain	3.5 dB
Polarization loss	−1 dB	Tracking loop bandwidth	1 kHz
Line losses	−2 dB	System noise temperature	526 K

received power are listed in Table 2.4. Note that the analysis includes the effect of occultation, which results in periodic signal outages, and the effect of the 2 rpm spin rate of the MAV, which results in a 2–3 dBm variation in the total received power as the patch antennas pass in and out of the Electra signal. The total received power required by the Electra to close the link has been determined by hardware tests in the laboratory, which have demonstrated that the Electra can reliably track signals as low as −150 dBm, as indicated by the red line in Figure 2.22. This indicates that link closure can be maintained continuously from about 10 hours prior to atmospheric entry for MRO and MTO and from about 9 hours prior to atmospheric entry for MEX. This corresponds to a range of about 110,000 km in each case, as indicated by Figure 2.6.

The effect of occultation is also shown in Figure 2.22. For MRO, there are five periods of signal outage and six tracking passes, each lasting approximately an hour, during which radiometric navigation data can be obtained.

In comparison, link closure can be maintained continuously throughout the final approach for MEX, while for MTO there are two periods of signal outage. (The number of occultations and their duration depend on the orbital parameters, as previously explained.)

2.4.2 Signal-to-Noise Ratio

The total received power-to-noise density ratio P_{rt}/N_0 is equal to the carrier power-to-noise density ratio C/N_0, as follows:

$$\frac{P_{rt}}{N_0} = \frac{C}{N_0} \tag{2.19}$$

The bit energy-to-noise density ratio is given by:

$$\frac{E_b}{N_0} = \frac{C}{N_0} - 10 \log B_R \tag{2.20}$$

where B_R is the bit rate in symbols per second. Thus, if the noise-density N_0 is known, the bit energy-to-noise density ratio E_b/N_0 can be calculated. The SNR of a phase modulated signal is then given by:

$$\text{SNR} = \frac{B_R}{B_W} \frac{E_b}{N_0} \tag{2.21}$$

where B_W is the filter bandwidth. For a BPSK modulation scheme, the quantity B_R/B_W is usually taken to be 1. Hence, the SNR is ideally equal to E_b/N_0. However, there is significant signal power loss through the complex baseband process in the Electra and fixed-point simulations have revealed that for data rates between 8 ksps and 1024 ksps, the SNR is given by [50]:

$$\text{SNR} = 0.62 \frac{E_b}{N_0} \tag{2.22}$$

49

The SNR for data rates between 1 ksps and 1024 ksps are shown in Figure 2.23 for MRO, MEX, and MTO. The SNR depends strongly on the data rate and varies between -40 dB and $+20$ dB throughout the final approach for each orbiter. The dependence of SNR on range is nearly identical for all three orbiters, as shown in the figure. Note that the Electra signal can also be transmitted in a carrier-only mode, without data modulation, in order to aid acquisition of the signal during the initial phase of the final approach. In this case, the bit energy-to-noise density ratio E_b/N_0 given in Equation 2.20 reduces to:

$$\frac{E_b}{N_0} = \frac{C}{N_0} \tag{2.23}$$

The result of the carrier-only mode is that the SNR is shifted up by 30 dB, as indicated by the 0 ksps curve in Figure 2.23. In this case, the SNR lies in the region from $+20$ dB to $+50$ dB.

2.5 Outcome of the Analysis

A high-fidelity model of the Electra signal can now be constructed using the calculated values of the Doppler shift, the Doppler rate, the total received power, and the SNR throughout the final approach. This signal forms the input to the carrier tracking loop of the Electra transceiver and will facilitate the analysis of the expected performance of the tracking loop and its ability to acquire and track the signal over the full range of expected operating conditions. In addition, it will facilitate the error characterization and error modeling of the Electra as a navigation sensor.
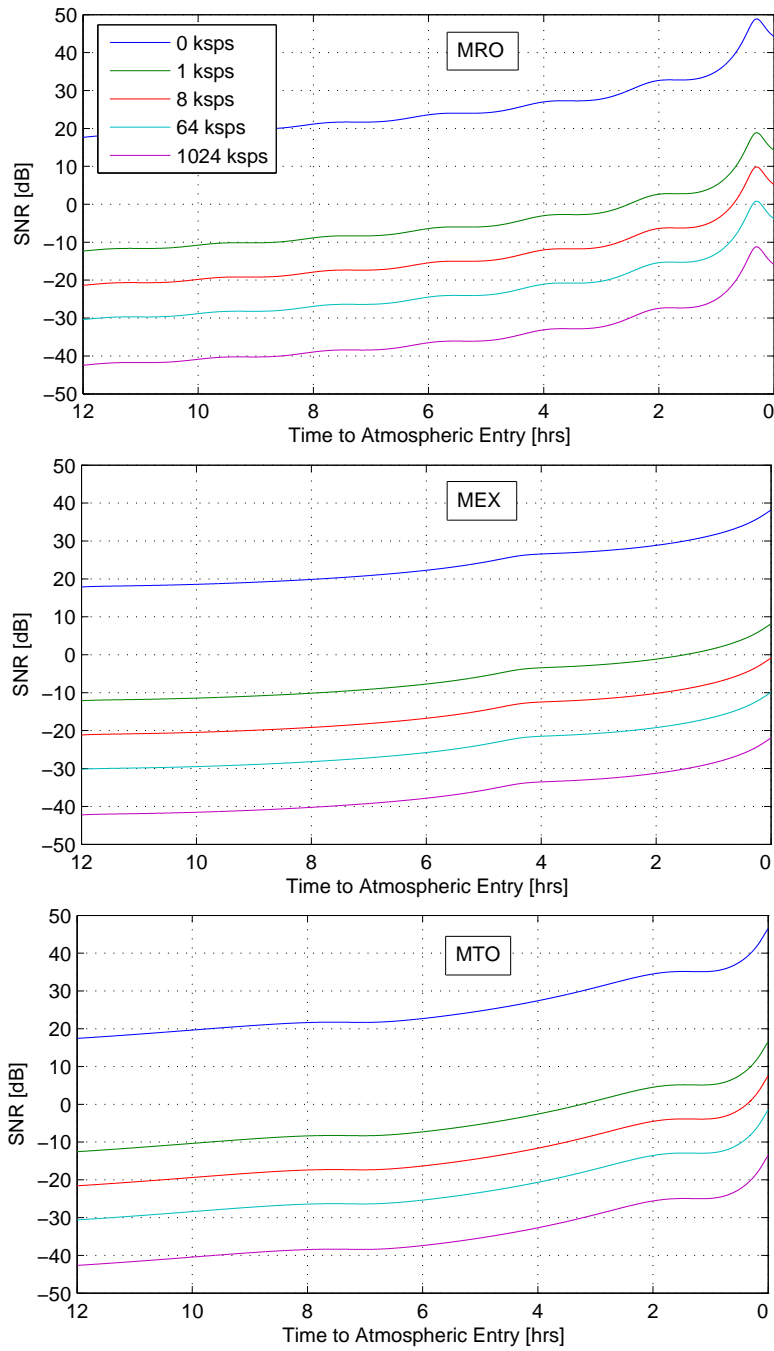
Figure 2.23: SNR during the final approach for MRO (top), MEX (middle), and MTO (bottom)

51

Chapter 3

The Electra UHF Transceiver

3.1 Introduction

A high-level block diagram of the Electra UHF transceiver that measures carrier phase is shown in Figure 3.1 [16]. The figure illustrates the frequency plan of the transceiver and shows the main components of the Electra, which include:

1. An ultra stable oscillator (USO) with frequency $f_{USO} = 76.56$ MHz, from which all other frequencies are derived.

2. An automatic gain control (AGC) circuit, which boosts the power of the received signal to a specified level.

3. A digital phase-locked loop (PLL) with frequency sweep for aided acquisition, which tracks the phase $\phi(t)$ of the received signal using a numerically controlled oscillator (NCO).

4. A front-end PLL, which functions as a mixer and translates the frequency of the received signal to an intermediate frequency $f_{IF} = 71.775$ MHz, which has been chosen so as to minimize noise during sampling.
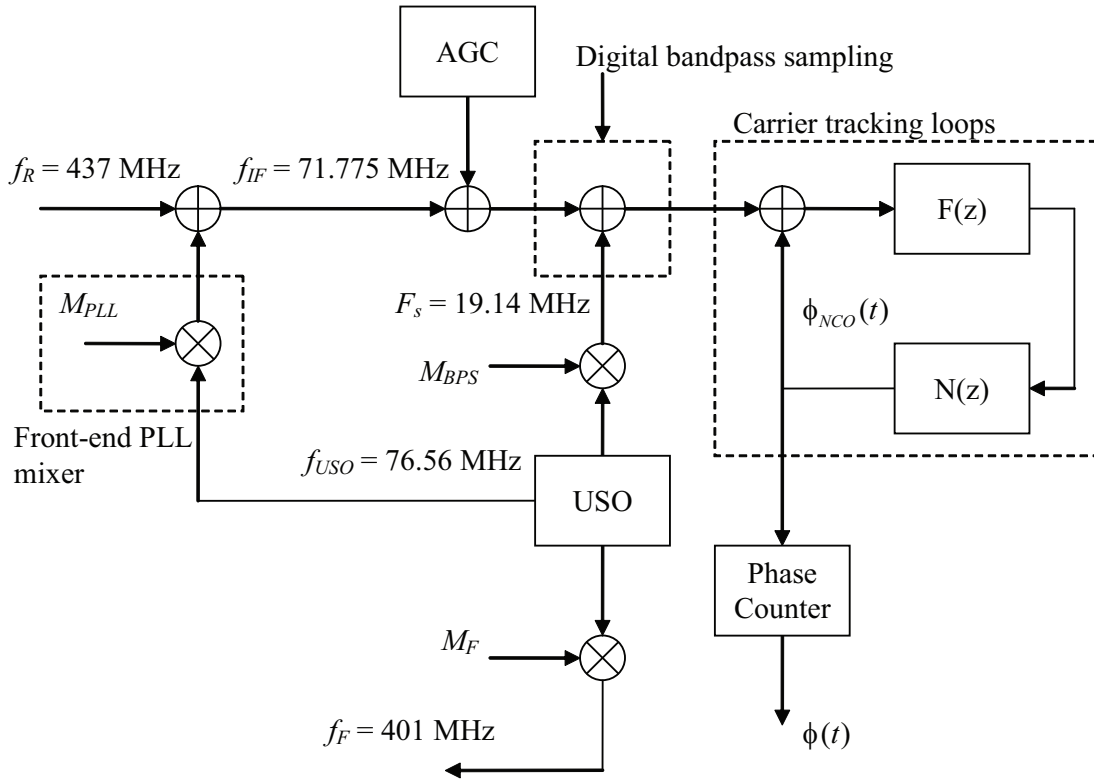
Figure 3.1: High-level block diagram of the Electra UHF Transceiver

5. A digital bandpass sampler, which provides analog-to-digital (A/D) sampling at $F_s = f_{USO}/4$, complex basebanding, and downsampling and decimation.

6. A phase accumulator, which reports the phase values $\phi(t)$ continuously.

The forward link from the transceiver to the transponder has a nominal frequency f_F of 401 MHz, while the return link from the transponder to the transceiver has a nominal frequency f_R of 437 MHz. The transpon-

der, which is identical to the transceiver, phase coherently remodulates the measured phase onto the return link signal and multiplies the remodulated signal by a turnaround ratio. The multiplicative constants M_f (or M_R for the transponder), M_{BPS}, and M_{PLL} shown in Figure 3.1 are frequency multipliers that are defined so as to produce the correct frequencies.

A software model of the baseband processing module (BPM) of the Electra transceiver has been developed in MATLAB by JPL. The model consists of the digital portion of the Electra transceiver, which contains the digital signal processing functions, including the AGC, the digital bandpass sampling, the NCO-based carrier tracking loop with frequency sweep and lock detection for aided acquisition, and the phase accumulator. The model provides a direct, bit-to-bit mapping of the functions implemented in the actual flight field programmable gate array (FPGA) and all variables in the software model are quantized to their true levels in the FPGA. The software model allows the performance of the tracking loop to be evaluated for a range of BPSK signals with different data rates, Doppler shifts, Doppler rates, signal strengths, and SNRs. In addition, the ability of the tracking loop to acquire and track the transmitted signal can be investigated for a range of tracking loop parameters such as tracking loop bandwidth and tracking loop order. Note that the Electra software model does not include a model of the USO. The Electra model also does not include a model of the front-end PLL that reduces the received signal frequency f_R to the intermediate frequency f_{IF}. Instead, the Electra software model operates directly on the intermediate frequency signal.

3.2 Signal and Noise Model

The Electra transceiver can transmit a carrier-only signal or a BPSK signal in one of two modes: BPSK with suppressed carrier or BPSK with residual carrier. The BPSK data is encoded using bipolar, nonreturn-to-zero (NRZ) data format for the suppressed carrier signal, while the data is encoded using biphase Manchester data format for the residual carrier signal. Manchester data format is chosen for the residual carrier signal because there is a spectral null in the middle of the Manchester power spectrum, which enhances residual carrier tracking by removing the interference from the data component of the signal [47]. A detailed description of the Electra modulation architecture, including the structure of the transmitted BPSK signals and the data encoding formats is given in Appendix A. To summarize, the transmitted BPSK signal can be represented by:

$$x(t) = \begin{cases} A'd(t)\cos\left[2\pi f_c t + \theta_{in}(t)\right] & \text{for suppressed carrier} \\ A'\cos\left[2\pi f_c t + \delta d(t) + \theta_{in}(t)\right] & \text{for residual carrier} \end{cases} \tag{3.1}$$

where

$$
\begin{aligned}
f_c &= \text{Nominal carrier frequency} \\
A' &= \text{Signal amplitude} \\
\delta &= \text{Modulation index} \\
d(t) &= \text{Binary valued } (\pm 1) \text{ data corresponding to either NRZ or} \\
&\quad \text{Manchester encoded data} \\
\theta_{in}(t) &= \text{Input phase offset}
\end{aligned}
$$

The modulation index for the suppressed carrier signal is $\delta = \pi/2$ rad, which leads to the simplified expression given first in Equation 3.1. Conversely, the modulation index is set to $\delta = \pi/3$ rad for the residual carrier signal.

After transmission and free-space propagation between the two spacecraft, the BPSK signal that is received by the front-end of the Electra transceiver can be modeled as:

$$x(t) = \begin{cases} A'd(t)\cos\left[2\pi(f_c + df)t + \theta_{in}(t)\right] + N(t) \\ \qquad\qquad\qquad \text{for suppressed carrier} \\ A'\cos\left[2\pi(f_c + df)t + \delta d(t) + \theta_{in}(t)\right] + N(t) \\ \qquad\qquad\qquad \text{for residual carrier} \end{cases} \qquad (3.2)$$

where df is the Doppler shift, resulting from the relative approach dynamics, and $N(t)$ is additive noise, such as thermal noise, shot noise, and any other physical noise sources.

The received BPSK signal is first frequency translated to the intermediate frequency $f_{IF} = 71.775$ MHz by the front-end PLL before being sent to the Electra BPM, where all the digital signal processing functions occur. Note that the front-end PLL is not included in the software model.

3.3   Digital Bandpass Sampling

The digital bandpass sampling consists of A/D conversion, complex basebanding, and downsampling and decimation as illustrated in Figure 3.2 [51]. The input to the A/D converter is the intermediate frequency signal that
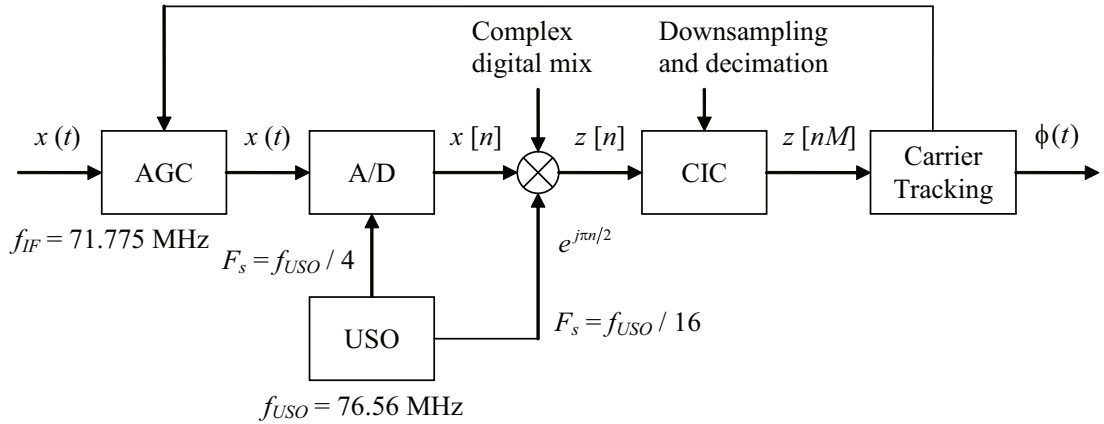
Figure 3.2: Digital bandpass sampling

has been amplified to a specified level by the AGC. Note that the intermediate frequency has been selected so as to minimize noise during the sampling process. The input signal to the A/D converter can be represented by:

$$
x(t) = \begin{cases} A\,d(t)\cos\left[2\pi(f_{IF}+df)t + \theta_{in}(t) + \theta_{AGC}(t)\right] + N(t) \\ \qquad\qquad\qquad\qquad \text{for suppressed carrier} \\[2ex] A\cos\left[2\pi(f_{IF}+df)t + \delta d(t) + \theta_{in}(t) + \theta_{AGC}(t)\right] + N(t) \\ \qquad\qquad\qquad\qquad \text{for residual carrier} \end{cases} \tag{3.3}
$$

where $A = A' \times A_{AGC}$ and A_{AGC} and $\theta_{AGC}(t)$ are the amplitude and the phase contribution from the AGC, respectively.

3.3.1 Analog-to-Digital Conversion

The intermediate frequency signal given by Equation 3.3 represents a continuous-time bandpass signal that is centered about the frequency f_{IF} and

that has a certain bandwidth f_B as determined by the modulation scheme and the Doppler shift. If the Fourier transform of the binary data signal $d(t)$ is given by:

$$D(f) = \int_{-\infty}^{\infty} d(t)\, e^{-j2\pi ft}\, dt \tag{3.4}$$

then the modulation theorem can be used to represent the continuous-time Fourier transform of the intermediate frequency signal by:

$$X(f) = \begin{cases} \frac{1}{2}Ae^{j\theta(t)}D(f - f_{IF}) + \frac{1}{2}Ae^{-j\theta(t)}D(f + f_{IF}) \\ \qquad\qquad\qquad\qquad \text{for suppressed carrier} \\ \\ \frac{1}{2}Ae^{j\theta(t)}\big[D(f - f_{IF}) + \delta(f - f_{IF})\big] + \frac{1}{2}Ae^{-j\theta(t)} \\ \big[D(f + f_{IF}) + \delta(f + f_{IF})\big] \qquad \text{for residual carrier} \end{cases} \tag{3.5}$$

where $\delta(f)$ is the unit impulse function or Dirac delta function and where

$$\theta(t) = 2\pi\, df\, t + \theta_{in}(t) + \theta_{AGC}(t) \tag{3.6}$$

Note that the unit impulse function in Equation 3.5 is a direct consequence of the residual carrier term, which is explicitly derived in Equation A.7 in Appendix A. A conceptual representation of the Fourier transforms given by Equation 3.5 is shown in Figure 3.3, which shows the continuous-time Fourier transform of (a) the suppressed carrier signal and (b) the residual carrier signal. Both signals are centered at the intermediate frequency f_{IF} and have a given bandwidth f_B. The difference between the two signals is the residual carrier term, which is represented by the unit impulse function centered at f_{IF}.

In traditional sampling, the Nyquist criterion requires that the sampling

58

rate F_s satisfies the relationship:

$$F_s \geq 2(f_{IF} + f_B/2) \tag{3.7}$$

in order to avoid aliasing. The Electra A/D conversion, however, employs a bandpass sampling technique, which maps the intermediate frequency band directly down to digital baseband. By taking advantage of the spectral signal replications that are inherent to the sampling process, bandpass sampling reduces the sampling rate below the Nyquist rate and reduces the amount of digital memory necessary to capture a given time interval of a continuous-time signal. Referring to Figure 3.3 (c) and (d), which shows the continuous-time Fourier transforms of the sampled suppressed carrier signal and the sampled residual carrier signal, respectively, the signal replications occur at frequencies f_i that are given by:

$$f_i = \pm f_{IF} \pm i\,F_s \qquad \text{for } i = 0, 1, 2, \ldots \tag{3.8}$$

The bandpass sampling maps the intermediate frequency signal directly down to digital baseband, as long as the frequency band

$$f_{IF} - \frac{F_s}{4} \leq f \leq f_{IF} + \frac{F_s}{4} \tag{3.9}$$

coincides with one of the image bands

$$k\frac{F_s}{2} \leq f \leq (k+1)\frac{F_s}{2} \tag{3.10}$$

for some integer k [64]. This leads to the following condition on f_{IF} and F_s:

$$f_{IF} = (2k+1)\frac{F_s}{4} \tag{3.11}$$

59

This guarantees that the intermediate frequency f_{IF} will be mapped down to the center of the Nyquist band $F_s/4$. Furthermore, the sampling rate F_s should just exceed twice the intermediate frequency filter bandwidth $2B_{IF}$ in order to maintain the lowest possible A/D sampling rate and avoid aliasing [64]. Thus the sampling frequency is chosen as:

$$F_s = \frac{f_{USO}}{4} = 19.14\,\text{MHz}. \tag{3.12}$$

which is far below the Nyquist rate of $2(f_{IF} + f_B/2)$.

The output of the A/D converter is the sampled, discrete-time signal, which can be represented as $x[n] = x(nT_s)$ as follows:

$$x[n] = \begin{cases} A\,d(nT_s)\cos\big[-\pi n/2 + \theta(nT_s)\big] + N(nT_s) \\ \qquad\qquad\qquad\qquad \text{for suppressed carrier} \\[2mm] A\cos\big[-\pi n/2 + \delta d(nT_s) + \theta(nT_s)\big] + N(nT_s) \\ \qquad\qquad\qquad\qquad \text{for residual carrier} \end{cases} \tag{3.13}$$

where $T_s = 1/F_s$ is the sample period, n is the index of the discrete-time sequence, and

$$\theta(nT_s) = 2\pi n\,\frac{df}{F_s} + \theta_{in}(nT_s) + \theta_{AGC}(nT_s) \tag{3.14}$$

Note that as a consequence of the bandpass sampling, an integer number of multiples of 2π has been removed from the argument of the cosine function to yield the expression given by Equation 3.13.
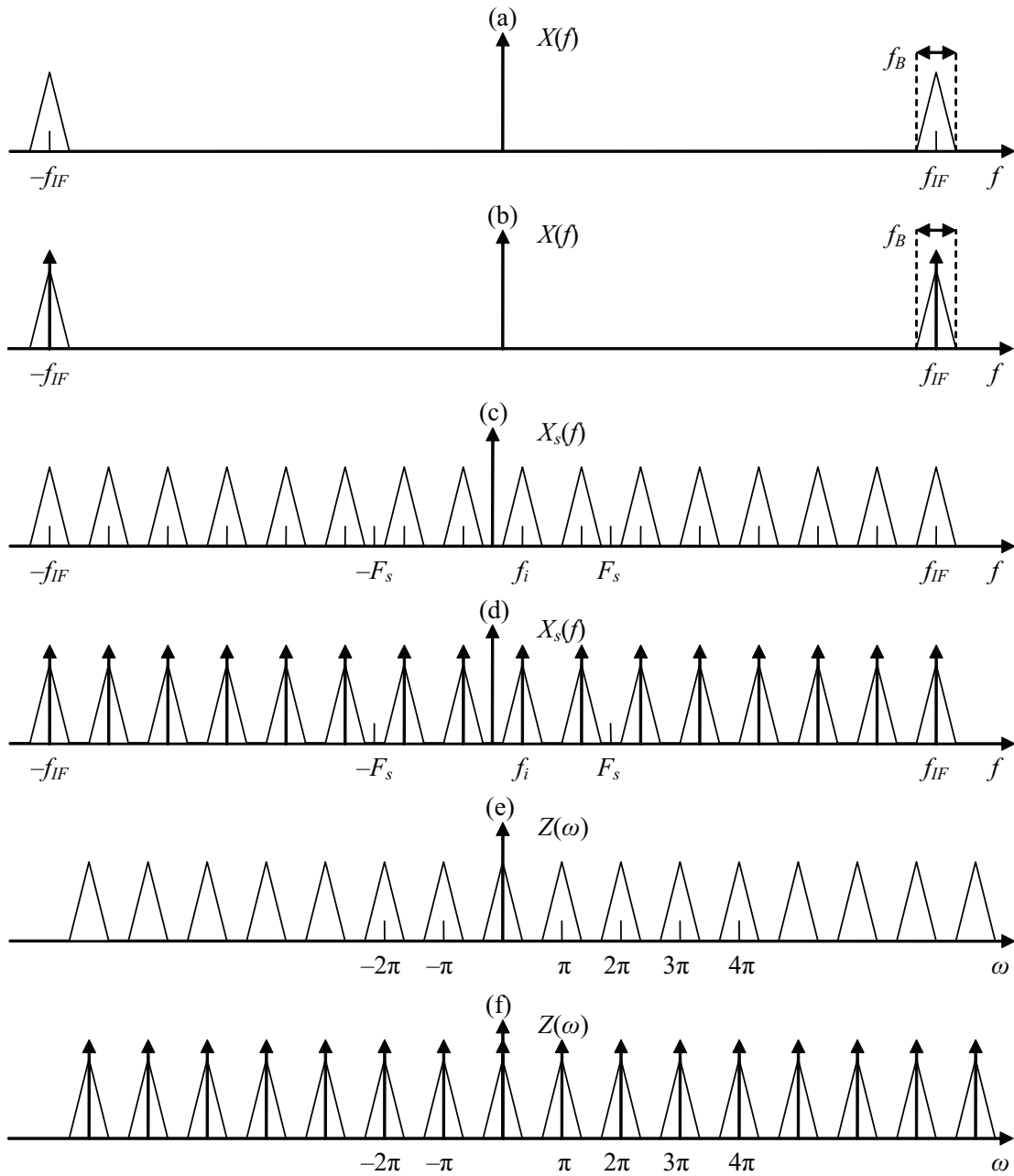
Figure 3.3: Fourier transforms of (a) the suppressed carrier signal, (b) the residual carrier signal, (c) the sampled suppressed carrier signal, (d) the sampled residual carrier signal, (e) the complex baseband suppressed carrier signal, and (f) the complex baseband residual carrier signal

61

3.3.2 Complex Basebanding

After A/D conversion, the sampled, discrete-time signal is digitally downconverted and decimated using a digital complex baseband downconversion scheme. The first step involves digital complex mixing to produce the complex signal, given by:

$$z[n] = x[n]e^{j\pi n/2} \tag{3.15}$$

where the discrete-time frequency $\pi n/2$ rad/sample of the complex exponential is equal to the frequency of the sampled signal $x[n]$ in Equation 3.13. The operation given by Equation 3.15 corresponds to frequency translation in the frequency domain. Thus the discrete-time Fourier transform of $z[n]$ can be represented conceptually as shown in Figure 3.3 (e) and (f). Note that the horizontal frequency axis has been normalized according to:

$$\omega = 2\pi f T_s \tag{3.16}$$

which corresponds to the transformation from continuous-time to discrete-time. Combining Equations 3.13 and 3.15, the result of the complex mixing is:

$$z[n] = \begin{cases} \frac{1}{2}A\,d(nT_s)\left\{e^{j\theta(nT_s)} + e^{j[\pi n - \theta(nT_s)]}\right\} + N_b(nT_s) \\ \qquad\qquad\qquad\qquad \text{for suppressed carrier} \\ \\ \frac{1}{2}A\left\{e^{j[\delta d(nT_s)+\theta(nT_s)]} + e^{j[\pi n - \delta d(nT_s)+\theta(nT_s)]}\right\} + N_b(nT_s) \\ \qquad\qquad\qquad\qquad \text{for residual carrier} \end{cases} \tag{3.17}$$

where the received noise has now been translated to complex baseband and can be represented by:

$$N_b(t) = N_I(t) + jN_Q(t) \tag{3.18}$$

where $N_I(t)$ and $N_Q(t)$ are approximately statistically independent, stationary, white Gaussian noise processes.

The first exponential term $e^{j\theta(nT_s)}$ or $e^{j[\delta d(nT_s)+\theta(nT_s)]}$ in Equation 3.17 corresponds to the slowly varying phase of the received signal, which contains the navigation information. This is the term that the carrier tracking loop aims to track. The second exponential term corresponds to the second harmonic of the carrier signal, where the input signal frequency has been doubled to $2f_{IF}$ Hz in the continuous-time domain or πn rad/sample in the discrete-time domain. The second harmonic of the carrier frequency can be removed by lowpass filtering the signal, leaving only the slowly varying phase term:

$$z[n] = \begin{cases} \frac{1}{2}A\,d(nT_s)e^{j\theta(nT_s)} + N_b(nT_s) & \text{for suppressed carrier} \\ \frac{1}{2}Ae^{j[\delta d(nT_s)+\theta(nT_s)]} + N_b(nT_s) & \text{for residual carrier} \end{cases} \tag{3.19}$$

3.3.3 Downsampling and Decimation

The second step in the digital complex baseband downconversion scheme involves digital decimation, if necessary, via a first-order cascaded-integrator-comb (CIC) filter. Electra requires at least 16 samples per symbol to accommodate symbol timing recovery, except at the highest data rates [64]. Consequently, at the lower data rates, the discrete-time signal can be downsampled

by a factor M, giving a new effective sampling frequency:

$$f_s = \frac{F_s}{M} \tag{3.20}$$

The downsampling factor M depends on the data rate and is increased proportionally such that:

$$\frac{F_s}{R_s M} = 16 \tag{3.21}$$

where R_s is the bit rate. At the highest data rates, M is nominally set to 1 so that there is no downsampling and decimation. Below a bit rate of 8 kbps, M remains fixed at 128 in order to accommodate Doppler offsets. The downsampling and decimation is accomplished via a first-order CIC filter, as shown in Figure 3.4. CIC filters are flexible, multiplierless, and can handle arbitrary and large rate changes [28]. The output of the CIC filter is the downsampled baseband signal given by:

$$z[nM] = \begin{cases} \frac{1}{2} A\, d(nMT_s) \left\{ e^{j\theta(nMT_s)} + e^{j[\pi n - \theta(nMT_s)]} \right\} \\ + N_b(nMT_s) \qquad\qquad \text{for suppressed carrier} \\ \frac{1}{2} A \left\{ e^{j[\delta d(nMT_s) + \theta(nMT_s)]} + e^{j[\pi n - \delta d(nMT_s) + \theta(nMT_s)]} \right\} \\ + N_b(nMT_s) \qquad\qquad \text{for residual carrier} \end{cases} \tag{3.22}$$

where $\theta(nMT_s)$ is now given by:

$$\theta(nMT_s) = 2\pi n\, \frac{df}{F_s} + \theta_{in}(nMT_s) + \theta_{AGC}(nMT_s) \tag{3.23}$$

Note that in the following analysis, the downsampling factor M will be set equal to one in order to simplify the notation, since the actual value of M does not affect the analysis in any way.
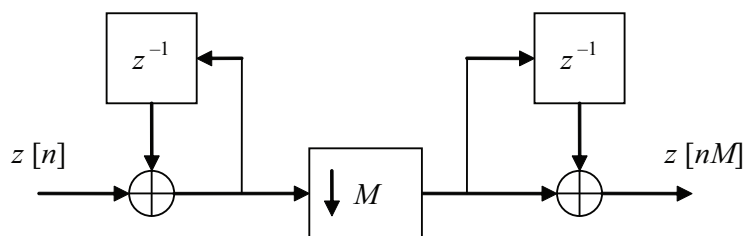
Figure 3.4: First-order CIC filter

3.4   Carrier Tracking Loop

The Electra carrier tracking loop must be able to acquire and track the carrier phase of the received signal reliably when the signal is a residual carrier signal, a suppressed carrier signal, or a carrier-only signal and when the received signal strength varies over several orders of magnitude and the frequency offsets vary up to ± 10 kHz. In addition, the carrier tracking loop should operate over the full range of possible symbol rates from 1 ksps to 4 Msps and over the full range of CIC filter decimated sampling rates. In order to meet these requirements the carrier tracking loop can operate as either a traditional PLL or as a Costas PLL, both of which are second-order with a bandwidth that is programmable from 10 Hz to 10 kHz. An introduction to the analysis and design of PLLs and Costas loops is provided in Appendix B. Note that the carrier tracking loop operates as a PLL when the received signal is a residual carrier signal, while it operates as a Costas loop when the received signal is a suppressed carrier signal. A functional diagram of the carrier tracking loop is shown in Figure 3.5.

65
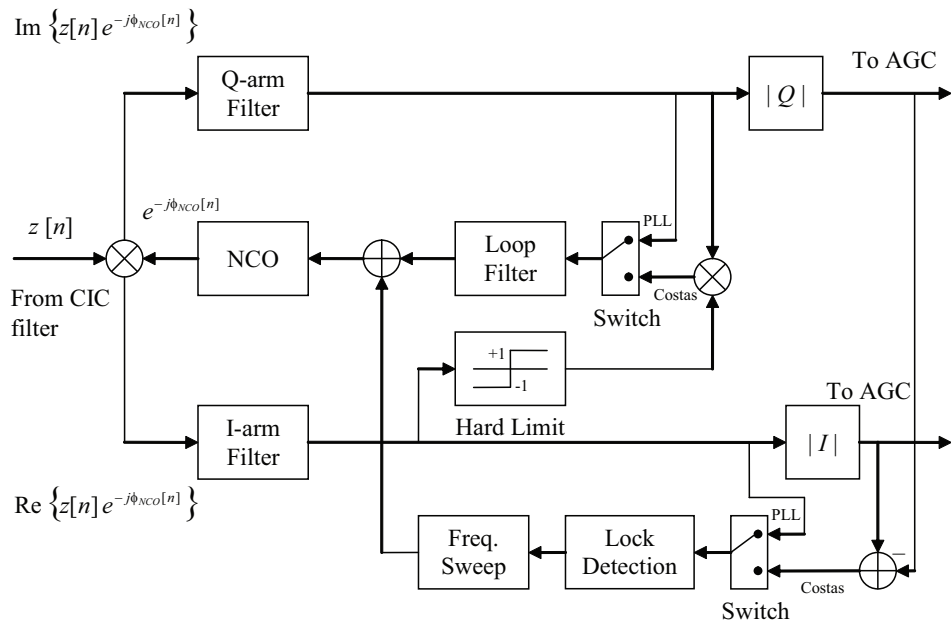
Figure 3.5: Carrier tracking loop with frequency sweep and lock detection

The input to the carrier tracking loop is the complex baseband signal $z[nM]$ that has been downsampled and decimated. The complex baseband signal is multiplied by the complex output of the NCO and the product is split into an in-phase or real component and a quadrature-phase or imaginary component. Both the in-phase and quadrature-phase signals are filtered by identical lowpass filters.

The lowpass filter outputs are used to form the input to the loop filter. In the PLL mode, the error signal which drives the loop filter and sets the frequency and phase of the NCO is derived solely from the quadrature-phase component of the residual carrier signal. In the Costas loop mode, the error

66

signal is corrected by the in-phase component of the suppressed carrier signal. The Costas loop is actually a hard-limited or polarity type Costas loop, where a hard limit is applied to the in-phase signal component. It has been shown that the optimal phase estimator requires a nonlinearity following the in-phase arm filter, where the nonlinearity is given by the hyperbolic tangent function [44]:

$$\tanh\left(K\frac{E_b}{N_0}\right)$$

where K is a scale factor and E_b/N_0 is the bit energy-to-noise density ratio. For large values of the argument, the hyperbolic tangent function approaches the polarity or sign of the argument. Hence, the nonlinearity can be implemented with a hard limiter, as shown in Figure 3.5.

Note that all adders and multipliers in the tracking loop are pipelined in order to maximize the throughput rate. This results in additional delay in the loop following all adders and multipliers, which can affect the overall loop transfer function. However, if the delay is less than $1/B_L$, where B_L is the loop bandwidth, then the loop transfer function remains unchanged. This is the case for Electra.

3.4.1   I/Q-Arm Filter

The in-phase and quadrature-phase signal components, which are given by:

$$
\begin{align}
I[n] &= \operatorname{Re}\left\{z[n]e^{-j\phi_{NCO}[n]}\right\} \tag{3.24}\\
Q[n] &= \operatorname{Im}\left\{z[n]e^{-j\phi_{NCO}[n]}\right\} \tag{3.25}
\end{align}
$$

67

are lowpass filtered by identical arm filters, whose purpose is to remove the second harmonic of the carrier frequency and to reduce the noise in the carrier tracking loop, without significantly reducing the signal power. The arm filters are implemented as discrete, first-order lowpass Butterworth filters, with a programmable cutoff frequency. The cutoff frequency that minimizes the tracking loop error can be shown to be approximately equal to the symbol rate for the NRZ encoded data [64]. Hence, the discrete-time cutoff frequency ω_c is given by:

$$\omega_c = \frac{S_R}{f_s/2} \tag{3.26}$$

where S_R is the symbol rate and f_s is the sampling frequency of the carrier tracking loop.

The transfer function of a discrete-time, first-order, lowpass Butterworth filter is given by:

$$G(z) = G_2 \frac{1 + z^{-1}}{1 - G_1 z^{-1}} \tag{3.27}$$

where G_1 and G_2 are the gains associated with the filter. The corresponding linear, constant coefficient difference equation is given by:

$$y[n] = G_2\big(x[n] + x[n-1]\big) + G_1 y[n-1] \tag{3.28}$$

where $x[n]$ is the input to the filter and $y[n]$ is the output of the filter. In order to increase the throughput rate, the arm filter is pipelined and the feedback portion of the filter has two delays instead of one. Hence, an additional stage is added to remove one of the poles in the feedback portion to produce the
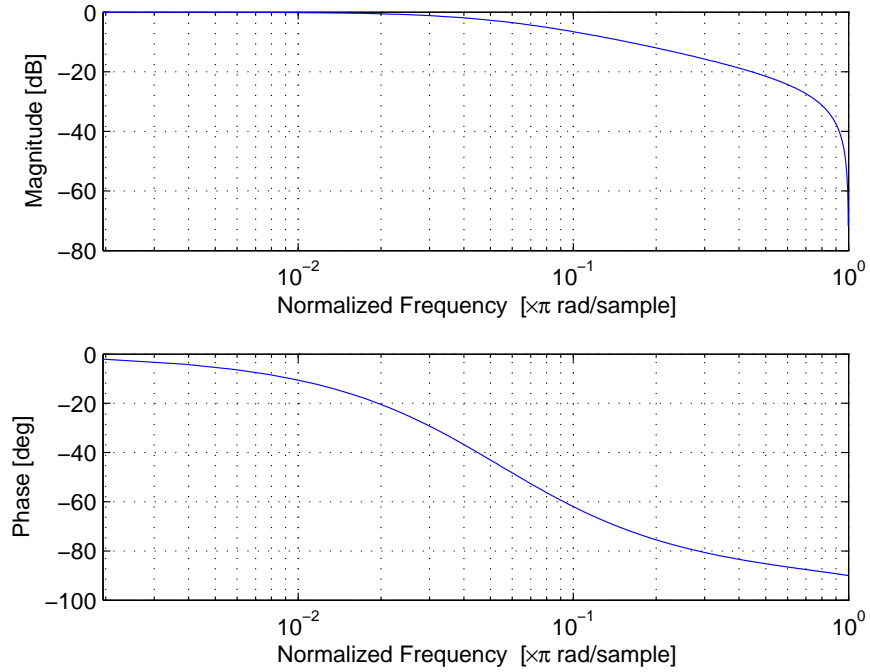
Figure 3.6: Frequency response of the I/Q-arm filters

proper filter response. Thus, the transfer function of the augmented, pipelined Butterworth filter is given by:

$$G(z) = G_2 \, \frac{1 + z^{-1}}{1 - G_1^2 z^{-2}} \, \left(1 + G_1 z^{-1}\right) \tag{3.29}$$

while the linear, constant coefficient difference equation is given by:

$$y[n] = G_2 \Big\{ x[n] + x[n-1] + G_1 \big(x[n-1] + x[n-2] \big) \Big\} + G_1^2 y[n-1] \tag{3.30}$$

The frequency response of the arm filter is shown in Figure 3.6

For the suppressed carrier signal, the output of the arm filters are the

69

following lowpass filtered signals:

$$I[n] = \frac{1}{2} A\, d(nT_s) \cos\left[\theta(nT_s) - \phi_{NCO}(nT_s)\right] + \hat{N}_I(nT_s) \qquad (3.31)$$

$$Q[n] = \frac{1}{2} A\, d(nT_s) \sin\left[\theta(nT_s) - \phi_{NCO}(nT_s)\right] + \hat{N}_Q(nT_s) \qquad (3.32)$$

while for the residual carrier signal, the output of the arm filters are:

$$
\begin{aligned}
I[n] &= \frac{1}{2} A\, \cos\left[\delta d(nT_s) + \theta(nT_s) - \phi_{NCO}(nT_s)\right] + \hat{N}_I(nT_s) \\
&= \frac{1}{2} A \cos\delta \cos\left[\theta(nT_s) - \phi_{NCO}(nT_s)\right] - \\
&\quad \frac{1}{2} A\, d(nT_s)\sin\delta \sin\left[\theta(nT_s) - \phi_{NCO}(nT_s)\right] + \hat{N}_I(nT_s) \quad (3.33) \\
Q[n] &= \frac{1}{2} A\, \sin\left[\delta d(nT_s) + \theta(nT_s) - \phi_{NCO}(nT_s)\right] + \hat{N}_Q(nT_s) \\
&= \frac{1}{2} A\, d(nT_s)\sin\delta \cos\left[\theta(nT_s) - \phi_{NCO}(nT_s)\right] - \\
&\quad \frac{1}{2} A \cos\delta \sin\left[\theta(nT_s) - \phi_{NCO}(nT_s)\right] + \hat{N}_Q(nT_s) \qquad (3.34)
\end{aligned}
$$

where

$$\theta(nT_s) = 2\pi n \frac{df}{F_s} + \theta_{in}(nT_s) + \theta_{AGC}(nT_s) \qquad (3.35)$$

and where $\hat{N}_I$ and $\hat{N}_Q$ are the lowpass filtered noise components. Note that in Equations 3.33 and 3.34, the residual carrier signal has been expanded into a residual carrier component and a data component, as described in Appendix A.

3.4.2   Loop Filter

A second-order tracking loop will have a first-order loop filter, as explained in Appendix B. For the Electra, the loop filter is a one-pole filter with

the following transfer function:

$$F(z) = F_1 + \frac{F_2}{1 - z^{-1}} \tag{3.36}$$

The corresponding linear, constant coefficient difference equation of the loop filter is given by:

$$y[n] = (F_1 + F_2)x[n] - F_1 x[n-1] + y[n-1] \tag{3.37}$$

The filter coefficients F_1 and F_2 are programmable parameters that determine the tracking loop bandwidth B_L and are given by:

$$F_1 = \frac{8}{3} \times B_L \quad \text{and} \quad F_2 = \frac{32}{9} \times B_L^2 \times T_s \tag{3.38}$$

The single-sided tracking loop bandwidth B_L is related to the natural frequency ω_n and the damping ratio ζ by [16]:

$$B_L = \frac{1}{2\pi} \frac{\int_0^\infty |H(\omega)|^2 \, d\omega}{|H(0)|^2} = \frac{\omega_n \zeta}{2} \left(1 + \frac{1}{4\zeta^2}\right) \text{Hz} \tag{3.39}$$

where $H(\omega)$ is the closed-loop system transfer function. Thus, the natural frequency ω_n and the damping ratio ζ determine the loop bandwidth, which in turn determines the loop filter parameters F_1 and F_2. Thus, the purpose of the loop filter is to control the transient and steady-state performance of the carrier tracking loop by controlling the natural frequency and damping ratio. Note that the natural frequency and damping ratio are coupled to the dynamic response of the AGC, which applies a time-varying amplification to the received signal power [16].

71

When the carrier tracking loop is operating in lock, a linear analysis can be performed as explained in Appendix B. This allows the steady-state performance to be estimated for a particular input, using the final value theorem for a discrete-time system:

$$\lim_{n\to\infty} e[n] = \lim_{z\to1}(1 - z^{-1})E(z) \tag{3.40}$$

where $e[n]$ is the phase error and $E(z)$ is the z-transform of $e[n]$. The phase error transfer function of the carrier tracking loop is given by:

$$E(z) = \frac{1}{1 + G(z)F(z)N(z)}\, \Phi(z) \tag{3.41}$$

where $\Phi(z)$ is the z-transform of the input phase, $G(z)$ is the arm filter transfer function, $F(z)$ is the loop filter transfer function, and $N(z)$ is the NCO transfer function, which can be modeled as an integrator:

$$N(z) = \frac{z^{-1}}{1 - z^{-1}} \tag{3.42}$$

Thus, the phase error transfer function becomes:

$$E(z) = \frac{(1 - z^{-1})^2\,(1 - G_1 z^{-1})}{G_2\, z^{-1}\,(1 + z^{-1})\,(F_1 + F_2 - F_1 z^{-1})}\, \Phi(z) \tag{3.43}$$

The steady-state phase error for a phase step input, a frequency step input, and a frequency ramp input can then be found by applying the final value theorem. The results are summarized in Table 3.1, which shows that for a phase step input and a frequency step input, the steady-state error is zero. Note that a frequency step input corresponds to a signal with a constant

Table 3.1: Steady-state error for the Electra tracking loop

Input Type	z-Transform	Steady-State Error
Phase step	$\frac{1}{(1-z^{-1})}\Delta\Phi$	0
Frequency step	$\frac{T_s z^{-1}}{(1-z^{-1})^2}\Delta\omega$	0
Frequency ramp	$\frac{T_s^2 z^{-1}(1+z^{-1})}{(1-z^{-1})^3}\Delta R$	$\frac{T_s^2(1-G_1)}{G_2\,F_2}\Delta R$

Doppler shift. A more realistic input is the frequency ramp input, which corresponds to the case of an approaching spacecraft, where the accelerated motion between the transmitter and the receiver leads to a changing Doppler shift. As Table 3.1 shows, the second-order Electra tracking loop can track such a signal with a finite steady-state error. The magnitude of the error depends on the tracking loop gains and the Doppler rate. If the steady-state error is sufficiently small, the increased complexity of a third-order loop, which has zero steady-state error for a frequency ramp input, may not be justified.

In order to meet the performance criteria, the Electra specifications require that the bandwidth B_L and the sample period T_s are given by:

$$10\,\text{Hz} \leq \quad B_L \quad \leq 10\,\text{kHz} \tag{3.44}$$

$$\frac{1}{F_s}\ \mu\text{s} \ \leq \quad T_s \quad \leq \frac{128}{F_s}\ \mu\text{s} \tag{3.45}$$

The frequency response of the loop filter is shown in Figure 3.7 for tracking loop bandwidths of 0.1 kHz, 1 kHz, and 10 kHz.
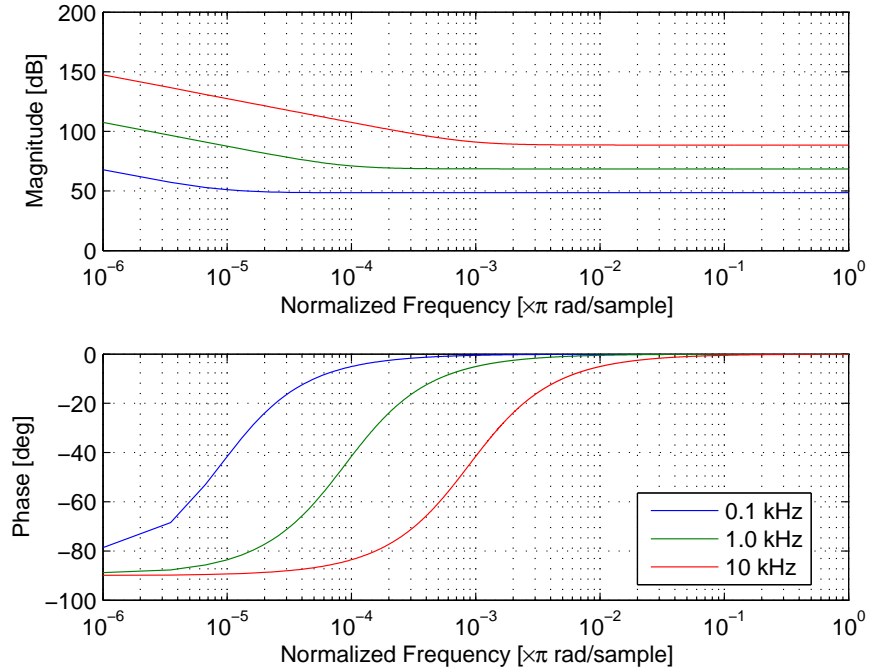
Figure 3.7: Frequency response of the loop filter

3.4.3 Numerically Controlled Oscillator

The NCO acts as an integrator and is a digital version of the voltage controlled oscillator (VCO), which is described in Appendix B. The purpose of the NCO is to drive the phase error to zero, such that when the tracking loop is operating in lock, the NCO phase $\phi_{NCO}[n]$ tracks the phase $\theta(nT_s)$ of the received signal. The instantaneous frequency of the NCO is the sum of the output of the loop filter and the output of the frequency sweep algorithm. The integrated phase estimate, which is in the unit of cycles, is used to form the complex output $e^{-j\phi_{NCO}[n]}$ of the NCO, which is calculated from sine and

74

cosine look-up tables. The look-up tables use only the eight most significant fractional bits of the phase estimate, which provides a reasonable trade-off between low spurious noise and memory required to store the table.

When the carrier tracking loop is operating in the locked mode, the phase error is approximately zero and the in-phase and quadrature-phase signals given by Equations 3.31 and 3.32 for the suppressed carrier case reduce to:

$$I[n] = \frac{1}{2} A \, d(nT_s) + \hat{N}_I(nT_s) \tag{3.46}$$

$$Q[n] = \hat{N}_Q(nT_s) \tag{3.47}$$

Thus, for the suppressed carrier case, the in-phase signal contains the data signal plus noise, while the quadrature-phase signal contains only noise. The equivalent in-phase and quadrature-phase signals for the residual carrier case given by Equations 3.33 and 3.34 reduce to:

$$I[n] = \frac{1}{2} A \, \cos \delta + \hat{N}_I(nT_s) \tag{3.48}$$

$$Q[n] = \frac{1}{2} A \, d(nT_s) \sin \delta + \hat{N}_Q(nT_s) \tag{3.49}$$

Consequently, when the carrier tracking loop is operating in lock for the residual carrier case, the in-phase signal contains the demodulated carrier plus noise, while the quadrature-phase signal contains the data signal plus noise.

3.4.4 Frequency Sweep and Lock Detection

The Electra employs a frequency sweep and lock detection algorithm in order to aid the carrier tracking loop in acquiring phase and frequency

lock. The frequency sweep and lock detection algorithm can operate in two different modes, as illustrated in Figure 3.5. In the PLL mode, the input to the lock detector is the in-phase signal $I[n]$ given by Equation 3.33. This signal oscillates about a near-zero mean value when the tracking loop is operating in the unlocked state. As the tracking loop acquires phase lock, the in-phase signal reduces to Equation 3.48, which has a positive dc-component and thus acts as an indicator for lock. In the Costas loop mode, the input to the frequency sweep and lock detection algorithm is the difference between the magnitudes of the in-phase and quadrature-phase signals $\big|I[n]\big| - \big|Q[n]\big|$ given by:

$$\big|I[n]\big| - \big|Q[n]\big| = \frac{1}{2}A\bigg\{\Big|\cos\big[\theta(nT_s) - \phi_{NCO}(nT_s)\big]\Big| -$$

$$\Big|\sin\big[\theta(nT_s) - \phi_{NCO}(nT_s)\big]\Big|\bigg\} + \big|\hat{N}_I(nT_s)\big| - \big|\hat{N}_Q(nT_s)\big| \quad (3.50)$$

Again, the signal oscillates about a near-zero mean value when the tracking loop is operating in the unlocked state. When the tracking loop acquires phase lock, Equation 3.50 reduces to:

$$\big|I[n]\big| - \big|Q[n]\big| = \frac{1}{2}A + \big|\hat{N}_I(nT_s)\big| - \big|\hat{N}_Q(nT_s)\big| \quad (3.51)$$

The signal now has a positive dc-component and can thus be used as an indicator for lock.

The algorithm sweeps through a given range of NCO frequencies at a given sweep rate. The frequency sweeping is accomplished in discrete increments that are maintained for a specified period of time. An estimate of the

76

input power to the lock detector is obtained by averaging a specified number of samples of data over each frequency increment interval. The lock detector output signal is then compared with a programmable threshold to determine if the carrier tracking loop is in lock. The duration of each frequency increment and the lock detector threshold are functions of E_b/N_0 and the tracking loop bandwidth. The frequency sweep and lock detection algorithm is illustrated in Figure 3.8.

The frequency sweep algorithm passes through the sweep range in increments f_{step} that are selected to be within the range [64]:

$$\frac{B_L}{4} \leq f_{step} \leq \frac{B_L}{2} \qquad (3.52)$$

where B_L is the tracking loop bandwidth. This is done in order to ensure that between the frequency increments there are no frequencies that fall outside of the tracking loop bandwidth that are not directly sampled. In general, the frequency increment is chosen to be approximately $B_L/4$ so that the frequency offset while sweeping is no greater than $B_L/2$. This represents a general rule of thumb for reliable acquisition when the loop SNR is 13 dB or better [64].

The number of averaging samples in each frequency increment used to estimate the signal power was determined empirically. Specifically, for lock stability, the number of averaging samples was chosen such that the integrator output was as consistent as possible [64]:

The minimum possible number of averaging samples was evident for a given noise level when frequent large scale fluctuations in the
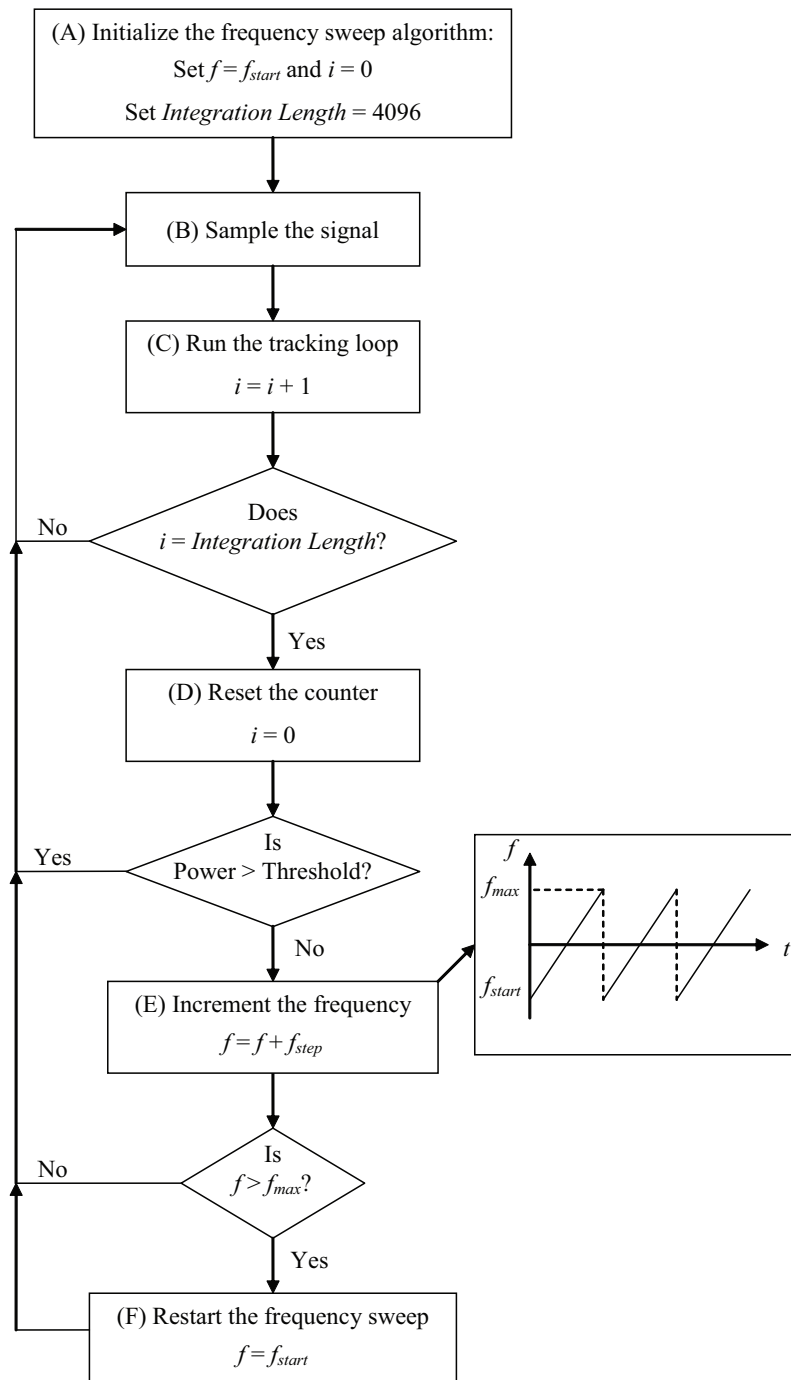
Figure 3.8: Frequency sweep and lock detection algorithm

sampled integrator output would appear when the number of averaging samples was reduced by one level. Once the number of averaging samples was determined to be stable in the noise only case, as indicated by no loss of lock in any observable window, Doppler shifts were added to the signal and lock stability was monitored. Under noise and Doppler shift conditions, a value for the number of averaging samples, which was always greater than or equal to the value for the noise only case, was determined to be stable if the average time between occurrences of loss of lock was not less than 35 minutes. This value was chosen as greater than double the expected time window for communications between Mars orbital and surface-based elements.

The value of the threshold is critical for tracking stability. It is chosen such that the probabilities of false lock and false loss of lock in the noisy environment are balanced. It was determined empirically that the optimal value of the threshold was approximately half the minimum observed integrator output at the end of each interval while in lock. That is, a threshold value [64]:

chosen as evenly between the spurious lows in the integrator output and the spurious highs in the absence of a signal, best preserved lock stability while minimizing the occurrence of false lock in a pure noise, no carrier environment. This level was well estimated by a value taken to be approximately half the minimum observed integrator output.

3.5 Automatic Gain Control

The AGC circuit controls the voltage level input to the A/D converter, based on a control voltage signal generated digitally in the Electra. The AGC is based on a single feedback control loop design, as shown in Figure 3.9. The inputs to the AGC are the magnitudes of the in-phase and quadrature-phase signals from the carrier tracking loop, as shown in Figure 3.5 and as given by Equations 3.31–3.34. The digital AGC error signal is generated from the tracking loop arm filter outputs $|I|$ and $|Q|$ as follows:

$$E_{AGC} = K \left(K_0 - \sqrt{I^2 + Q^2} \right) \tag{3.53}$$

where K_0 is the desired average output magnitude $\sqrt{I^2 + Q^2}$ from the tracking loop arm filters and K is a gain factor that controls the time constant of the AGC and the variance of the resulting amplitude gain estimate. A reasonable compromise between a fast AGC response time and a low noise gain estimate occurs when $K = 10^{-4}$ [64]. The AGC error signal is filtered by a first-order, lowpass Butterworth filter, whose frequency response is shown in Figure 3.10.
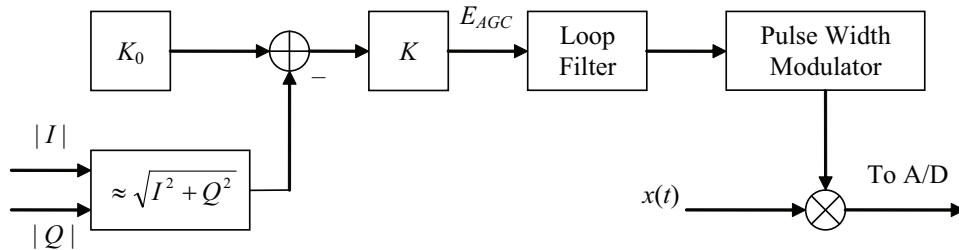
Figure 3.9: AGC circuit
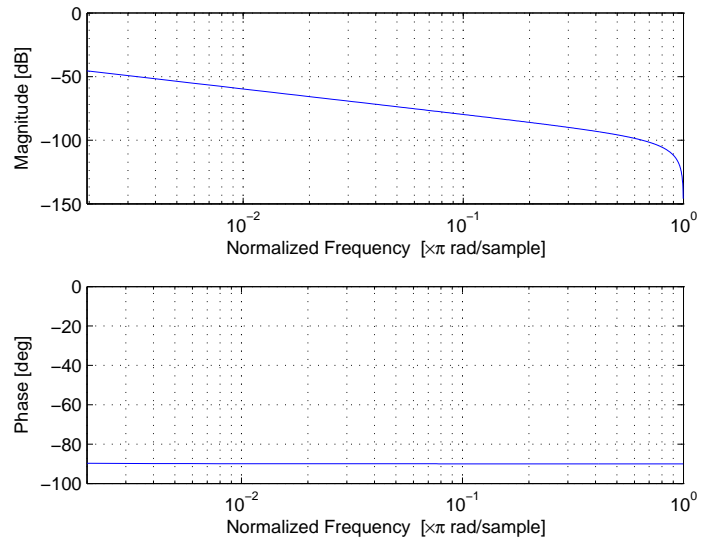
Figure 3.10: Frequency response of the AGC lowpass filter
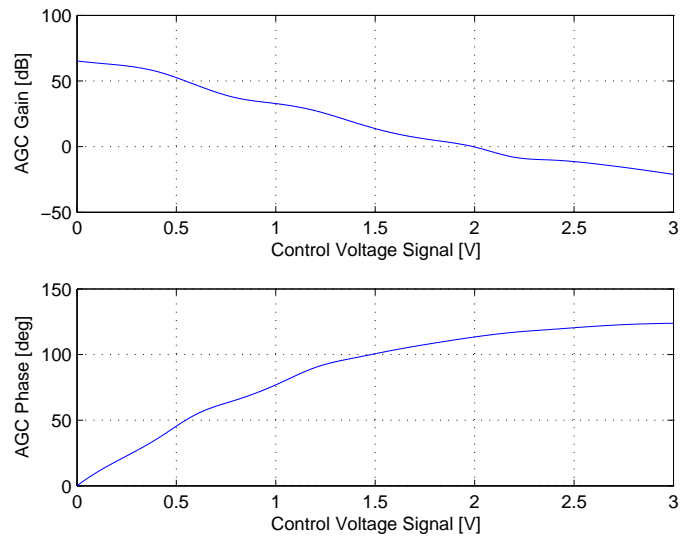
Figure 3.11: AGC gain and phase contribution

The resulting AGC control voltage error signal determines the level of the AGC gain supplied to the received signal, as shown in Figure 3.11. The figure also shows the significant AGC phase contribution, which acts as an additive bias to the phase of the received signal.

3.6 Electra Measurements

The Electra provides measurements of four observables that are of principal interest for navigation purposes, namely:

1. The accumulated phase estimate $\phi(T)$ from the NCO, which is accumulated over a specified count time T, usually between 10–20 seconds.

2. The in-phase signal $I[n]$ and the quadrature-phase signal $Q[n]$, which allows the SNR and the total received power to be estimated.

3. The system noise temperature T_{sys}, which allows the thermal noise density N_0 to be estimated.

The in-phase signal $I[n]$ and the quadrature-phase signal $Q[n]$ given by Equations 3.46–3.49 contain the data signal, as previously explained, and are fed to the digital data transition tracking loop (DTTL) for decoding using either Manchester decoding for the residual carrier mode or 3-bit soft decision Viterbi decoding for the suppressed carrier mode. In addition, these 13-bit measurements can also be used to estimate the SNR and the bit energy-to-noise density ratio E_b/N_0, as illustrated in Figure 3.12. Combined with a
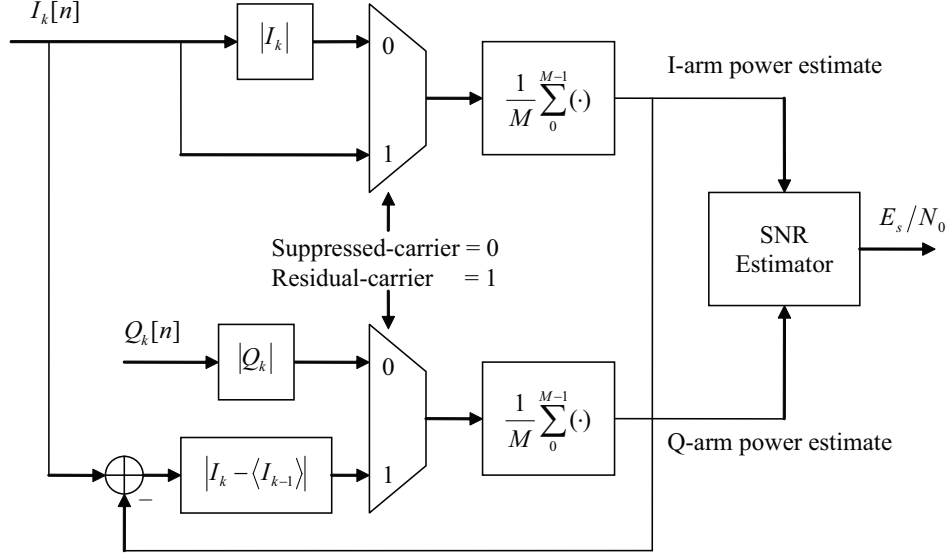
Figure 3.12: SNR estimator

measurement of the system noise temperature T_{sys}, the received signal strength indicated (RSSI) and the total received power P_{rt} can be estimated.

3.6.1 SNR Estimation for the Suppressed Carrier Case

In the suppressed carrier mode, the input to the SNR estimator comprises time-averaged samples of the magnitudes of the in-phase and quadrature-phase signals, as given by:

$$\langle I_k \rangle \ = \ \frac{1}{M} \sum_{m=0}^{M-1} \big| I(kM - n) \big| \tag{3.54}$$

$$\langle Q_k \rangle \ = \ \frac{1}{M} \sum_{m=0}^{M-1} \big| Q(kM - n) \big| \tag{3.55}$$

83

Note that the in-phase signal contains the data signal plus noise, while the quadrature-phase signal contains only noise. Thus, $\langle I_k \rangle$ is related to the data signal plus noise power, while $\langle Q_k \rangle$ is related to the noise power. If the in-phase signal is represented by:

$$I[n] = \pm A + v[n] \tag{3.56}$$

where A is the average signal amplitude and $v[n]$ is the arm filter noise with RMS value $\sigma_n = \sqrt{E\{v[n]^2\}}$, then as shown by Satorius [50], the following approximation for $\langle I_k \rangle$ can be made:

$$\langle I_k \rangle \cong \sqrt{\frac{2}{\pi}} \sigma_n \left\{ e^{-SNR/2} + \sqrt{\frac{\pi}{2}} \cdot \sqrt{SNR} \cdot \mathrm{erf}\left(\sqrt{\frac{SNR}{2}} \right) \right\} \tag{3.57}$$

where erf is the error function. If the total number of accumulated samples M is sufficiently large and if Gaussian receiver noise is assumed, then $\langle Q_k \rangle$ can be approximated by:

$$\langle Q_k \rangle \cong \sqrt{\frac{2}{\pi}} \sigma_n \tag{3.58}$$

The ratio $\langle I_k \rangle / \langle Q_k \rangle$ can then be represented as:

$$\frac{\langle I_k \rangle}{\langle Q_k \rangle} \cong \left\{ e^{-SNR/2} + \sqrt{\frac{\pi}{2}} \cdot \sqrt{SNR} \cdot \mathrm{erf}\left(\sqrt{\frac{SNR}{2}} \right) \right\} \tag{3.59}$$

Hence, given measurements of $\langle I_k \rangle$ and $\langle Q_k \rangle$, the SNR can be estimated using a table look-up procedure, where smoothed measurements of $\langle I_k \rangle / \langle Q_k \rangle$ have been collected for different symbol SNRs and the table created by curve fitting the measurements.

Finally, the bit energy-to-noise density ratio E_b/N_0 can be calculated

from Equation 2.22, which is repeated below:

$$\text{SNR} = 0.62 \frac{E_b}{N_0} \tag{3.60}$$

3.6.2 SNR Estimation for the Residual Carrier Case

In the residual carrier mode, the input to the SNR estimator comprises time-averaged samples of the in-phase signal and the residual in-phase signal, as given by:

$$\langle I_k \rangle = \frac{1}{M} \sum_{m=0}^{M-1} I(kM - n) \tag{3.61}$$

$$\langle Q_k \rangle = \frac{1}{M} \sum_{m=0}^{M-1} \left| I(kM - n) - \langle I_{k-1} \rangle \right| \tag{3.62}$$

Now, since the in-phase signal contains the demodulated carrier plus noise and since the noise is assumed to have a zero-mean value, $\langle I_k \rangle$ is essentially a constant dc offset, which corresponds to the carrier amplitude. The residual in-phase signal given by $\langle Q_k \rangle$ thus represents the noise power. Again, by assuming that the total number of accumulated samples M is sufficiently large and that the receiver noise is Gaussian, $\langle Q_k \rangle$ can be approximated by:

$$\langle Q_k \rangle \cong \sqrt{\frac{2}{\pi}} \, \sigma_n \tag{3.63}$$

Hence, the ratio $\langle I_k \rangle / \langle Q_k \rangle$ is proportional to the square root of the carrier SNR within the arm filter bandwidth. This can be related to the bit energy-to-noise density ratio E_b/N_0, given the modulation index δ. Thus,

E_b/N_0 can be estimated directly from the ratio $\langle I_k \rangle / \langle Q_k \rangle$ using a table look-up procedure, where the table has been created using smoothed measurements of $\langle I_k \rangle / \langle Q_k \rangle$, collected at different values of E_b/N_0.

3.6.3 Estimation of Total Received Power

The system noise temperature T_{sys} can be estimated from the front-end temperature measurement provided by the Electra transceiver. The thermal noise density N_0 can then be calculated from:

$$N_0 = 10 \log \left(k \, T_{sys} \right) + 30 \tag{3.64}$$

where k is Boltzmann's constant (1.380×10^{-23} J/K) and 30 is a product of the units conversion of N_0 from W/Hz to dBm/Hz.

The bit energy-to-noise density ratio E_b/N_0 and the noise density N_0 can be used to calculate the received signal strength indicated (RSSI) according to the equation [49]:

$$\text{RSSI} = \frac{E_b}{N_0} + N_0 + 10 \log B \tag{3.65}$$

where B is the tracking loop bandwidth. The relationship between RSSI and total received power is shown in Figure 3.13 for data rates between 1–1024 ksps and a tracking loop bandwidth of 1 kHz. The figure shows that for a data rate of 1 ksps, RSSI is a good approximation of the total received power. Furthermore, for higher data rates, RSSI and the total received power essentially differ by a constant. Consequently, with minor adjustments for the data rate, RSSI represents a good approximation of the true total received power [34].

86
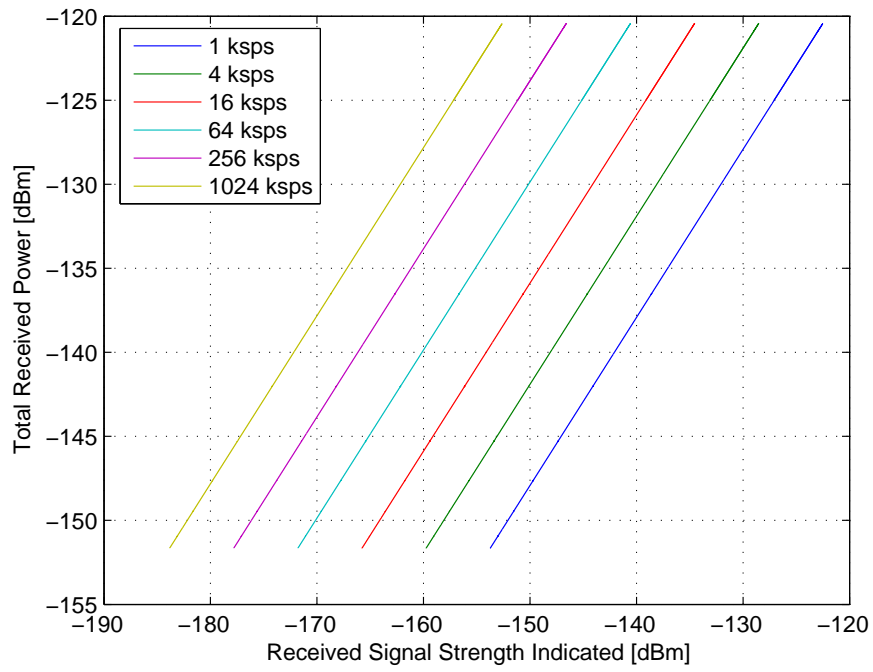
Figure 3.13: Relationship between RSSI and total received power

Chapter 4

Performance Analysis of the Electra

4.1 Introduction

An in-depth analysis of the performance of the Electra transceiver is presented in the following sections. The analysis is based on the detailed dynamic analysis and link budget analysis developed in Chapter 2 and on the high-fidelity MATLAB model of the Electra BPM that was described in Chapter 3. The results of the dynamic analysis and link budget analysis are used to specify the properties of the received signal, which is used as the input to the model of the Electra BPM. The overall link performance, which determines the range at which the communications link can be closed, is considered first. This is followed by an analysis of the acquisition performance of the tracking loop, based on various signal and tracking loop parameters. An analysis of the steady-state tracking performance and the resulting steady-state error is then presented. Finally, a description of the experimental setup needed to test and verify the performance of the Electra EDU in the laboratory is presented.

The performance of the Electra transceiver depends on many widely different parameters, some of which include:

1. Link parameters such as the transmitted power, the transmitter antenna gain, the receiver antenna gain, and the receiver sensitivity.

2. Signal parameters such as the Doppler shift, the Doppler rate, the signal strength, the SNR, the data rate, and the data modulation scheme.

3. Tracking loop parameters such as the tracking loop bandwidth and the tracking loop order.

4. Additive noise sources such as thermal noise, which are modeled, and other noise sources such as USO stability and multipath, which are not modeled.

4.2   Link Performance Parameters

The link performance depends on several link parameters, such as the transmitted power, the transmitter antenna gain, the receiver antenna gain, and the receiver sensitivity. The effect of these parameters on the range at which the link can be closed and communication established between the MAV and the MNO will be considered below.

4.2.1   The Effect of Transmitter Power on Performance

The range at which the link can be closed depends on the transmitted power, as shown in Figure 4.1. Note that the link is considered closed when the total received power is above the -150 dBm threshold, which was determined by hardware tests in the laboratory, as explained in Section 2.4. The figure

89
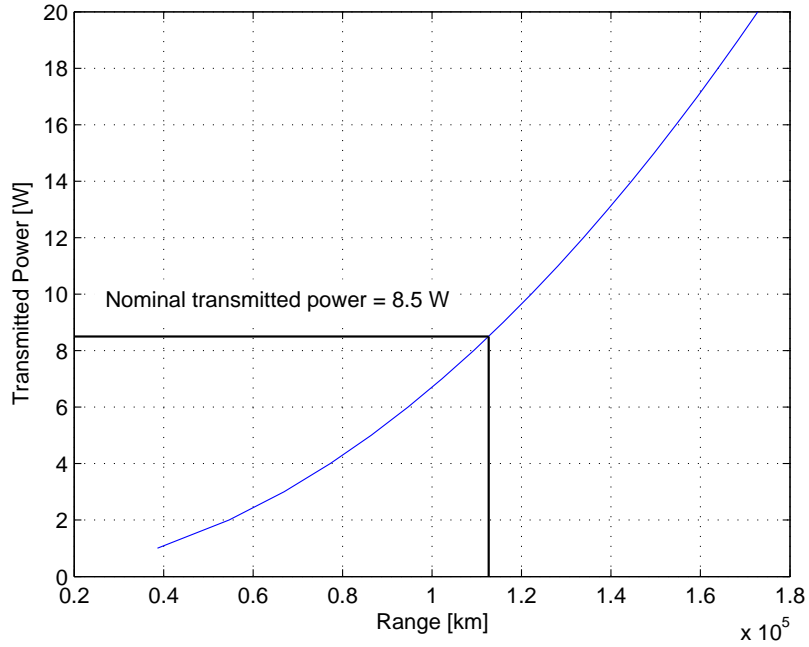
Figure 4.1: Link closure range as a function of transmitted power

confirms the earlier result that the link can be closed at approximately 110,000 km when the transmitted power is 8.5 W. Furthermore, the figure shows that the link closure range tends to respond quadratically to a linear increase in power, which is predominantly a result of the free space path loss, given by:

$$L_s = \left(\frac{4\pi f S}{c} \right)^2 \qquad (4.1)$$

where S is the range, f is the signal frequency, and c is the speed of light.

Figure 4.1 shows that even though the range at which the link can be closed increases as the transmitted power is increased, it does so at a decreasing rate. Fortunately, this effect is small over the range of power levels that the

90

Electra is designed to operate in. Consequently, increasing the transmitted power is an attractive option should it become necessary to substantially boost the range [34].

4.2.2 The Effect of Transmitter Antenna Gain on Performance

The range at which the link can be closed is also dependent on the transmitter antenna gain, as shown in Figure 4.2. Again, the link is considered closed when the total received power is above the -150 dBm threshold. In the nominal case where the transmitter antenna gain is 3.5 dB, the range at which the link can be closed is approximately 110,000 km. The figure shows that the range not only increases as the transmitter antenna gain is increased, but it does so at an increasing rate. This would suggest that increasing the transmitter antenna gain is preferable to increasing the transmitted power in order to boost the range.

There is a significant drawback to increasing the transmitter antenna gain, however. The three UHF patch antennas on the MAV are located on the backshell and separated by 120 deg, as discussed in Section 2.3. Since the MAV is spin-stabilized at 2 rpm, the antennas will actively switch every 10 seconds as they pass in and out of the field of view. If the transmitter antenna gain is increased, the signal nulls between the antennas will become more pronounced, resulting in signal dropouts during weak signal conditions. This condition could prove far more adverse to navigation than a 1 dB loss in antenna gain [34].
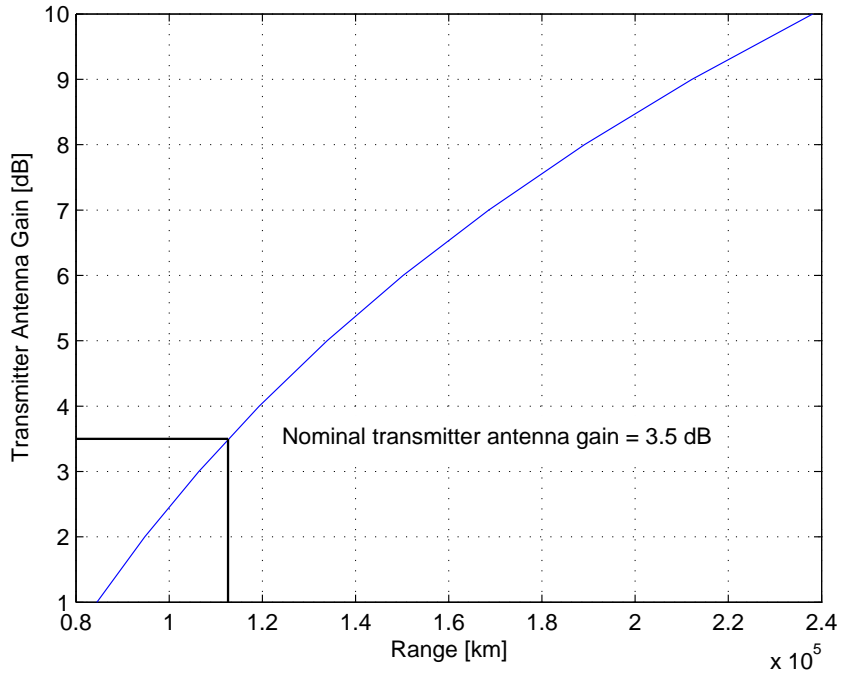
Figure 4.2: Link closure range as a function of transmitter antenna gain

4.2.3 The Effect of System Noise Temperature on Performance

The sensitivity of a radio receiver, including the antennas, the lines, and the pre-amps depends on the overall system noise temperature T_{sys} [34]. The system noise temperature is influenced by the actual physical temperature of the receiver hardware, the sky temperature as seen by the receiver antenna, the line losses, the pre-amp gains as well as many other parameters. Consequently, a model of the system noise temperature for the Electra cannot be developed here, but its effect on the system performance can still be analyzed.

The system noise temperature does not affect the total received power

and hence, has no effect on the range at which the link can be closed. However, it does affect the bit energy-to-noise density ratio E_b/N_0 and the SNR through the thermal noise density N_0, which is given by:

$$N_0 = 10 \log \left(k \, T_{sys} \right) + 30 \tag{4.2}$$

where k is Boltzmann's constant (1.380×10^{-23} J/K) and 30 is a product of the units conversion of N_0 from W/Hz to dBm/Hz.

The effect of system noise temperature on the range at which a BPSK modulated signal with a data rate of 1 ksps has a SNR of 0 dB is shown in Figure 4.3. The figure confirms the previous result, shown in Figure 2.23, that for a BPSK modulated signal with a data rate of 1 ksps and a nominal system noise temperature of 526 K, the range at which the SNR is 0 dB is approximately 33,000 km. (This range is not equivalent to the range at which the link can be closed, which is determined by the total received power. For a 1 ksps BPSK signal, the SNR is approximately -12 dB when the link can be closed, as shown in Figure 2.23.) It can be seen that significant gains in the SNR are achievable for any amount that the system noise temperature can be suppressed below the nominal value of 526 K.

The system noise temperature also plays a significant role in the quality of the Doppler measurement by contributing directly to the phase noise value through the SNR. A model of the one-way thermal phase noise is given by [16]:

$$\phi_{Thermal}(j\omega) = \sqrt{\frac{N_0}{2} \frac{1}{P_{rt}S_r}} \tag{4.3}$$
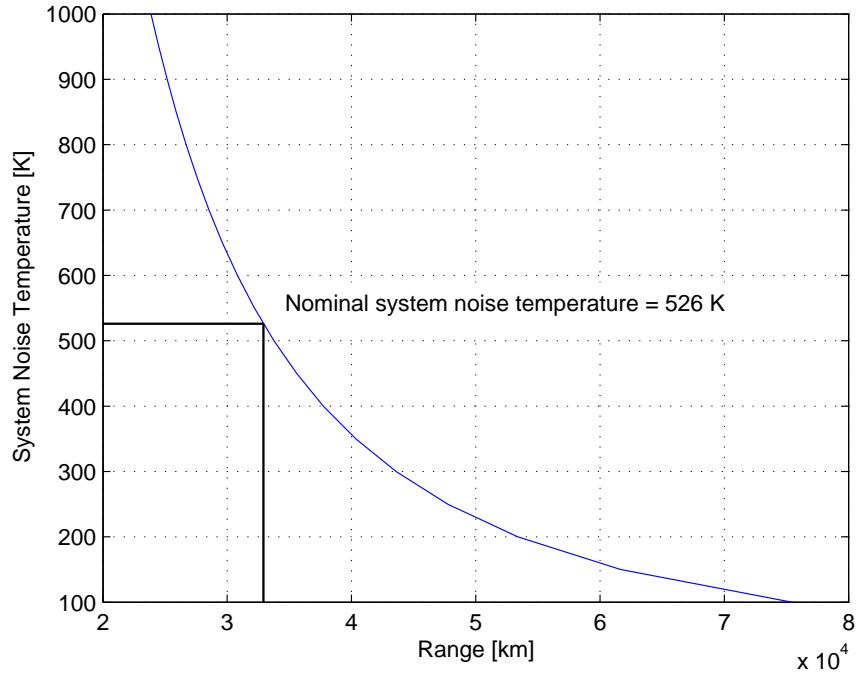
Figure 4.3: The 0 dB SNR range as a function of system noise temperature for a BPSK modulated signal with a data rate of 1 ksps

where P_{rt} is the total received power and S_r is the Costas loop squaring losses. The thermal phase noise is a significant error source in the integrated Doppler measurement. The error can be mitigated by choosing a narrower bandwidth and as a result, admitting less thermal noise into the system. However, as the loop bandwidth is decreased, the tracking loop response becomes more sluggish, which introduces deterministic errors. Consequently, there is a balance that must be achieved in the loop bandwidth for best overall performance. As previously mentioned, one of the measurements provided by the Electra is the

94

system noise temperature T_{sys}, which allows a real-time estimate of the noise density N_0 and hence E_b/N_0 and SNR.

4.3   Acquisition Performance Analysis

The acquisition performance of the Electra carrier tracking loop was tested for a range of BPSK residual carrier signals with different Doppler shifts, SNRs, data rates, and tracking loop bandwidths using the high-fidelity MATLAB model of the Electra BPM that was created by JPL. In addition, the acquisition performance of the tracking loop was compared for residual carrier signals, suppressed carrier signals, and carrier-only signals. The acquisition performance results are based on a Monte Carlo analysis, where the acquisition performance is estimated statistically as the percentage of successful acquisitions from a given number of acquisition attempts. For the analysis presented in the subsections below, 60 simulations were run for each specific acquisition case. For each simulation, a different randomly-generated and normally-distributed noise signal was used, together with a different randomly-generated and uniformly-distributed data modulation signal.

4.3.1   The Effect of Doppler Shift and SNR on Acquisition

The acquisition performance, which is measured as the percentage of successful acquisitions for a given number of acquisition attempts, of the Electra transceiver with a tracking loop bandwidth of 1 kHz is shown in Figure 4.4. The received signal is a BPSK residual carrier signal with a data rate of

95

128 ksps, a SNR that varies from -6 dB to $+2$ dB, and a Doppler shift that varies from 0 Hz to $+10$ kHz. The figure shows that the tracking loop is able to acquire the signal 100% of the time when the SNR is 0 dB and above, up to a Doppler shift of 10 kHz. As the SNR decreases, the acquisition performance worsens; at a SNR of -4 dB, acquisition occurs on average only 30% of the time, while at a SNR of -6 dB and below, acquisition is not possible at all. Thus the ability of the tracking loop to acquire the residual carrier signal is strongly dependent on the SNR but independent of the Doppler shift, over the range of expected values.

A similar set of results are shown in Figure 4.5, which shows the acquisition performance for a BPSK residual carrier signal with a data rate of 128 ksps, when the tracking loop bandwidth is 5 kHz. Again, the SNR varies from -6 dB to $+2$ dB while the Doppler shift varies from 0 Hz to $+10$ kHz. The results confirm that the ability of the tracking loop to acquire the residual carrier signal depends strongly on the SNR but is independent of the Doppler shift. The results also show that the increased bandwidth has improved the acquisition performance slightly. The tracking loop can now reliably acquire the residual carrier signal with a SNR of -3 dB and above, when the tracking loop bandwidth is 5 kHz. In addition, a residual carrier signal with a SNR of -5 dB can be acquired more than 50% of the time.

A consequence of the larger tracking loop bandwidth is that more noise is included in the phase measurement, which can affect the tracking performance and the magnitude of the steady-state error. Thus, once acquisition is

Figure 4.4: Residual carrier acquisition performance as a function of Doppler shift and SNR for a 1 kHz loop bandwidth
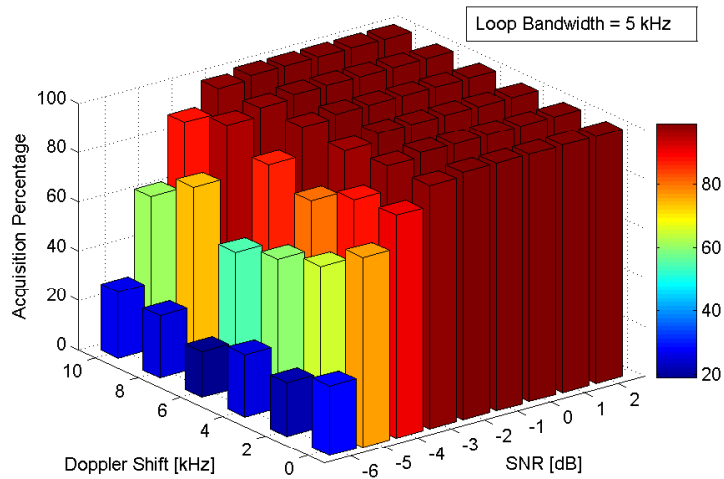
Figure 4.5: Residual carrier acquisition performance as a function of Doppler shift and SNR for a 5 kHz loop bandwidth

established and the receiver is locked onto the signal, the bandwidth should be decreased in order to eliminate some of the noise in the phase measurement, as explained in the following section.

4.3.2 The Effect of Tracking Loop Bandwidth on Acquisition

The acquisition performance of the Electra transceiver for various tracking loop bandwidths between 0.1 kHz and 10 kHz is shown in Figure 4.6. The received signal is a BPSK residual carrier signal with a data rate of 128 ksps, a constant Doppler shift of 2 kHz, and a SNR that varies from -6 dB to $+2$ dB. The figure shows that, in general, the acquisition performance is improved slightly as the tracking loop bandwidth is increased. For example, at a SNR of 0 dB, the signal can be acquired 100% of the time when the tracking loop bandwidth is above 0.5 kHz.

It has been determined analytically by Ely [16], however, that in order to meet the tracking performance requirements of a maximum range rate error of 0.1 mm/s on a 20 second count interval, the tracking loop bandwidth must be 0.1 kHz or less. Thus, if a bandwidth on the order of 1 kHz is used during the acquisition process, it must be reduced to 0.1 kHz once the signal is acquired, in order to minimize the steady-state tracking errors.

The acquisition performance also depends on the parameters of the frequency sweep and lock detection algorithm, as described in Section 3.4. In particular, the step size used in the frequency sweep is highly dependent on the tracking loop bandwidth and, in order to ensure proper performance, the step
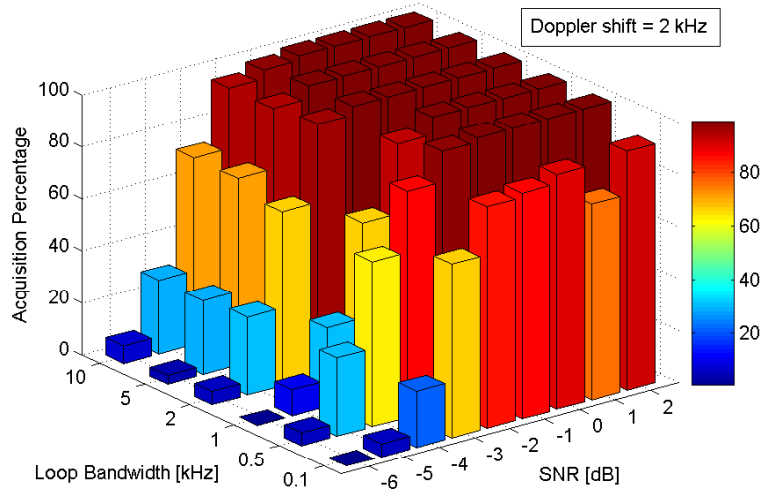
Figure 4.6: Residual carrier acquisition performance as a function of tracking loop bandwidth

size should satisfy the relationship given in Equation 3.52, which is repeated below:

$$\frac{B_L}{4} \leq f_{step} \leq \frac{B_L}{2} \tag{4.4}$$

The step size will also determine the amount of time it takes to sweep through the full frequency range, which should include the entire range of expected Doppler shifts from -10 kHz to $+10$ kHz. The sweep time is given by:

$$T_{sweep} = 4096 \times T_s \times \frac{20\,\text{kHz}}{f_{step}} \tag{4.5}$$

where 4096 corresponds to the integration time used to estimate the signal power in the lock detection algorithm and where T_s is the sample time. The

99

sample time was specified in Equation 3.45, which is repeated below:

$$\frac{1}{F_s} \ \mu\text{s} \ \leq T_s \leq \frac{128}{F_s} \ \mu\text{s} \tag{4.6}$$

Thus, for a tracking loop bandwidth of 1 kHz, the step size will be between 0.25–0.5 kHz and the time it takes to sweep through the full 20 kHz frequency range will be between 8.6 ms and 2.2 s. If the bandwidth is reduced to 0.1 kHz, the sweep time could increase to as much as 21.9 s. This could potentially be a problem, since the spacecraft rotation rate of 2 rpm means that each of the three UHF patch antennas is only visible for 10 seconds at a time. (If the patch antennas are replaced by a single wrap-around antenna, as the current MSL design calls for, then the long sweep time will no longer be a problem.)

4.3.3 The Effect of Data Rate on Acquisition

In the previous sections, the acquisition performance was analyzed for a BPSK residual carrier signal with a data rate of 128 ksps. However, the data rate of the signal that modulates the carrier wave will also affect the acquisition performance. Furthermore, to a large extent, the data rate will determine the required tracking loop bandwidth, as will be shown below.

The acquisition performance for a BPSK residual carrier signal with data rates between 1 ksps and 1024 ksps, when the tracking loop bandwidth is 1 kHz is shown in Figure 4.7. The signal has a constant Doppler shift of 2 kHz and a SNR that varies from −6 dB to +4 dB. The figure shows that
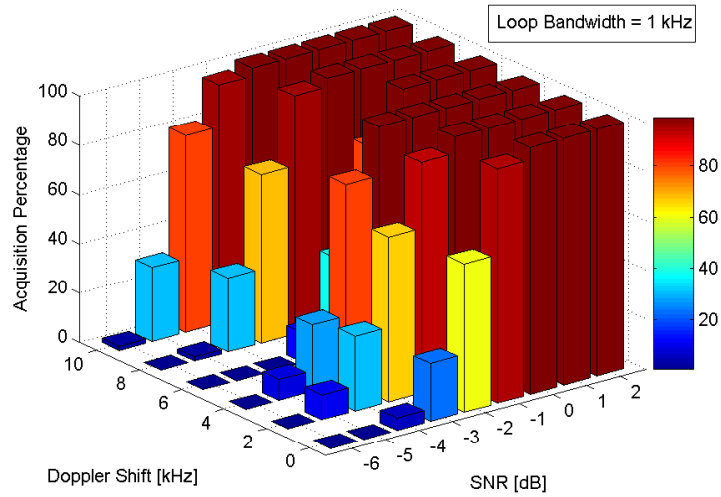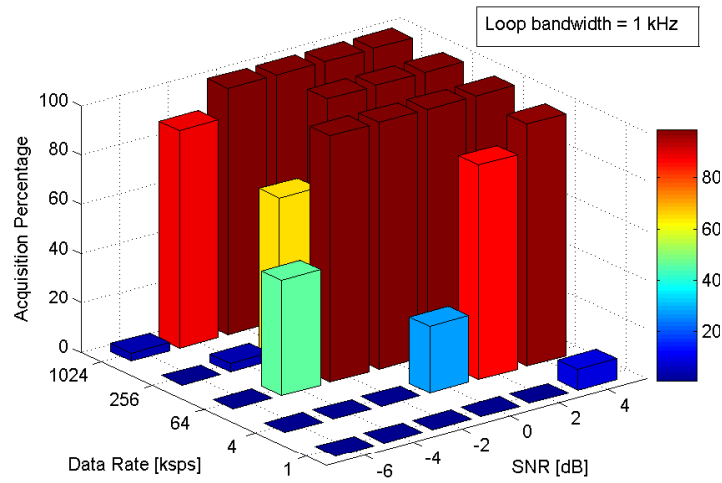
Figure 4.7: Residual carrier acquisition performance as a function of data rate for a 1 kHz tracking loop bandwidth
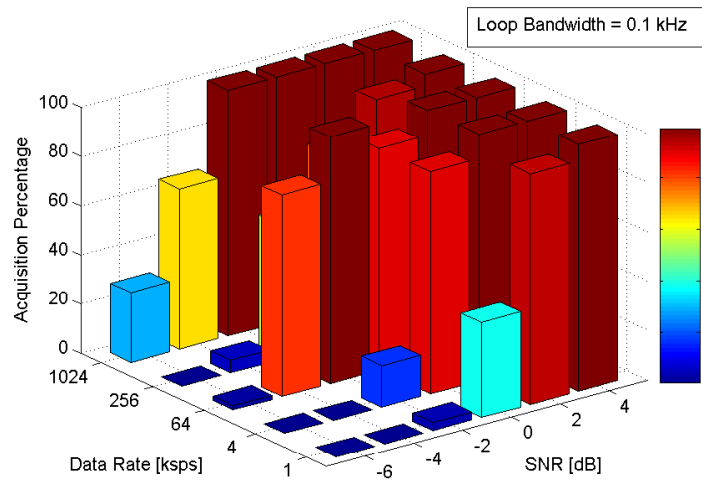
Figure 4.8: Residual carrier acquisition performance as a function of data rate for a 0.1 kHz tracking loop bandwidth

the Electra transceiver is unable to acquire the signal at the lowest data rate of 1 ksps for the range of values of SNR. As the data rate is increased, the acquisition performance improves and at data rates of 64 ksps and above, the performance is identical to the previous results shown in Figure 4.4.

A similar set of results are shown in Figure 4.8, which shows the acquisition performance for a BPSK residual carrier signal with data rates between 1 ksps and 1024 ksps, when the tracking loop bandwidth is decreased to 0.1 kHz. The figure shows that the acquisition performance is improved at the lower data rates of 1 ksps and 4 ksps, where the signal can now be acquired at values of SNR between 0–2 dB.

The improved performance with a narrower tracking loop bandwidth at the lower data rates is associated with the power spectral density (PSD) of the data pulses. As explained in Appendix A, the PSD for a Manchester-encoded data pulse, is given by:

$$P(f) = T_s \frac{\sin^4 \pi f T_s/2}{(\pi f T_s/2)^2} \tag{4.7}$$

where f is the frequency, T_s is the bit duration, and $R_s = 1/T_s$ is the data rate. The PSD for a 1 ksps and a 1024 ksps data rate is shown in Figure 4.9. The two main lobes of the PSD, which contain most of the power in the data signal, have a combined width of 4 kHz for the 1 ksps data rate and a combined width of 4000 kHz for the 1024 ksps data rate. Consequently, the spectral null in the middle of the PSD is much narrower at the lower data rates. The residual carrier signal, which the tracking loop is trying to acquire, lies in the spectral null of the PSD and hence, a lower tracking loop bandwidth

(a) PSD for a 1 ksps data rate

(b) PSD for a 1024 ksps data rate
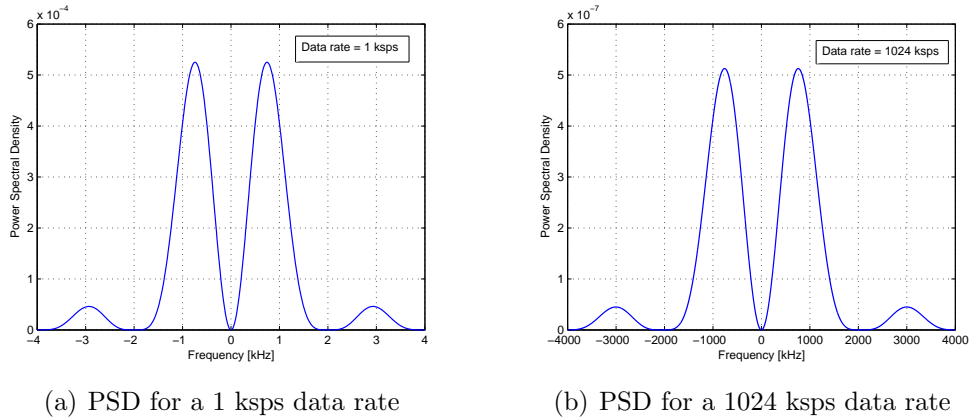
Figure 4.9: Power spectral densities for different Manchester-encoded data rates

is required for the lower data rate, in order to limit the amount of interference within the bandwidth.

4.3.4 Acquisition Performance of Suppressed Carrier Signals

The acquisition performance results presented so far pertain only to residual carrier signals. The Electra transceiver is also able to transmit and receiver suppressed carrier signals, in which case the carrier tracking loop operates in the Costas loop mode, as discussed in Section 3.4.

The acquisition performance for a BPSK suppressed carrier signal with a data rate of 128 ksps, when the tracking loop bandwidth is 1 kHz is shown in Figure 4.10. The SNR varies from 0 dB to +6 dB and the Doppler shift varies from 0 Hz to +10 kHz. The figure confirms the earlier result that the acquisition performance is strongly dependent on the SNR but largely independent of the Doppler shift. Furthermore, the figure shows that the
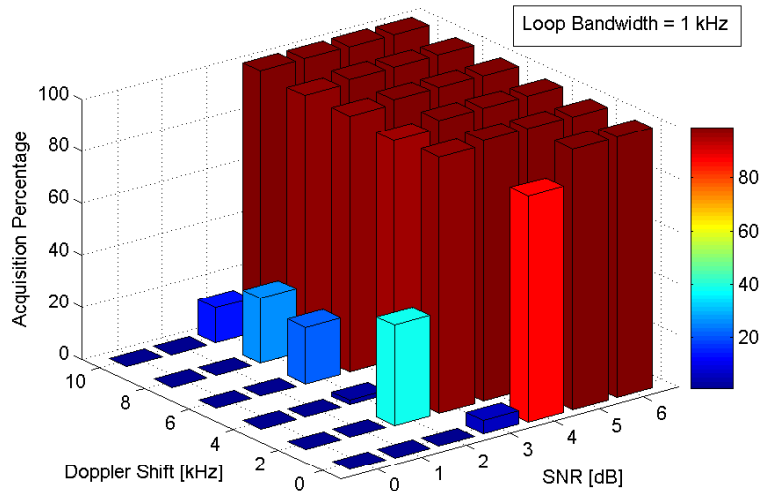
Figure 4.10: Acquisition performance of a suppressed carrier signal

tracking loop can reliably acquire the signal when the SNR is +5 dB and above. This result compares unfavorably to the acquisition performance for a residual carrier signal, which can be reliably acquired at a SNR of 0 dB, as shown in Figure 4.4. This confirms the fact that residual carrier signals can be acquired at a lower SNR than suppressed carrier signals. The reason, as explained in Appendix A, is that a residual carrier signal divides the transmitted power between a carrier signal and a data signal, as opposed to a suppressed carrier signal, which contains only a data signal. It is the carrier signal that improves the acquisition performance and allows the tracking loop to lock onto the received signal in a noisier environment. The drawback, of course, is that the bit error rate of a residual carrier signal is higher than that of a suppressed

104
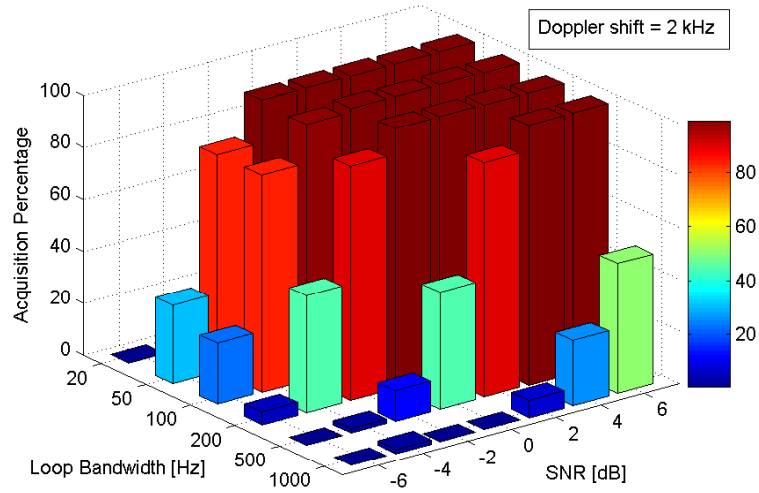
Figure 4.11: Acquisition performance of a carrier-only signal

carrier signal, where all of the transmitted power is contained in the data signal.

4.3.5 Acquisition Performance of Carrier-Only Signals

The Electra transceiver is able to transmit and receive carrier-only signals, in addition to residual carrier signals and suppressed carrier signals. Carrier-only signals can be transmitted at the start of the final approach phase, when the distance between the MAV and the MNO is the greatest, in order to extend the maximum range at which the link can be closed.

The acquisition performance of a carrier-only signal for a range of tracking loop bandwidths between 20 Hz and 1 kHz is shown in Figure 4.11. The

105

signal has a constant Doppler shift of 2 kHz and a SNR that varies from -6 dB to $+6$ dB. The figure shows that the acquisition performance is greatest when the tracking loop bandwidth is on the order of 0.1 kHz, in which case the carrier-only signal can be acquired reliably when the SNR is greater than -4 dB. The improved acquisition performance at the lower tracking loop bandwidths is a consequence of the decrease in noise power allowed into the bandwidth.

4.4   Tracking Performance Analysis

The tracking performance of the Electra transceiver was tested for carrier-only, residual carrier, and suppressed carrier signals for a range of Doppler shifts and SNRs using the high-fidelity Electra MATLAB model. The results are based on a tracking loop bandwidth of 0.1 kHz, which is required in order to meet the navigation performance requirements of a maximum range rate error of 0.1 mm/s on a 20 second count interval, as determined analytically by Ely [16]. The tracking performance is analyzed statistically in terms of the expectation and the variance of the error in the measurement of the Doppler shift. The results are based on a Monte Carlo analysis, where 100 simulations were run for each specific tracking case. For each simulation, a different randomly-generated and normally-distributed noise signal was used, together with a different randomly-generated and uniformly-distributed data modulation signal.

The output of the tracking loop is the accumulated NCO phase, mea-

106
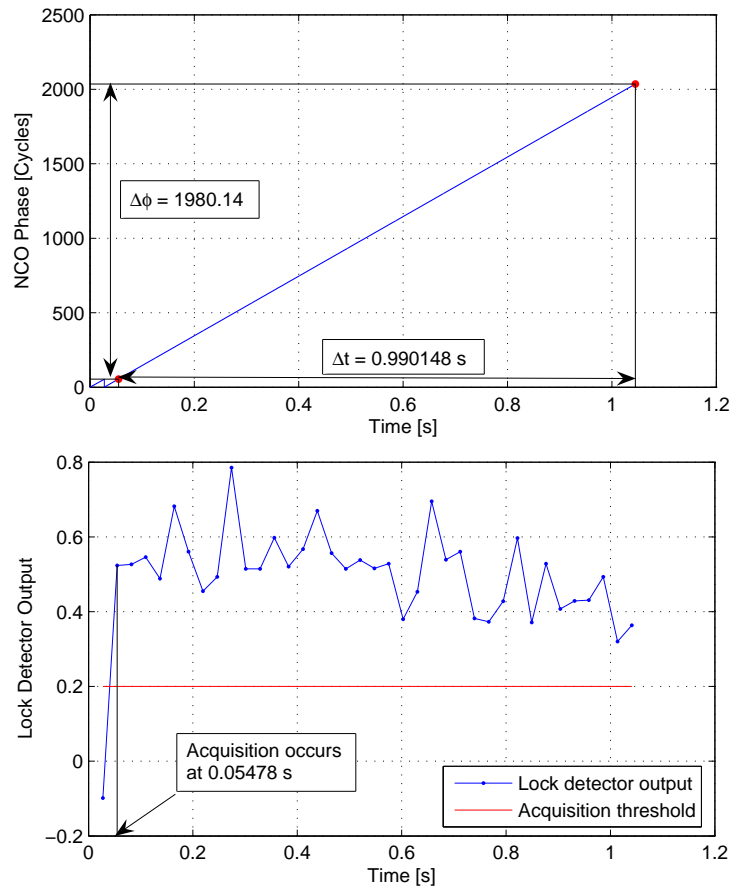
Figure 4.12: Signal acquisition and tracking

sured in cycles from the start of acquisition, as described in Chapter 3 and as shown in Figure 4.12. The Doppler shift, which is the difference of two phase measurements separated by a specified count time, is then given by:

$$\Delta f = \frac{\phi_{NCO}(t_2) - \phi_{NCO}(t_1)}{t_2 - t_1} \tag{4.8}$$

The time interval $(t_2 - t_1)$ between the two phase measurements must be sufficiently large in order to determine the Doppler shift accurately. How-

ever, this increases the run-time of the simulations. In order to determine the Doppler shift accurately, while minimizing the run-time of the simulations, the tracking loop was initially allowed to track the received signal for approximately 0.3 s, which corresponds to a run-time of about 260 s. The resulting accuracy in the measurement of the Doppler shift was not sufficiently high, as described in the following section, and consequently, the tracking time was later increased to 1.2 s, which corresponds to a simulation run-time of approximately 1040 s.

4.4.1   Tracking Performance of Carrier-Only Signals

The tracking performance of the Electra transceiver was tested for a carrier-only signal for a range of Doppler shifts between 0–10 kHz and SNRs between 0–50 dB. This corresponds to the expected operating conditions for the Electra transceiver during final approach, when the received signal is a carrier-only signal, as determined by the approach analysis presented in Chapter 2. The mean error in the measurement of the Doppler shift and the variance of the error are shown in Figures 4.13 and 4.14, respectively, for a range of Doppler shifts and SNRs. Note that these results correspond to a tracking time of approximately 0.3 s. The figures show that the mean error and the variance of the error are essentially independent of the Doppler shift up to 10 kHz, but are strongly dependent on the SNR. Furthermore, there is a bias in the mean error, which increases from about -0.1 mHz at a SNR of 0 dB to about $+0.27$ mHz at a SNR of 50 dB. Finally, the variance tends to decrease

108

Figure 4.13: Mean error of the Doppler shift for a carrier-only signal for a tracking time of 0.3 s
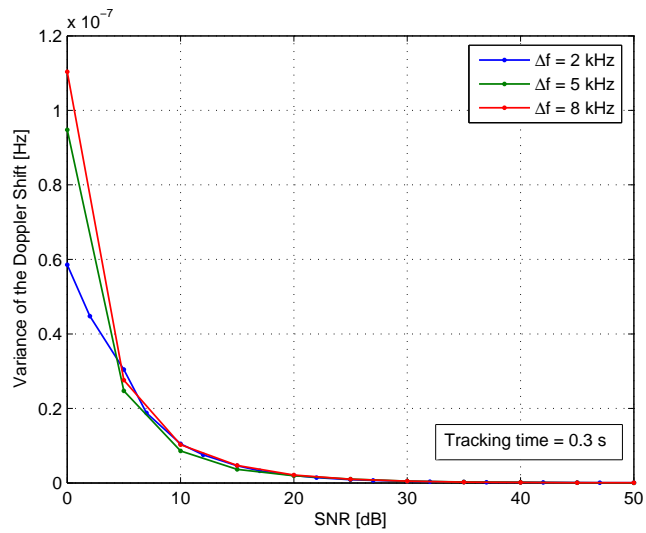
Figure 4.14: Variance of the Doppler shift for a carrier-only signal for a tracking time of 0.3 s

109

rapidly from 0.1 μHz to zero, as the SNR increases from 0 dB to 50 dB.

The navigation performance requirements specify that the maximum allowable range rate error is 0.1 mm/s on a 20 second count interval. The range rate is related to the Doppler shift by Equation 2.8, which is repeated below:

$$\Delta f = -\frac{f_T \dot{r}}{c} \tag{4.9}$$

where f_T is the transmitted signal frequency and c is the speed of light. Thus, the navigation performance requirement translates into a maximum allowable Doppler shift error of 0.146 mHz, which is indicated in Figure 4.13. The figure shows that the error in the Doppler shift satisfies the performance requirements when the SNR is in the range of 0–25 dB. Above a SNR of 25 dB, the mean error is greater than the maximum allowable error.

The error in the measurement of the Doppler shift for each individual simulation is shown in Figure 4.15 as a function of the SNR only, since the error is essentially independent of the Doppler shift up to 10 kHz. The figure shows that the variance in the error decreases as the SNR increases, which is the expected behavior. However, the figure also shows that as the SNR increases, the error approaches a steady value of approximately 0.27 mHz, which is not the expected behavior. The error in the Doppler shift should have a zero mean, since the second-order tracking loop is capable of tracking a constant Doppler shift with zero steady-state error. (The simulations are run with a constant Doppler shift only, due to the short tracking times, which are on the order of 0.3 s.)
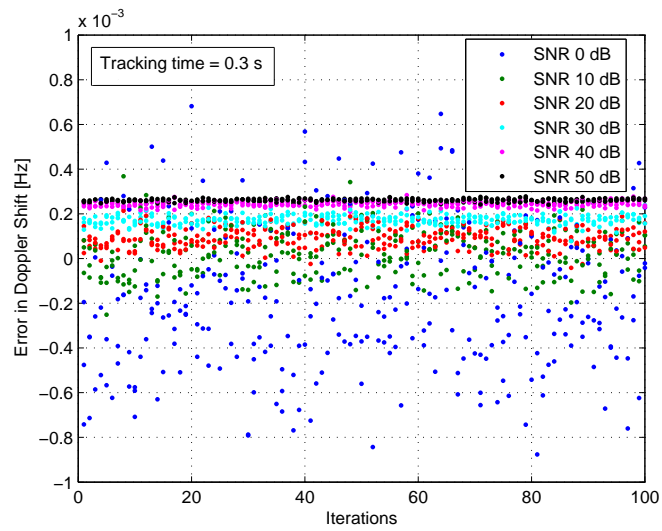
Figure 4.15: Error in the Doppler shift for a carrier-only signal for a tracking time of 0.3 s
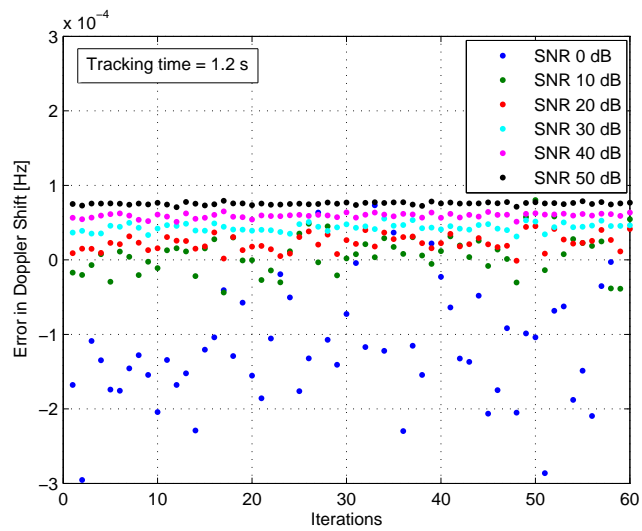
Figure 4.16: Error in the Doppler shift for a carrier-only signal for a tracking time of 1.2 s

In an attempt to investigate the cause of the non-zero mean error, it was discovered that the magnitude of the error in the measurement of the Doppler shift could be reduced substantially if the tracking time was increased. Increasing the tracking time corresponds to increasing the time interval $(t_2 - t_1)$ between the two phase measurements used to formulate the Doppler shift, as shown in Equation 4.8. The effect of this is to reduce the influence of the random phase noise on the estimate of the Doppler shift. Due to limitations on the run-time of the simulations and on the memory storage requirements of MATLAB, the tracking time was only increased by a factor of four.

The tracking performance when the tracking time is increased from 0.3 s to 1.2 s is shown in Figure 4.16. The figure shows the error in the measurement of the Doppler shift for each individual simulation. The simulation parameters are identical to those of the previous simulations, that is, the received signal is a carrier-only signal and the SNR varies between 0–50 dB. Due to the increased run-time of the simulations, which has also increased by a factor of four, only 60 simulations were run for each specific case. The results are summarized in Figures 4.17 and 4.18, which show the mean error and the variance of the error, respectively. The previous results are also shown in the figures for comparison purposes. The mean error now satisfies the navigation performance requirements throughout the range of values of SNR. However, the error still does not have a zero mean and there is a distinct linear increase in the mean error as the SNR increases, which remains unexplained. Finally, the variance of the error has reduced significantly from the previous results.
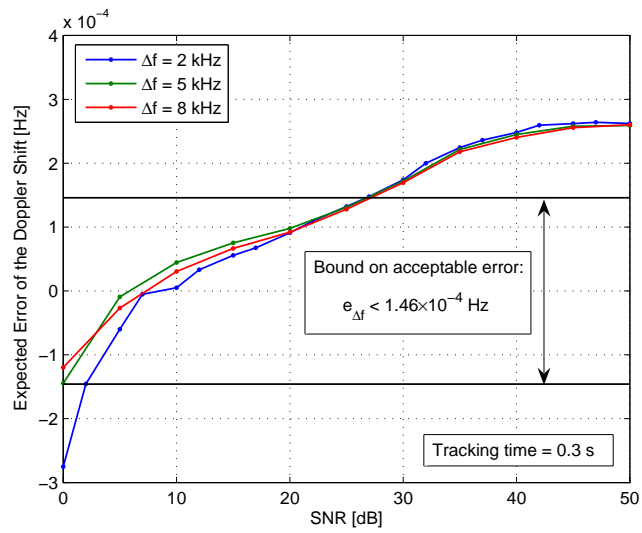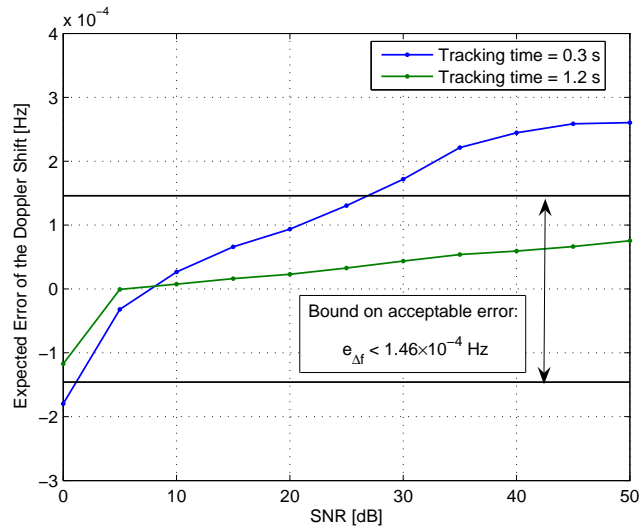
Figure 4.17: Mean error of the Doppler shift for a carrier-only signal for a tracking time of 1.2 s
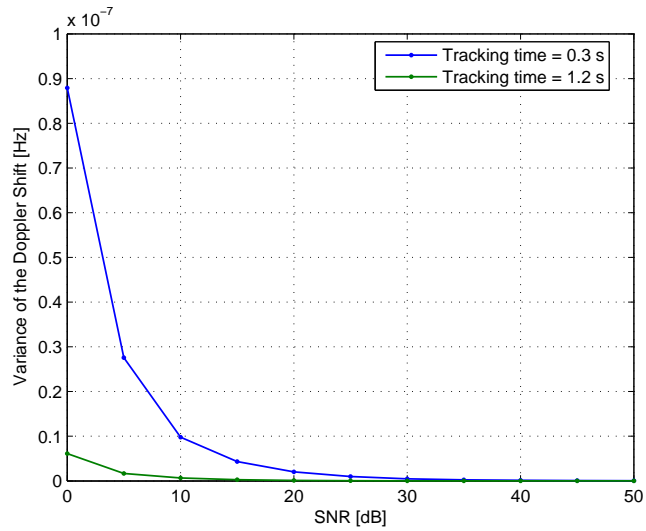
Figure 4.18: Variance of the Doppler shift for a carrier-only signal for a tracking time of 1.2 s

4.4.2 Tracking Performance of Residual and Suppressed Carrier Signals

The tracking performance of the Electra transceiver was also tested for residual carrier and suppressed carrier signals for a range of Doppler shifts and SNRs. The data rate was set between 1 ksps and 8 ksps for both the residual carrier and suppressed carrier signal, which leads to a SNR that varies between -20 dB and $+20$ dB throughout the final approach, as determined by the approach analysis presented in Chapter 2. However, the acquisition performance analysis presented earlier in this chapter revealed that the Electra transceiver could only acquire the transmitted signal reliably when the SNR was greater than 0 dB for a residual carrier signal or greater than 3 dB for a suppressed carrier signal. Thus the tracking performance analysis is limited to the range of values of SNR between 0–20 dB.

The mean error in the measurement of the Doppler shift and the variance of the error are shown in Figures 4.19 and 4.20, respectively, for both the residual carrier and suppressed carrier case. For comparison purposes, the results of the carrier-only case are also shown. Note that these results correspond to a tracking time of approximately 0.3 s. Figure 4.19 shows that for the suppressed carrier signal, the bias in the mean error and the trend of the mean error as a function of the SNR are similar to that of the carrier-only signal. On the other hand, for the residual carrier signal, the mean error fluctuates as a function of the SNR and there doesn't seem to be any similarities with the suppressed carrier signal nor the carrier-only signal.
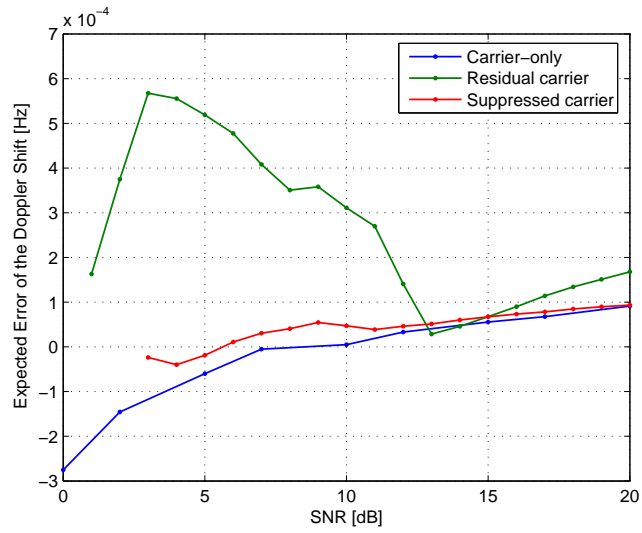
Figure 4.19: Mean error of the Doppler shift for a residual and suppressed carrier signal
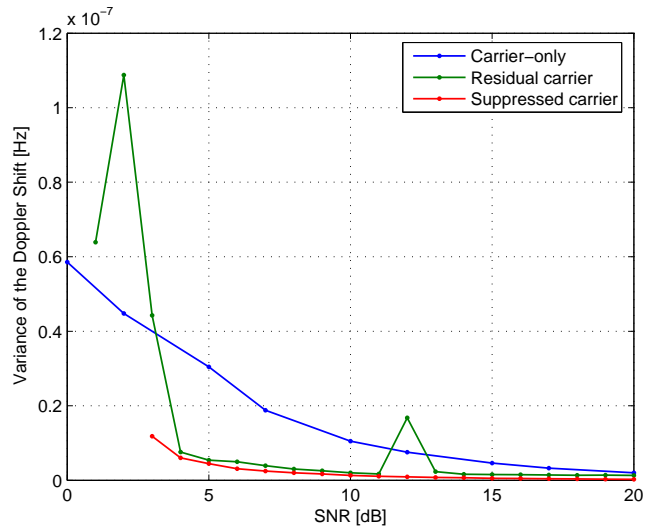
Figure 4.20: Variance of the Doppler shift for a residual and suppressed carrier signal

The variance of the error for the residual carrier and suppressed carrier signal are both lower than the variance for the carrier-only signal and are nearly identical, as shown in Figure 4.20, with the exception of the variance at a SNR of 12 dB. Closer analysis of the simulation data for the residual carrier signal has not revealed any explanation for this anomalous data point, which lies at a variance much higher than anticipated.

The results shown in Figures 4.19 and 4.20 were obtained from simulations with a tracking time of 0.3 s, which corresponds to a simulation run-time of 350 s for the residual carrier case and a simulation run-time of 260 s for the suppressed carrier case. (The difference in run-times is a result of the fact that the bit rate of the Manchester encoded data for the residual carrier signal is twice the bit rate of the NRZ encoded data for the suppressed carrier signal, as described in Appendix A.) It is anticipated that the results will improve in a manner similar to the carrier-only case, as the tracking time is increased. However, these longer simulations were not run as part of the dissertation research work, since it is the carrier-only case that is of most interested to the approach navigation task.

4.5 Electra EDU Testing

The results of the acquisition and tracking performance analysis, presented above, are based on software simulations of the Electra MATLAB model. Although the Electra MATLAB model is a high-fidelity model that provides a direct, bit-to-bit mapping of the functions implemented in the ac-

tual flight FPGA and includes correct levels of quantization for all variables, the performance analysis should be repeated using the Electra EDU in order to verify the results.

The Electra EDU is a breadboard version made from commercial grade (non-space qualified) parts that is functionally equivalent to the Electra flight unit. Two EDUs have been manufactured by JPL for research purposes. One of these units currently resides in the Department of Aerospace Engineering and Engineering Mechanics at The University of Texas at Austin, while the other resides at JPL's Guidance, Navigation, and Control Section. The Electra EDU consists of the BPM, which includes the tracking loop and all of the digital signal processing functions that are described in Chapter 3. It does not include an RF front-end nor a USO. Thus all signal inputs to the Electra EDU must occur at the IF frequency. In this manner, the Electra EDU is identical to the MATLAB model.

The experimental setup required to test the acquisition and tracking performance of the Electra EDU is illustrated in Figure 4.21. It includes the following hardware instruments:

1. A signal generator, such as the Agilent 33250A AWG, which generates the Doppler-shifted carrier signal.

2. A bit-error-rate (BER) analyzer, such as the Acterna FIREBERD 6000, which generates the binary data signal.

117
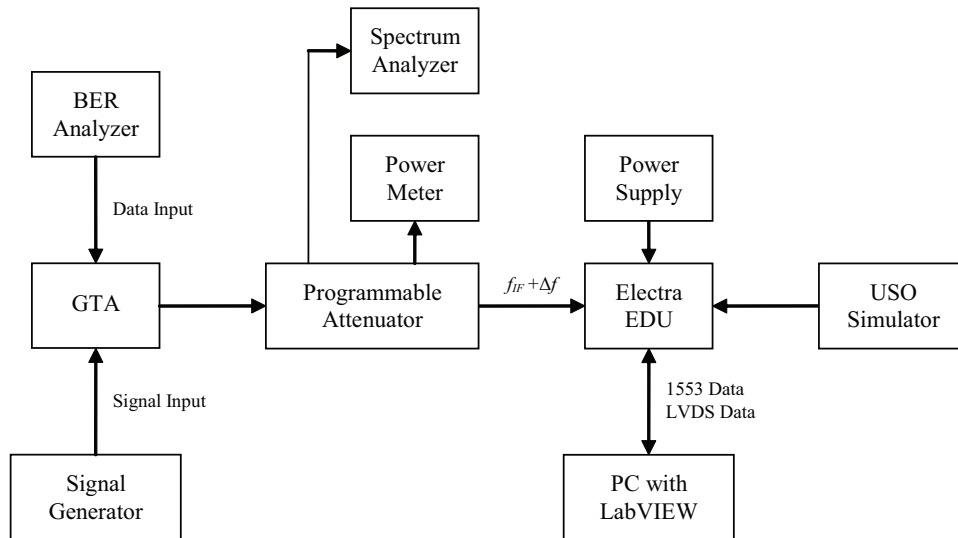
Figure 4.21: Experimental setup for testing the Electra EDU

3. A ground test accelerator (GTA), which modulates the carrier signal with the data signal.

4. A programmable attenuator, such as the Weinschel RF attenuator, which controls the power of the signal sent to the Electra EDU.

5. A spectrum analyzer, such as the Agilent E4445A, and power meter, such as the Agilent 4417A, which verify that the signal entering the Electra EDU has the correct spectrum and power level.

6. An Electra EDU, which contains the digital signal processing functions for acquiring and tracking the test signal.

7. A USO simulator, such as the Fluke 910 GPS, which provides an accurate and stable signal that drives the internal clock of the Electra EDU.

118

8. A PC with LabVIEW, which is used to configure the Electra EDU and to capture the output data using 1553 and LVDS protocols.

A more detailed description of the experimental setup is given by Arnold [5] and [6]. The first reference provides the procedure for testing the tracking performance while the second reference provides the procedure for testing the acquisition performance. Note that performance tests on the Electra EDU were not performed as part of the dissertation research work. Although future work on this research topic should include hardware testing, there is considerable expense involved with acquiring the necessary instruments to support the testing. In addition, there is the issue of providing an accurate and stable simulated USO source to the Electra EDU. Acquisition and tracking performance results will depend strongly on the accuracy and stability of this source. One option is to use the Fluke 910 GPS Controlled Frequency Standard, but this adds complexity and cost to the experimental setup.

Chapter 5

Navigation Filter Design

5.1 Introduction

The design of a navigation filter that is based on the Electra transceiver and that is suitable for Mars final approach navigation is presented in the following sections. The filter design is based on an extended Kalman filter (EKF), which is the standard filter used for these types of applications. The EKF is designed for the Electra transceiver and utilizes the two-way Doppler measurements provided by the Electra transceiver to estimate the position and velocity of the Mars approach vehicle and the Mars Network orbiter. The filter design incorporates a model of the error in the two-way Doppler measurement. The error model is based on the results of the tracking performance analysis presented in Chapter 4, which in turn, is based on simulations of the high-fidelity Electra MATLAB model, presented in Chapter 3, where the simulation parameters were determined from the results of the dynamic analysis and link analysis, presented in Chapter 2.

The resulting EKF design is adaptive in the sense that it includes a model of the error in the Doppler measurement, which is a function of the SNR, as shown in Chapter 4. The SNR is itself a function of the range between the

Mars approach vehicle and the Mars Network orbiter, as shown in Chapter 2. The performance of the resulting navigation filter is analyzed and the information content in the Doppler data and the observability of the estimated states are investigated for various orbital geometries.

5.2   Extended Kalman Filter

The EKF is considered to be the baseline technique for any real-time sequential estimation task with nonlinear dynamics. The theoretical development of the EKF is well known and can be found in several references, including Brown and Hwang [9] and Gelb [24]. The theoretical development will not be presented here; instead a brief overview of the pertinent equations will be presented.

The nonlinear continuous-time model of the system dynamics and the nonlinear discrete-time model of the measurements are given by:

$$\dot{\boldsymbol{X}}(t) = \boldsymbol{F}(\boldsymbol{X}(t), t) + \boldsymbol{W}(t) \tag{5.1}$$

$$\boldsymbol{Y}_i = \boldsymbol{G}(\boldsymbol{X}(t_i), t_i) + \boldsymbol{V}_i \tag{5.2}$$

where

$$
\begin{aligned}
\boldsymbol{X}(t) &= \text{(n$\times$1) state vector} \\
\boldsymbol{F}(\boldsymbol{X}(t), t) &= \text{(n$\times$1) nonlinear function of the state vector } \boldsymbol{X}(t) \\
\boldsymbol{W}(t) &= \text{(n$\times$1) white noise process with known spectral density} \\
\boldsymbol{Y}_i &= \text{(m$\times$1) measurement vector at time } t_i
\end{aligned}
$$

$$\boldsymbol{G}(\boldsymbol{X}(t_i), t_i) \quad = \quad \text{(m}\times\text{n) nonlinear function that relates the states}$$

$$\text{to the measurements}$$

$$\boldsymbol{V}_i \quad = \quad \text{(m}\times\text{1) white noise sequence with known covariance}$$

The white noise process $\boldsymbol{W}(t)$ is assumed to be a zero mean process with a known spectral density $\boldsymbol{Q}(t)$, while the white noise sequence $\boldsymbol{V}_i$ is assumed to be a zero mean sequence with a known covariance $\boldsymbol{R}_i$. Furthermore, it is assumed that $\boldsymbol{W}(t)$ and $\boldsymbol{V}_i$ have zero crosscorrelation. These assumptions are summarized in the following equations:

$$E[\boldsymbol{W}(t)\boldsymbol{W}^T(\tau)] \quad = \quad \boldsymbol{Q}(t)\delta(t-\tau) \tag{5.3}$$

$$E[\boldsymbol{V}_i\boldsymbol{V}_j^T] \quad = \quad \boldsymbol{R}_i\delta_{ij} \tag{5.4}$$

$$E[\boldsymbol{W}_i\boldsymbol{V}_j^T] \quad = \quad 0 \tag{5.5}$$

where $\delta(t-\tau)$ is the Dirac delta function and δ_{ij} is the Kronecker delta function.

Given a nominal or reference state $\boldsymbol{X}^*(t)$ that is related to the actual state by:

$$\boldsymbol{X}(t) = \boldsymbol{X}^*(t) + \boldsymbol{x}(t) \tag{5.6}$$

where $\boldsymbol{x}(t)$ is a small deviation, a first-order Taylor's series expansion can be used to linearize both the system dynamics model and the measurement model about the nominal state, as follows:

$$\dot{\boldsymbol{X}}(t) \quad = \quad \boldsymbol{F}(\boldsymbol{X}^*(t) + \boldsymbol{x}(t), t) + \boldsymbol{W}(t) \tag{5.7}$$

$$= \quad \boldsymbol{F}(\boldsymbol{X}^*(t)) + \frac{\partial \boldsymbol{F}(t)}{\partial \boldsymbol{X}(t)}\bigg|_{\boldsymbol{X}^*} \boldsymbol{x}(t) + \ldots + \boldsymbol{W}(t) \tag{5.8}$$

$$\begin{aligned} \boldsymbol{Y}_i &= \boldsymbol{G}(\boldsymbol{X}^*(t_i) + \boldsymbol{x}(t_i), t_i) + \boldsymbol{V}_i & (5.9) \\ &= \boldsymbol{G}(\boldsymbol{X}^*(t_i)) + \left.\frac{\partial \boldsymbol{G}(t_i)}{\partial \boldsymbol{X}(t_i)}\right|_{\boldsymbol{X}^*} \boldsymbol{x}(t_i) + \ldots + \boldsymbol{V}_i & (5.10) \end{aligned}$$

Since the nominal state $\boldsymbol{X}^*(t)$ satisfies the deterministic differential equation:

$$\dot{\boldsymbol{X}}^*(t) = \boldsymbol{F}(\boldsymbol{X}^*(t), t) \tag{5.11}$$

and since the deviation $\boldsymbol{x}(t)$ is small, the linearized system dynamics and the linearized measurement model can be represented to first-order by:

$$\begin{aligned} \dot{\boldsymbol{x}}(t) &= \boldsymbol{A}(t)\boldsymbol{x}(t) + \boldsymbol{W}(t) & (5.12) \\ \boldsymbol{y}_i &= \boldsymbol{H}_i \boldsymbol{x}(t_i) + \boldsymbol{V}_i & (5.13) \end{aligned}$$

where $\boldsymbol{y}_i$ is defined as:

$$\boldsymbol{y}_i = \boldsymbol{Y}_i - \boldsymbol{G}(\boldsymbol{X}^*(t_i)) \tag{5.14}$$

and where $\boldsymbol{A}(t)$ and $\boldsymbol{H}_i$ are the Jacobian matrices evaluated on the nominal state:

$$\boldsymbol{A}(t) = \left.\frac{\partial \boldsymbol{F}(t)}{\partial \boldsymbol{X}(t)}\right|_{\boldsymbol{X}^*} \qquad \boldsymbol{H}_i = \left.\frac{\partial \boldsymbol{G}(t_i)}{\partial \boldsymbol{X}(t_i)}\right|_{\boldsymbol{X}^*} \tag{5.15}$$

The EKF estimates the current state $\boldsymbol{X}(t)$ recursively and linearly using discrete measurements $\boldsymbol{Y}_i$. Given a new measurement $\boldsymbol{Y}_i$, the optimal update of the state estimate $\hat{\boldsymbol{X}}_i$ at time t_i can be shown to be given by the linear, recursive equation:

$$\hat{\boldsymbol{X}}_i = \hat{\boldsymbol{X}}_i^- + \boldsymbol{K}_i[\boldsymbol{Y}_i - \boldsymbol{H}_i \hat{\boldsymbol{X}}_i^-] \tag{5.16}$$

where $\boldsymbol{K}_i$ is the Kalman gain and $\hat{\boldsymbol{X}}_i^-$ is an a priori estimate of the state. The optimal Kalman gain for calculating the state estimate $\hat{\boldsymbol{X}}_i$ can be shown to

123

be given by:

$$K_i = P_i^- H_i^T [H_i P_i^- H_i^T + R_i]^{-1} \tag{5.17}$$

where P_i^- is the error covariance associated with the a priori state estimate. The error covariance for the updated state estimate in the Joseph formulation can be shown to be:

$$\begin{aligned}
P_i &= E[(X_i - \hat{X}_i)(X_i - \hat{X}_i)^T] \tag{5.18} \\
&= [I - K_i H_i] P_i^- [I - K_i H_i]^T + K_i R_i K_i^T \tag{5.19}
\end{aligned}$$

The updated state estimate and error covariance are then propagated forward in time to the next measurement point at time t_{i+1}. The state estimate $\hat{X}_{i+1}^-$ at time t_{i+1} is the solution to the deterministic differential equation:

$$\dot{\hat{X}}(t) = F(\hat{X}(t), t) \tag{5.20}$$

with initial condition $\hat{X}_i$ at time t_i. The error covariance at time t_{i+1} is given by:

$$P_{i+1}^- = \Phi_i P_i \Phi_i^T + Q_i \tag{5.21}$$

where Φ_i is the state transition matrix that is the solution to the differential equation:

$$\dot{\Phi}(t, t_i) = A(t)\Phi(t, t_i) \tag{5.22}$$

with initial condition $\Phi(t_i, t_i) = I$.

The process is then repeated by returning to Equation 5.16 and calculating the new optimal gain K_{i+1} using $\hat{X}_{i+1}^-$ as the a priori state estimate and P_{i+1}^- as its corresponding error covariance.

5.3 Dynamic Model

The nonlinear dynamic model consists of the Mars gravitational poten-
tial and the atmospheric drag perturbation. Thus, the spacecraft equation of
motion is given by:

$$\ddot{\boldsymbol{r}} = \nabla U + \boldsymbol{a}_{Drag} \tag{5.23}$$

where $\ddot{\boldsymbol{r}}$ is the spacecraft inertial acceleration vector, U is the Mars gravita-
tional potential, and $\boldsymbol{a}_{Drag}$ is the atmospheric drag perturbation.

If the state vector $\boldsymbol{X}(t)$ is a six element vector, consisting of the space-
craft inertial position and velocity components, then the nonlinear dynamic
model can be represented by:

$$\boldsymbol{X}(t) = \begin{bmatrix} \boldsymbol{r} \\ \dot{\boldsymbol{r}} \end{bmatrix}_{(6\times1)} \qquad \boldsymbol{F}(\boldsymbol{X}(t)) = \begin{bmatrix} \dot{\boldsymbol{r}} \\ \nabla U + \boldsymbol{a}_{Drag} \end{bmatrix}_{(6\times1)} \tag{5.24}$$

The Jacobian matrix $\boldsymbol{A}(t)$ and the partial derivatives of the dynamic
model with respect to the state vector are given in Appendix C.

5.3.1 Gravitational Potential

The gravitational potential consists of the two-body gravitational term
and the J_2 perturbation, which accounts for the oblateness of Mars. Thus, the
gravitational potential can be modeled as:

$$U = \frac{\mu}{r} + \mu R_m^2 J_2 \left(\frac{1}{2r^3} - \frac{3z^2}{2r^5} \right) \tag{5.25}$$

where

125

$$\mu \quad = \quad \text{Mars gravitational parameter, } 4.283 \times 10^{13} \text{ m}^3\text{s}^{-2}$$

$$R_m \quad = \quad \text{Mean equatorial radius of Mars, } 3402.5 \text{ km}$$

$$J_2 \quad = \quad \text{Second zonal harmonic coefficient of Mars, } 0.00196045$$

and where r is the radial distance of the spacecraft from the center of Mars, which in the inertial coordinates (x, y, z) is given by:

$$r = \sqrt{x^2 + y^2 + z^2} \tag{5.26}$$

The acceleration due to the gravitational potential is found by taking the gradient of the gravitational potential ∇U, which yields the following components in the three inertial directions:

$$a_{U_x} = -\frac{\mu}{r^3}x\left\{1 - \frac{3}{2}\left(\frac{R_m}{r}\right)^2 J_2\left[5\left(\frac{z}{r}\right)^2 - 1\right]\right\} \tag{5.27}$$

$$a_{U_y} = -\frac{\mu}{r^3}y\left\{1 - \frac{3}{2}\left(\frac{R_m}{r}\right)^2 J_2\left[5\left(\frac{z}{r}\right)^2 - 1\right]\right\} \tag{5.28}$$

$$a_{U_z} = -\frac{\mu}{r^3}z\left\{1 - \frac{3}{2}\left(\frac{R_m}{r}\right)^2 J_2\left[5\left(\frac{z}{r}\right)^2 - 3\right]\right\} \tag{5.29}$$

5.3.2 Atmospheric Drag Perturbation

The acceleration due to atmospheric drag is given by:

$$\boldsymbol{a}_{Drag} = -\frac{1}{2}\frac{C_D A}{M}\rho\left|\boldsymbol{v}_{rel}\right|\boldsymbol{v}_{rel} \tag{5.30}$$

where

$$C_D \quad = \quad \text{Coefficient of drag}$$

$$A \quad = \quad \text{Spacecraft cross-sectional area}$$

126

$$M = \text{Spacecraft mass}$$

The assumed values for the spacecraft drag parameters for the MAV [15] and the MNO [36] are summarized in Table 5.1.

The spacecraft velocity vector relative to the rotating atmosphere is modeled as:

$$\boldsymbol{v}_{rel} = \dot{\boldsymbol{r}} - \boldsymbol{\omega}_m \times \boldsymbol{r} \tag{5.31}$$

where $\boldsymbol{r}$ and $\dot{\boldsymbol{r}}$ are the spacecraft inertial position and velocity vectors, respectively, and $\boldsymbol{\omega}_m$ is the Mars angular velocity vector, which is assumed to be aligned with the inertial z-axis. The magnitude of the angular velocity vector is assumed to be:

$$\omega_m = \frac{2\pi}{88642.663} = 7.0882 \times 10^{-5} \text{ rad/s} \tag{5.32}$$

The atmospheric density ρ is modeled using an exponential model, which is given by:

$$\rho = \rho_0 \, e^{-\gamma \, (r - r_0)} \tag{5.33}$$

where ρ is the density in kg-m^3 and where the constant model parameters are given by [25]:

$$\rho_0 = \text{Reference density, } 4.7 \times 10^{-4} \text{ kg-m}^3$$
$$\gamma = \text{Scale factor, } 1 \times 10^{-4}$$
$$r_0 = \text{Reference distance, } 3.429 \times 10^6 \text{ m}$$

Table 5.1: Drag parameter values

Parameter	MAV	MNO
C_D	2.2	2.2
A (m^2)	12.5	36.0
M (kg)	3400	1225

5.4 Measurement Model

The Electra navigation measurement is the two-way integrated Doppler observable, as previously described. A simplified model of the Doppler observable is given by:

$$\Delta f = -\frac{f_T \dot{r}}{c} \tag{5.34}$$

where f_T is the transmitted signal frequency, $\dot{r}$ is the range rate between the MAV and the MNO, and c is the speed of light. Since the range rate is given by:

$$\dot{r} = \frac{(\dot{\boldsymbol{r}}_{MAV} - \dot{\boldsymbol{r}}_{MNO})^T (\boldsymbol{r}_{MAV} - \boldsymbol{r}_{MNO})}{\left| \boldsymbol{r}_{MAV} - \boldsymbol{r}_{MNO} \right|} \tag{5.35}$$

the Doppler measurement model can be represented as:

$$\boldsymbol{G}(\boldsymbol{X}(t_i), t_i) = -\frac{f_T}{c} \frac{(\dot{\boldsymbol{r}}_{MAV} - \dot{\boldsymbol{r}}_{MNO})^T (\boldsymbol{r}_{MAV} - \boldsymbol{r}_{MNO})}{\left| \boldsymbol{r}_{MAV} - \boldsymbol{r}_{MNO} \right|} \tag{5.36}$$

If the state vector is a twelve element vector, consisting of the inertial position and velocity components of both the MAV and the MNO, it can be

represented by:

$$\boldsymbol{X}(t) = \begin{bmatrix} \boldsymbol{r}_{MAV} \\ \dot{\boldsymbol{r}}_{MAV} \\ \boldsymbol{r}_{MNO} \\ \dot{\boldsymbol{r}}_{MNO} \end{bmatrix}_{(12 \times 1)} \tag{5.37}$$

Then the Jacobian matrix $\boldsymbol{H}_i$ and the partial derivatives of the Doppler measurement model with respect to the state vector are given by:

$$\boldsymbol{H}_i = \left. \frac{\partial \boldsymbol{G}(t_i)}{\partial \boldsymbol{X}(t_i)} \right|_{\boldsymbol{X}^*} = \begin{bmatrix} \boldsymbol{H}_{i,1} & \boldsymbol{H}_{i,2} & \boldsymbol{H}_{i,3} & \boldsymbol{H}_{i,4} \end{bmatrix}_{(1 \times 12)} \tag{5.38}$$

where

$$\boldsymbol{H}_{i,1_{(1 \times 3)}} = \left. \frac{\partial \boldsymbol{G}(t_i)}{\partial \boldsymbol{r}_{MAV}} \right|_{\boldsymbol{X}^*} = -\frac{f_T}{c} \left[\frac{\dot{\boldsymbol{r}}_{rel}^T}{|\boldsymbol{r}_{rel}|} - \frac{\dot{\boldsymbol{r}}_{rel}^T \boldsymbol{r}_{rel} \boldsymbol{r}_{rel}^T}{|\boldsymbol{r}_{rel}|^3} \right] \tag{5.39}$$

$$\boldsymbol{H}_{i,2_{(1 \times 3)}} = \left. \frac{\partial \boldsymbol{G}(t_i)}{\partial \dot{\boldsymbol{r}}_{MAV}} \right|_{\boldsymbol{X}^*} = -\frac{f_T}{c} \frac{\boldsymbol{r}_{rel}^T}{|\boldsymbol{r}_{rel}|} \tag{5.40}$$

$$\boldsymbol{H}_{i,3_{(1 \times 3)}} = \left. \frac{\partial \boldsymbol{G}(t_i)}{\partial \boldsymbol{r}_{MNO}} \right|_{\boldsymbol{X}^*} = +\frac{f_T}{c} \left[\frac{\dot{\boldsymbol{r}}_{rel}^T}{|\boldsymbol{r}_{rel}|} - \frac{\dot{\boldsymbol{r}}_{rel}^T \boldsymbol{r}_{rel} \boldsymbol{r}_{rel}^T}{|\boldsymbol{r}_{rel}|^3} \right] \tag{5.41}$$

$$\boldsymbol{H}_{i,4_{(1 \times 3)}} = \left. \frac{\partial \boldsymbol{G}(t_i)}{\partial \dot{\boldsymbol{r}}_{MNO}} \right|_{\boldsymbol{X}^*} = +\frac{f_T}{c} \frac{\boldsymbol{r}_{rel}^T}{|\boldsymbol{r}_{rel}|} \tag{5.42}$$

and where the following definitions have been made:

$$\boldsymbol{r}_{rel} = \boldsymbol{r}_{MAV} - \boldsymbol{r}_{MNO} \tag{5.43}$$

$$\dot{\boldsymbol{r}}_{rel} = \dot{\boldsymbol{r}}_{MAV} - \dot{\boldsymbol{r}}_{MNO} \tag{5.44}$$

5.4.1 Measurement Error Model

The results of the tracking performance analysis of the Electra transceiver were presented in Section 4.4. The results revealed the characteristics of the

steady-state tracking error in the two-way Doppler measurement. It was found that the mean error and the variance of the error were strongly dependent on the SNR but independent of the Doppler shift up to 10 kHz. The Electra transceiver is capable of estimating the SNR, based on measurements of the in-phase signal $I[n]$ and the quadrature-phase signal $Q[n]$ of the tracking loop, as described in Section 3.6. Consequently, a model of the error in the two-way Doppler measurement as a function of the SNR can be included in the navigation filter, such that the filter is capable of estimating the mean error and the variance of the error, based on measurements of the SNR by the Electra transceiver. In this way, the navigation filter is adaptive to the dynamic operating environment of the Electra transceiver throughout the final approach phase.

The results of the acquisition performance analysis of the Electra transceiver were presented in Section 4.3. The results revealed that the tracking loop could reliably acquire a carrier-only signal with a SNR of -4 dB and higher. Similarly, the tracking loop could reliably acquire a residual carrier signal and a suppressed carrier signal when the SNR was greater than 0 dB and $+3$ dB, respectively. In addition, the results of the link analysis presented in Section 2.4 revealed that the SNR of a carrier-only signal is $+20$ dB at 10 hours prior to atmospheric entry, which is the point at which the link can be closed, and increases up to $+50$ dB at the point of atmospheric entry. Similarly, the SNR of a residual carrier signal and a suppressed carrier signal with a data rate of 1 ksps is approximately -10 dB at 10 hours prior to atmospheric entry,

and increases up to +20 dB at the point of atmospheric entry. Furthermore, the link analysis revealed that the SNR of a residual carrier signal and a suppressed carrier signal with a data rate of 1 ksps does not increase above 0 dB until approximately 2 hours prior to atmospheric entry. Consequently, from 10 hours prior to atmospheric entry and up to 2 hours prior to atmospheric entry, the Electra transceiver can only acquire the carrier-only signal. Thus, it is the carrier-only signal that is of primary interest to the design of the navigation filter and consequently, it is the tracking performance analysis of the carrier-only signal that forms the basis of the model of the error in the Doppler measurement.

The mean error in the measurement of the Doppler shift for a carrier-only signal can be modeled by a linear relationship, as shown in Figure 5.1, where the corresponding residuals are shown in Figure 5.2. The data point at a SNR of 0 dB has been omitted from the linear model since it falls well outside of the range of expected values of SNR from +20 dB to +50 dB throughout the final approach. The coefficients corresponding to the linear model are given in Table 5.2.

The variance of the error in the measurement of the Doppler shift can be modeled in a similar manner, as shown in Figure 5.3, where a fifth-degree polynomial is used to approximate the variance. Again, the data point at a SNR of 0 dB has been omitted from the model. The residuals associated with the fifth-degree polynomial approximation are shown in Figure 5.4, while the coefficients of the fifth-degree polynomial are given in Table 5.2.
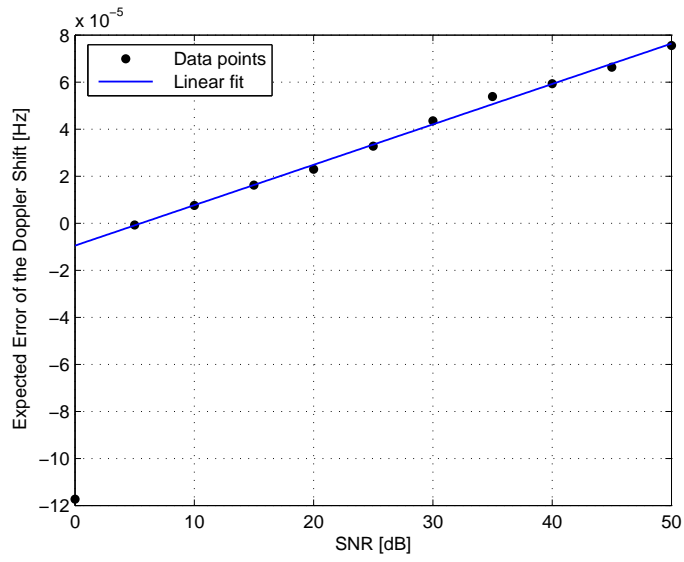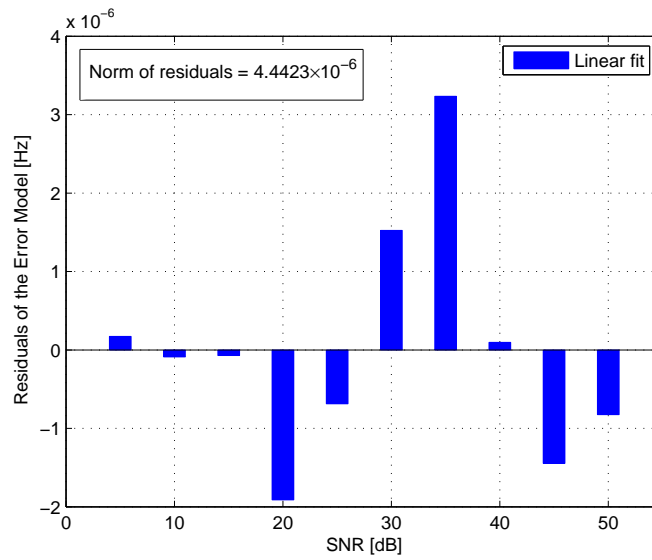
131

Figure 5.1: Linear model of the mean error

Figure 5.2: Residuals for the linear model of the mean error

132
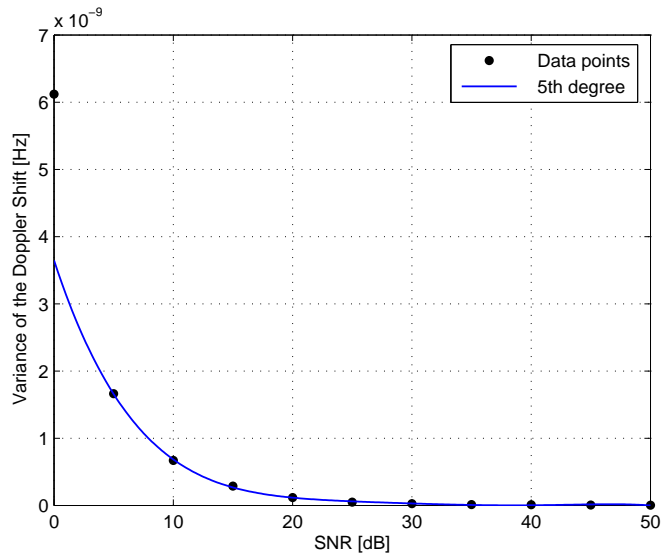
Figure 5.3: Polynomial approximation of the variance of the error
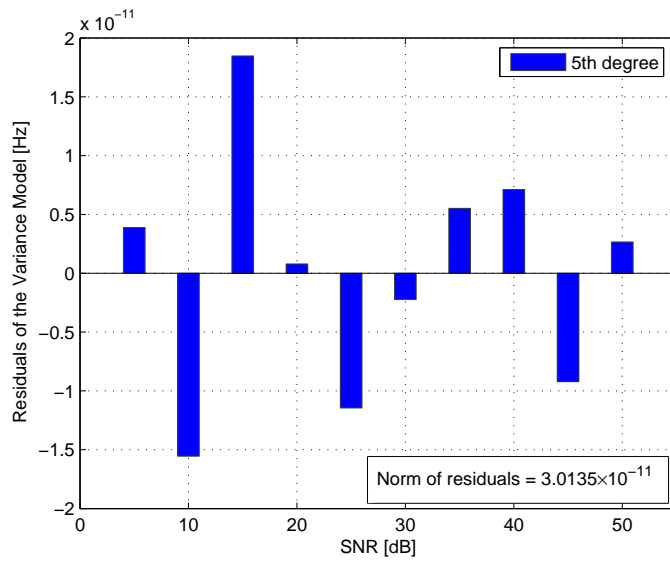
Figure 5.4: Residuals for the polynomial approximations of the variance of the error

133

Table 5.2: Coefficients of the polynomials for the error and variance models

Model	x^5	x^4	x^3	x^2	x^1	x^0
Error ($\times 10^{-6}$ Hz)	-	-	-	-	1.718	-9.514
Variance ($\times 10^{-11}$ Hz)	-7.296	1.450	-4.907	3.520	-9.343	4.399

5.5 Navigation Filter Performance

The performance of the navigation filter is analyzed and the information content in the Doppler measurement is investigated for different Mars Network orbiters and for different orbital geometries. For each analysis, the measurement processing begins at 10 hours prior to atmospheric entry, which is the point at which the communications link can initially be closed, and continues up to the point of atmospheric entry. The effect of occultations on the navigation filter performance is considered by comparing the filter performance for the cases when occultations are included in the analysis with the cases when occultations are ignored.

In order to investigate the information content in the raw Electra navigation measurement, only the Electra Doppler measurement is considered in the analysis, in spite of the availability of DSN tracking data during part of the final approach from 10 hours prior to atmospheric entry and up to the data cutoff point at approximately 6 hours prior to atmospheric entry. In an actual operational environment, the DSN data and the Electra Doppler data would

be fused together in some manner to yield a combined navigation solution. In the interest of examining the raw Electra measurement and due to the lack of an accurate DNS tracking model and data fusion method, the availability of the DSN tracking data is ignored in the analysis. Consequently, the accuracy of the navigation solution is not indicative of the likely accuracy that can be achieved in an operational environment, which can be assumed to be superior due to the additional data from the DSN tracking.

Two different values for the a priori uncertainties in the inertial position and velocity of the Mars approach vehicle are considered. In the first case, the a priori uncertainty is assumed to be 1000 km in the position coordinates and 1 km/s in the velocity components, which corresponds to the a priori uncertainty at the start of the initial approach phase at 30–45 days before atmospheric entry [20]. This is the a priori uncertainty that is typically used at the start of DSN tracking. At the end of the initial approach phase, the DSN tracking has reduced the uncertainties to approximately 10 km in the position coordinates and 0.1 km/s in the velocity components [20]. These values are used as the a priori uncertainties for the second case that is considered in the analysis.

It is necessary to consider the geometry of the approach trajectory of the MAV, in order to analyze the information content in the Electra Doppler measurement and to understand the results of the navigation performance analysis. The geometry of the approach is illustrated in Figure 5.5, which shows the approach trajectory along the three inertial axes. The figure shows
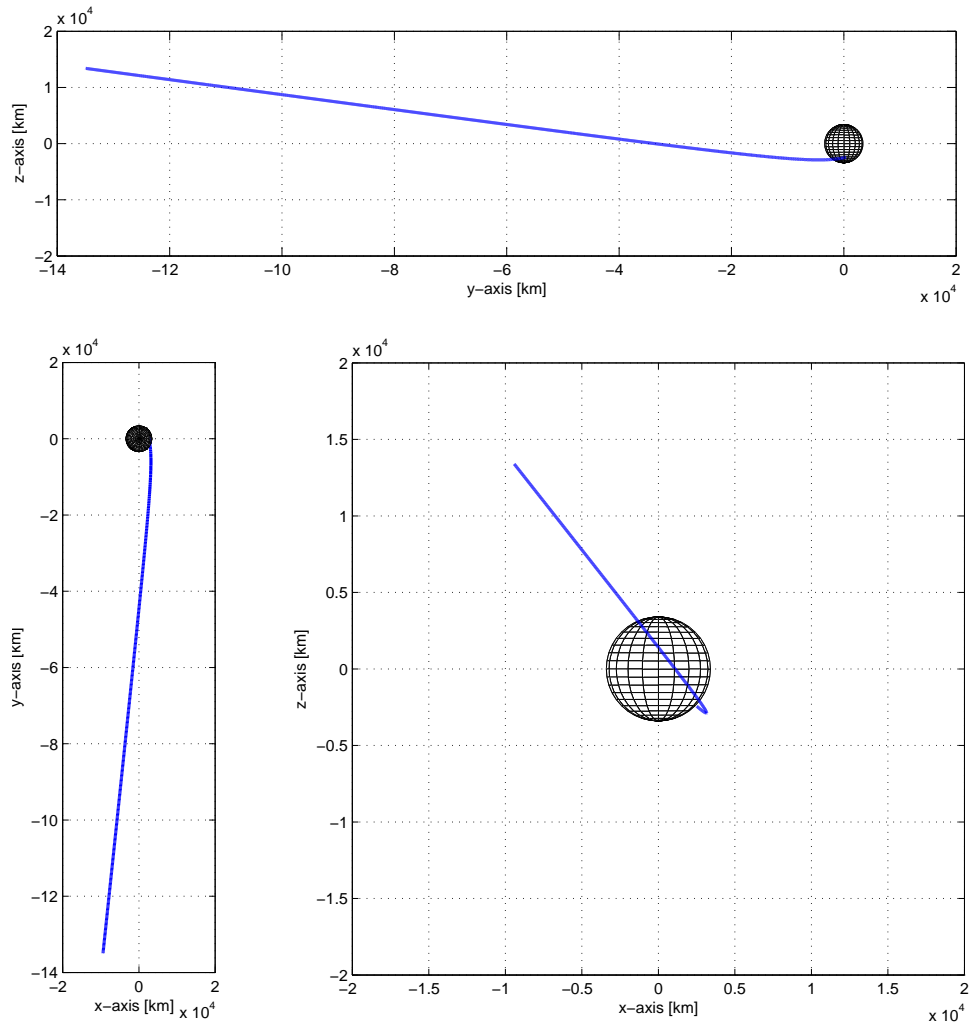
Figure 5.5: Approach geometry for the MAV

that the approach trajectory is aligned primarily along the y-axis, with only small movements in the x-axis and z-axis. This will affect the overall performance of the navigation solution and lead to a markedly different performance along the three inertial coordinate axes, as shown in the following sections.

5.5.1 Determination of the Covariances

There are three covariance matrices associated with the EKF, namely the measurement error covariance $\boldsymbol{R}_i$, the process noise covariance $\boldsymbol{Q}_i$, and the state estimate error covariance $\boldsymbol{P}_i$. Typically, the measurement error covariance and the process noise covariance are parameters that are used to tune the filter performance. In this case, the measurement error covariance is determined from the steady-state tracking performance analysis, presented in Section 4.4, and a model of the measurement error covariance as a function of the SNR and hence, the range between the MAV and the MNO, is included in the filter design.

The process noise covariance is difficult to determine, and typically the value of the process noise is varied in a trial-and-error method in order to tune the performance of the navigation filter. For a six element state vector, the process noise covariance is a (6×6) matrix, which would require at least the six diagonal elements and possibly as much as all 36 elements to be tuned individually. However, there is a simpler method of determining the process noise covariance, which uses the relationship between the spectral density matrix $\boldsymbol{Q}(t)$, associated with the continuous-time system dynamics, and the process

noise covariance $\boldsymbol{Q}_i$, used in the discrete-time update equations of the EKF. The process noise covariance is the solution to the differential equation:

$$\dot{\boldsymbol{Q}}_i = \boldsymbol{A}(t)\boldsymbol{Q}_i + \boldsymbol{Q}_i\boldsymbol{A}^T(t) + \boldsymbol{Q}(t) \tag{5.45}$$

with initial condition $\boldsymbol{Q}_i = \boldsymbol{0}_{(6\times6)}$ and where $\boldsymbol{A}(t)$ is the Jacobian matrix. The spectral density matrix can then be modeled as:

$$\boldsymbol{Q}(t) = \left[\begin{array}{cc} \boldsymbol{0}_{(3\times3)} & \boldsymbol{0}_{(3\times3)} \\ \boldsymbol{0}_{(3\times3)} & \alpha\boldsymbol{I}_{(3\times3)} \end{array} \right] \tag{5.46}$$

where α is a scalar and $\boldsymbol{I}$ is the identity matrix. Now the only tuning parameter associated with the determination of the process noise covariance is the scalar α, and the natural dynamics associated with the system, as represented by the Jacobian matrix $\boldsymbol{A}(t)$, are used to populate the elements of the (6×6) process noise covariance matrix.

The final covariance matrix associated with the EKF is the state estimate error covariance $\boldsymbol{P}_i$. The error covariance matrix is calculated at each time step before and after the measurement update and it is a measure of the accuracy of the navigation solution. It is instructive to consider the evolution of the error covariance as a function of time, without including any measurements. This shows the natural growth of the error covariance as a result of the natural system dynamics. The error covariance for the inertial position and velocity components of the MAV is shown in Figures 5.6 and 5.7, respectively. The figures show the growth in the error covariance for the two cases when the a priori uncertainty is 1000 km in position and 1 km/s in velocity and 10 km in position and 0.1 km/s in velocity.
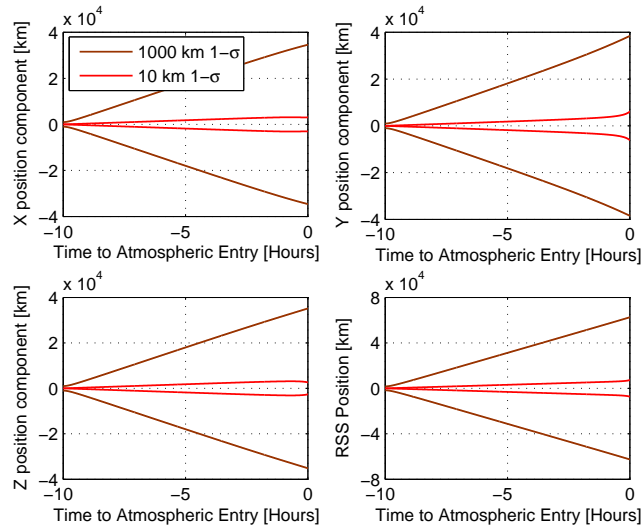
138

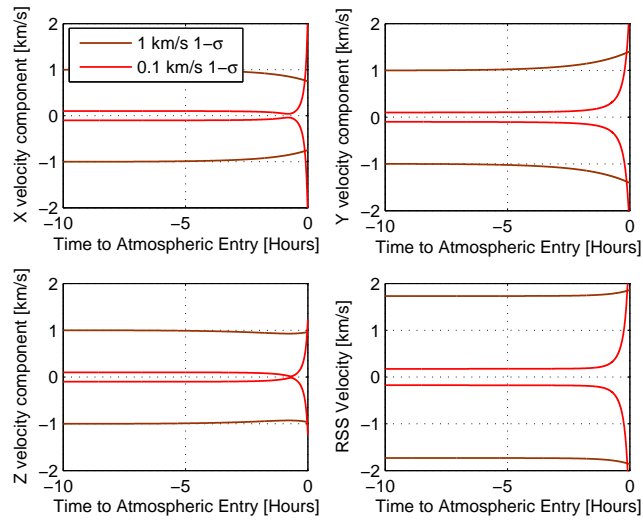Figure 5.6: Error covariance growth in position without measurements

Figure 5.7: Error covariance growth in velocity without measurements

139

5.5.2 Navigation Performance with MRO

The navigation performance when the Mars Network orbiter is MRO is shown in Figures 5.8–5.19. All of the results are given in terms of the inertial position and velocity components of the MAV. The results shown in Figures 5.8–5.13 correspond to the case when the a priori uncertainty is 1000 km in each of the position components and 1 km/s in each of the velocity components, while the results shown in Figures 5.14–5.19 correspond to the case when the a priori uncertainty is 10 km in each of the position components and 0.1 km/s in each of the velocity components. For each case, three different orbital geometries for MRO are considered, which correspond to a right ascension of the ascending node (RAAN) of 180 deg, 225 deg, and 270 deg. This yields a difference in the RAAN between the MAV orbit and the MNO orbit of approximately 90 deg, 45 deg, and 0 deg, respectively.

The results shown in Figures 5.8–5.13 show that, in general, there is little information content in the Electra Doppler data in the y-axis position component of the MAV. The y-axis corresponds to the direction of the asymptote of the hyperbolic approach trajectory and can be considered to be the along-track direction. The covariance of the y-axis position component is constant for most of the final approach and doesn't significantly reduce until the final few hours of the approach when the relative orbital geometry changes. In comparison, the information content in the x-axis and z-axis position components of the MAV is, in general, significantly higher. The result is that the covariance of the x-axis and z-axis position components are rapidly reduced

when the relative orbital geometry is favorable. A favorable orbital geometry is one in which there is a substantial difference in RAAN between the MAV orbit and the MNO orbit. When the difference in RAAN approaches zero, the information content in the x-axis position component of the MAV is significantly reduced. The consequence is that initially the covariance of the x-axis position component grows rapidly and overwhelms any contribution from the measurement data to the reduction of the covariance.

The results shown in Figures 5.14–5.19 confirm the previous results, namely that there is little information content in the Electra Doppler data in the y-axis position component of the MAV. Furthermore, the results confirm that the orbital geometry is highly unfavorable when the difference in RAAN between the MAV orbit and the MNO orbit approaches zero. In addition, the figures show that the Electra Doppler data does not contain sufficient information to reduce the covariance of the position components, when the initial uncertainty in the position components is 10 km. As a result, the covariance initially grows before the measurements are able to reduce it to a level that corresponds to the initial uncertainty.

The effect of occultation is also included in the analysis. The results when occultation is included is shown by the dotted line in the figures. The results show that the effect of occultation on the navigation performance is negligible. The covariance grows during the occultation periods, but when line-of-sight visibility returns, the covariance is rapidly reduced to a level that corresponds with the results of the analysis when occultation is not included.

141

Figure 5.8: Position errors with MRO when the difference in RAAN is 90 deg and the a priori uncertainty is large (solid line: no occultations, dotted line: with occultations)

Figure 5.9: Velocity errors with MRO when the difference in RAAN is 90 deg and the a priori uncertainty is large (solid line: no occultations, dotted line: with occultations)

Figure 5.10: Position errors with MRO when the difference in RAAN is 45 deg and the a priori uncertainty is large (solid line: no occultations, dotted line: with occultations)
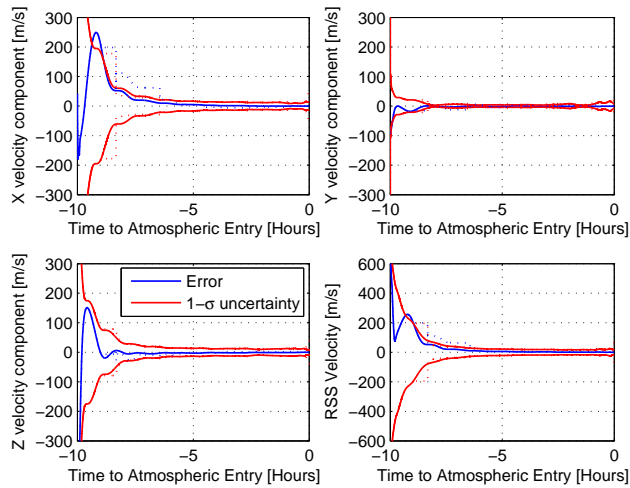
Figure 5.11: Velocity errors with MRO when the difference in RAAN is 45 deg and the a priori uncertainty is large (solid line: no occultations, dotted line: with occultations)

143
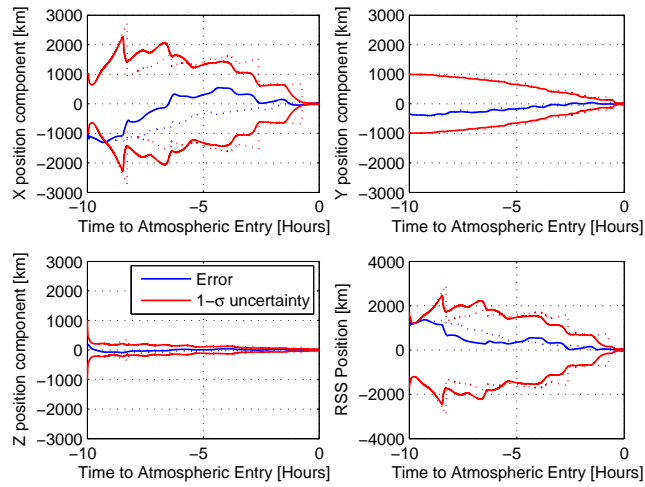
Figure 5.12: Position errors with MRO when the difference in RAAN is 0 deg and the a priori uncertainty is large (solid line: no occultations, dotted line: with occultations)
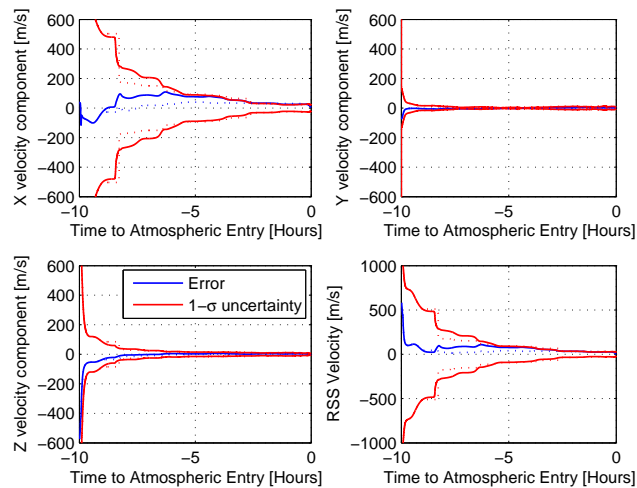
Figure 5.13: Velocity errors with MRO when the difference in RAAN is 0 deg and the a priori uncertainty is large (solid line: no occultations, dotted line: with occultations)
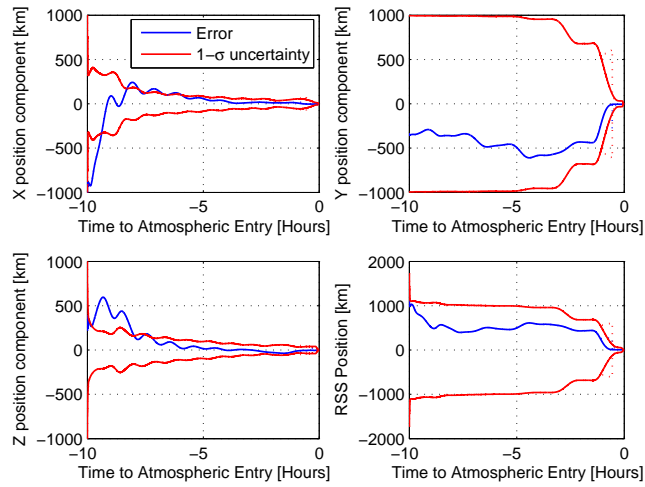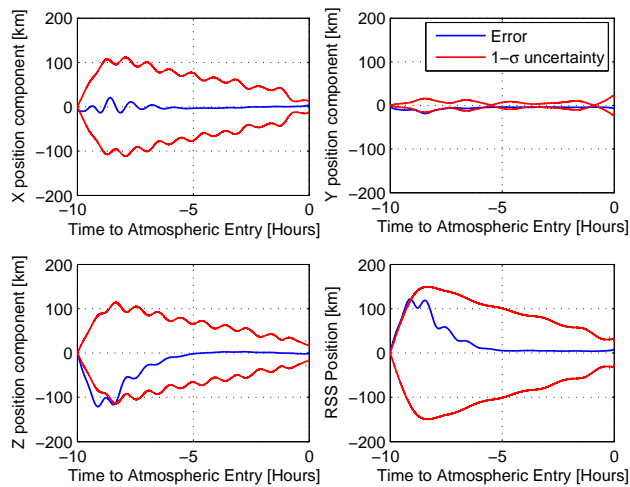
Figure 5.14: Position errors with MRO when the difference in RAAN is 90 deg and the a priori uncertainty is small (solid line: no occultations, dotted line: with occultations)
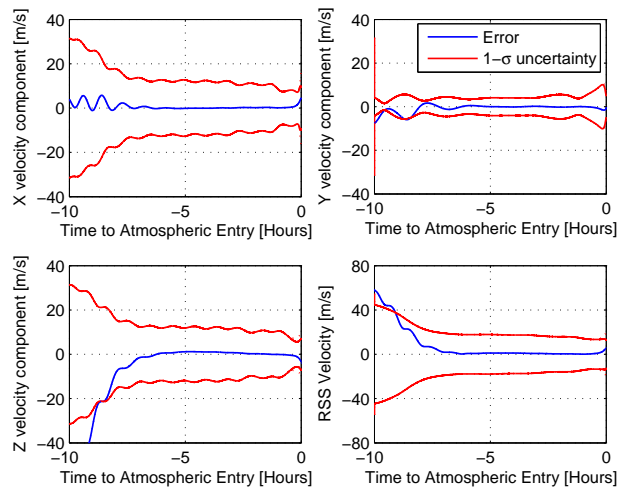
Figure 5.15: Velocity errors with MRO when the difference in RAAN is 90 deg and the a priori uncertainty is small (solid line: no occultations, dotted line: with occultations)
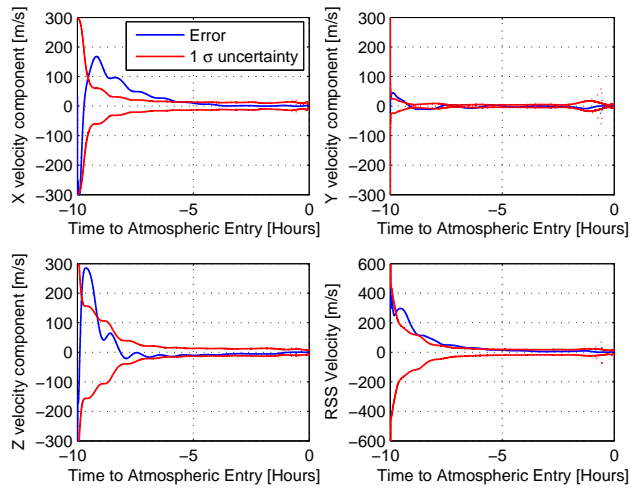
145
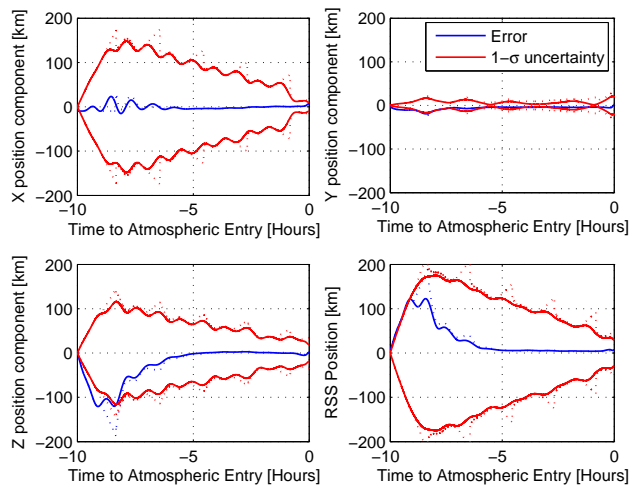
Figure 5.16: Position errors with MRO when the difference in RAAN is 45 deg and the a priori uncertainty is small (solid line: no occultations, dotted line: with occultations)
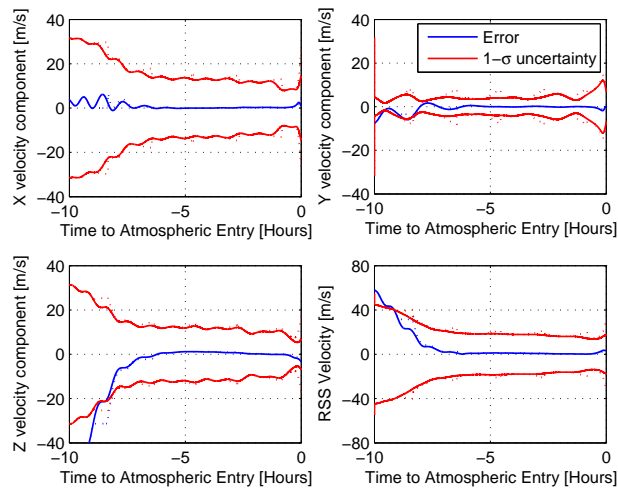
Figure 5.17: Velocity errors with MRO when the difference in RAAN is 45 deg and the a priori uncertainty is small (solid line: no occultations, dotted line: with occultations)
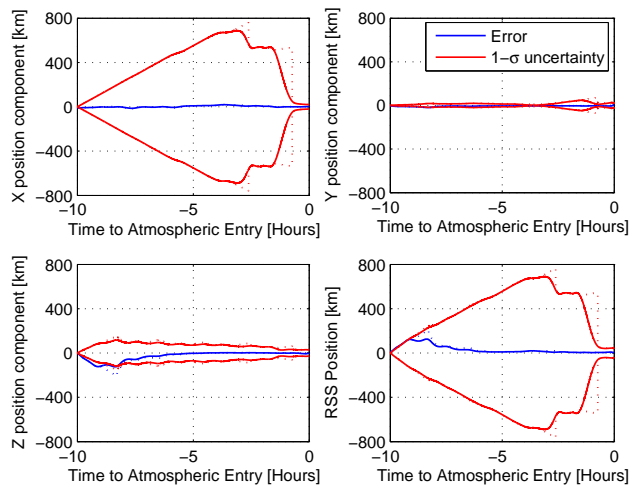
Figure 5.18: Position errors with MRO when the difference in RAAN is 0 deg and the a priori uncertainty is small (solid line: no occultations, dotted line: with occultations)
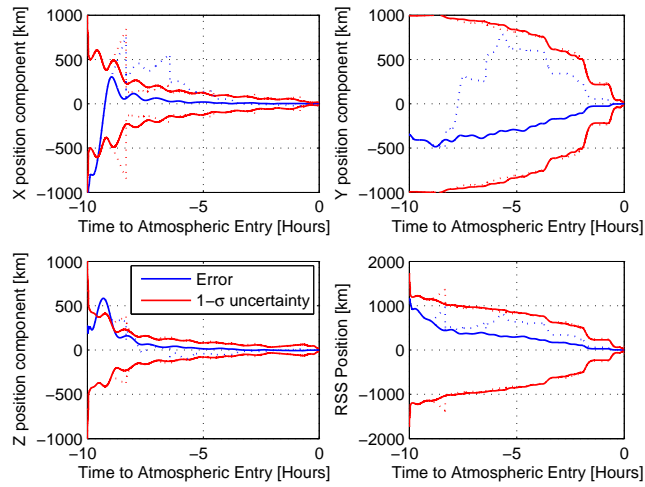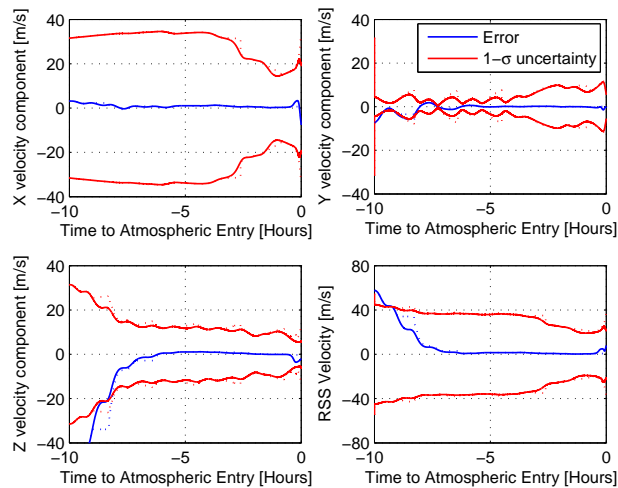

Figure 5.19: Velocity errors with MRO when the difference in RAAN is 0 deg and the a priori uncertainty is small (solid line: no occultations, dotted line: with occultations)

### 5.5.3 Navigation Performance with MTO

The navigation performance when the Mars Network orbiter is MTO is shown in Figures 5.20–5.31. All of the results are given in terms of the inertial position and velocity components of the MAV. The results shown in Figures 5.20–5.25 correspond to the case when the a priori uncertainty is 1000 km in each of the position components and 1 km/s in each of the velocity components, while the results shown in Figures 5.26–5.31 correspond to the case when the a priori uncertainty is 10 km in each of the position components and 0.1 km/s in each of the velocity components. For each case, three different orbital geometries for MTO are considered, which correspond to a RAAN of 180 deg, 225 deg, and 270 deg. This yields a difference in the RAAN between the MAV orbit and the MNO orbit of approximately 90 deg, 45 deg, and 0 deg, respectively. Note that the effect of occultation is not included in the analysis since the high-altitude MTO orbit is continuously visible throughout the final approach.

The results show that when the Mars Network orbiter is MTO the information content in the Electra Doppler data is less than when it is MRO. This confirms the fact that a low altitude orbiter provides more information content in the Doppler data than a higher altitude orbiter [20]. This is a consequence of the higher orbital velocity and shorter orbital period associated with the low altitude orbiter, which means that the relative approach dynamics are changing more rapidly. As a result, the covariance reduces at a significantly lower rate for MTO than for MRO, as shown in the figures.

Figure 5.20: Position errors with MTO when the difference in RAAN is 90 deg and the a priori uncertainty is large

Figure 5.21: Velocity errors with MTO when the difference in RAAN is 90 deg and the a priori uncertainty is large
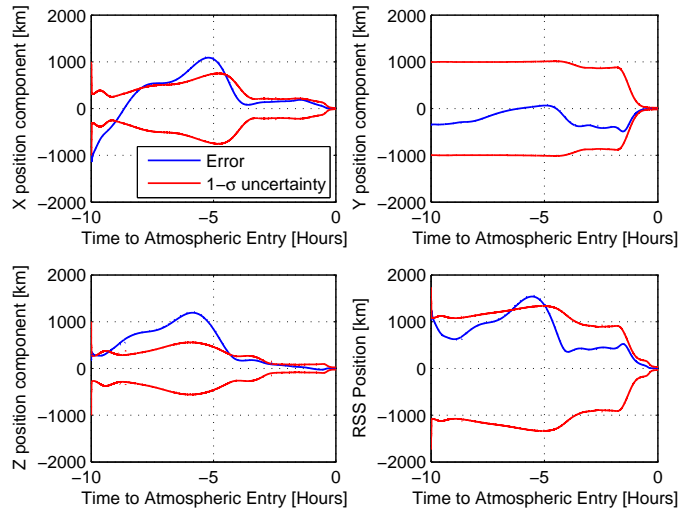
Figure 5.22: Position errors with MTO when the difference in RAAN is 45 deg and the a priori uncertainty is large
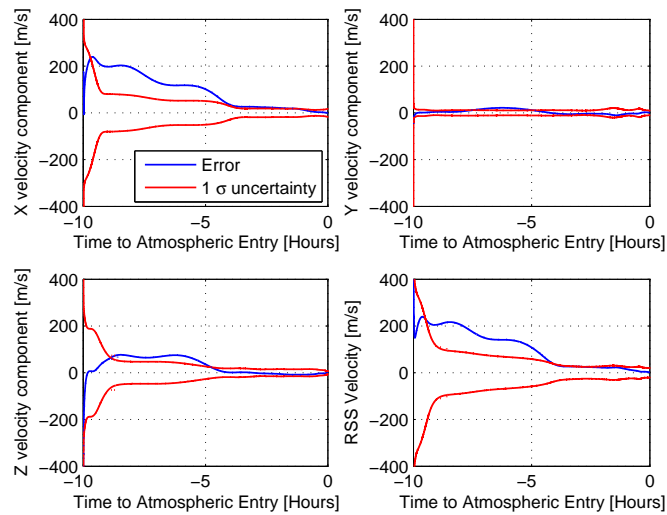
Figure 5.23: Velocity errors with MTO when the difference in RAAN is 45 deg and the a priori uncertainty is large

150
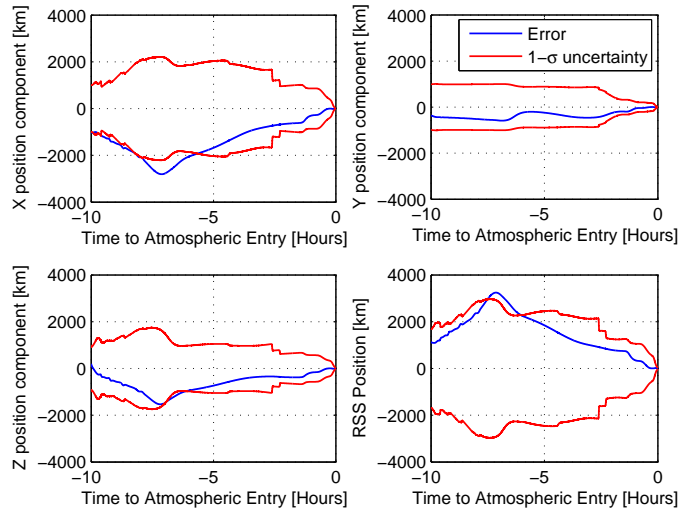
Figure 5.24: Position errors with MTO when the difference in RAAN is 0 deg and the a priori uncertainty is large
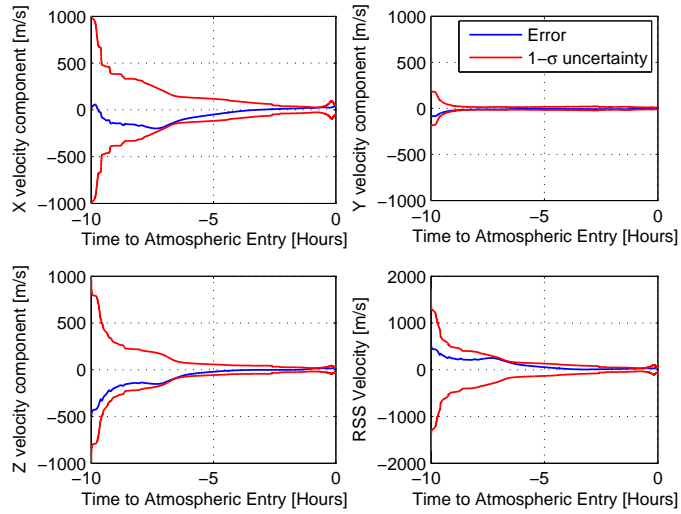
Figure 5.25: Velocity errors with MTO when the difference in RAAN is 0 deg and the a priori uncertainty is large
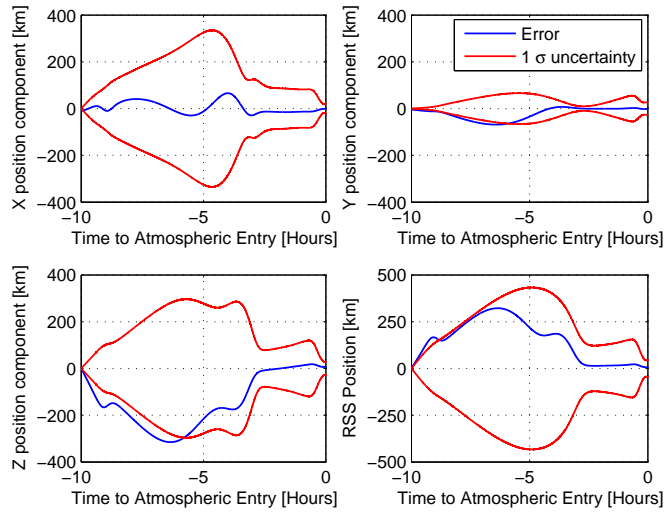
Figure 5.26: Position errors with MTO when the difference in RAAN is 90 deg and the a priori uncertainty is small
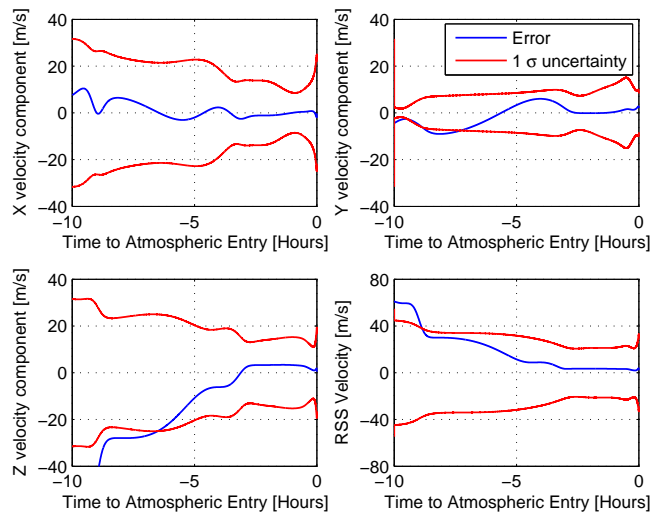
Figure 5.27: Velocity errors with MTO when the difference in RAAN is 90 deg and the a priori uncertainty is small
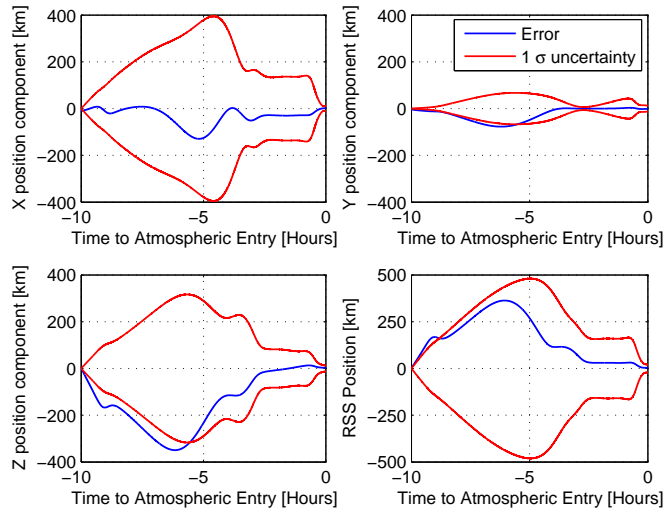
Figure 5.28: Position errors with MTO when the difference in RAAN is 45 deg and the a priori uncertainty is small
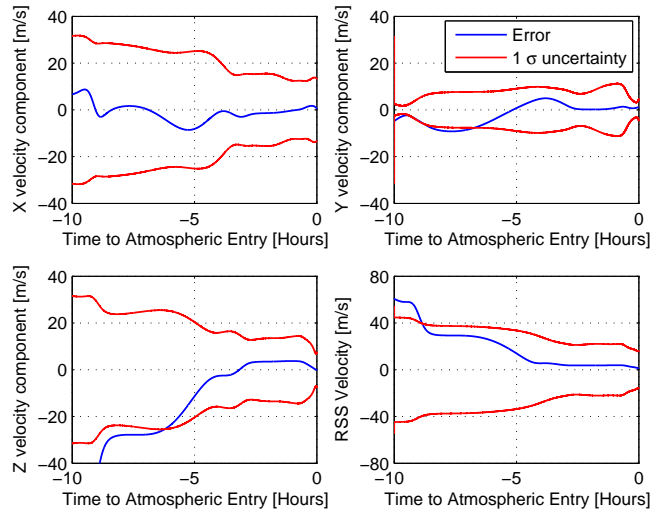
Figure 5.29: Velocity errors with MTO when the difference in RAAN is 45 deg and the a priori uncertainty is small
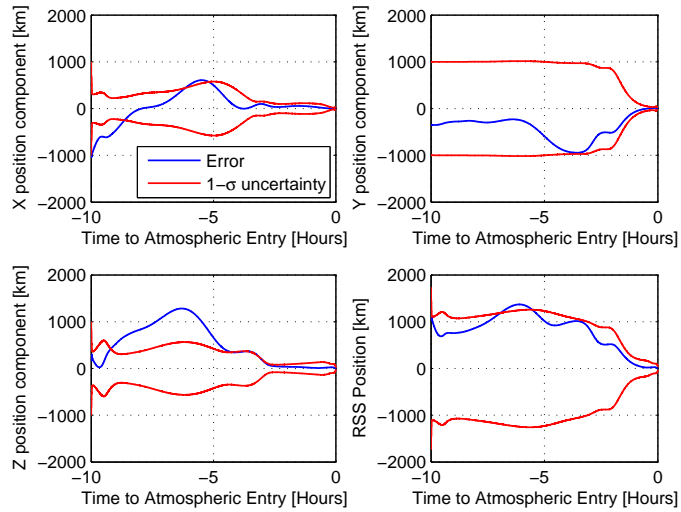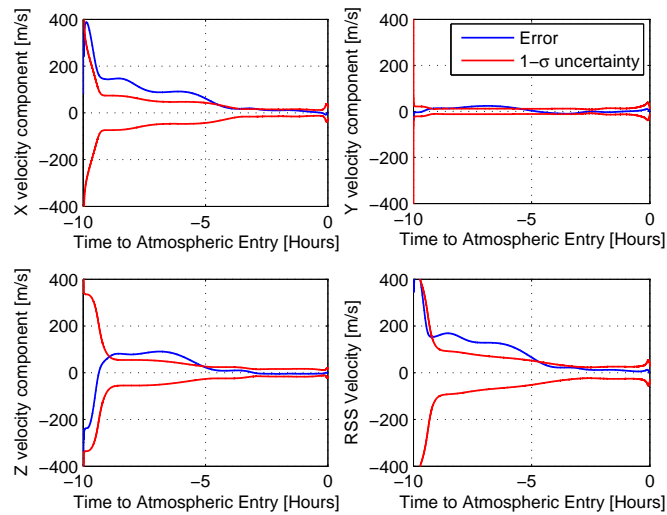
153
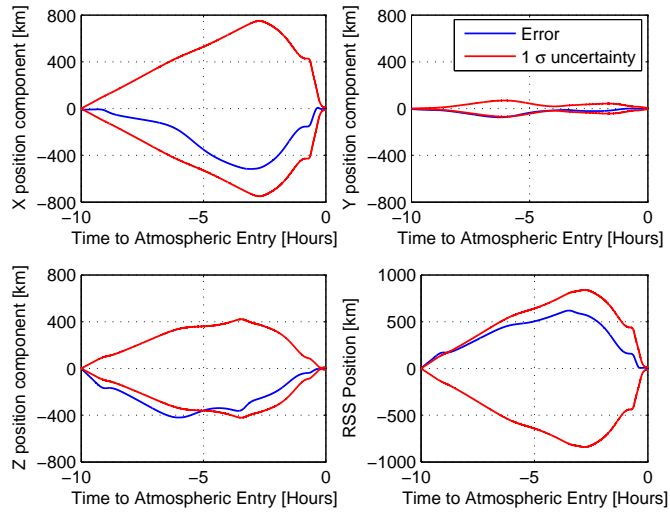
Figure 5.30: Position errors with MTO when the difference in RAAN is 0 deg and the a priori uncertainty is small
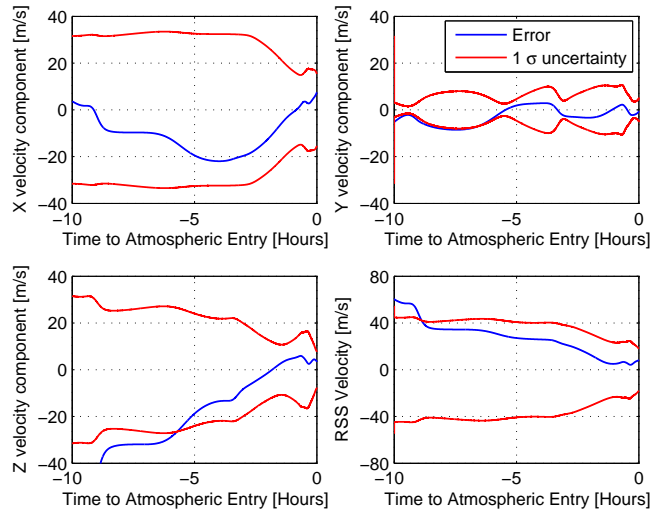
Figure 5.31: Velocity errors with MTO when the difference in RAAN is 0 deg and the a priori uncertainty is small

5.5.4 Summary of the Navigation Performance

The results of the navigation performance analysis revealed the navigation accuracy and the information content available in the raw Electra navigation data. The analysis revealed that certain orbital geometries, where the difference in RAAN between the MAV orbit and the MNO orbit is close to zero, are unfavorable from a navigational point of view and can lead to observability problems in some of the position components. The analysis also revealed that even for the most favorable orbital geometries there is an observability problem in the along-track direction. This observability problem can only be solved by adding another measurement data type to the navigation filter or by collecting Doppler data from another source, which has a large angular separation from the Mars Network orbiter, such as a source on the Earth. A viable solution to the observability problem in the along-track direction is to add DSN tracking data to the navigation filter. As previously mentioned, DSN data will be available up to the data cutoff time of six hours prior to atmospheric entry. Consequently, it is anticipated that the accuracy of the navigation solution can be increased by adding DSN tracking data.

Finally, the analysis revealed that from a navigational point of view, a low-altitude orbiter such as MRO is preferable to a higher altitude orbiter such as MTO. This is a consequence of the relative approach dynamics, which are more rapidly changing for a lower altitude orbiter. (This is in contrast to the requirements of the tracking loop, which favor the less severe dynamics associated with a higher altitude orbiter.)

Chapter 6

Conclusions

6.1 Conclusions

The objective of this dissertation was to develop a navigation filter for Mars final approach, based on the Electra UHF transceiver, which incorporates an accurate model of the error in the two-way Doppler measurement. In order to achieve this, the relative dynamics and the link budget between a Mars approach vehicle and a Mars Network orbiter were analyzed during the final approach phase to determine the expected operating environment of the Electra transceiver. A model of the Electra signal was developed on the basis of the results of the dynamic analysis and the link analysis and was used as input to high-fidelity simulations of the Electra transceiver. The simulations formed the basis of a Monte Carlo analysis, which was used to determine the acquisition and tracking performance of the Electra transceiver for a range of signal and tracking loop parameters. The performance analysis was used to characterize the steady-state tracking error and to develop a model of the error in the two-way Doppler measurement as a function of the SNR. The error model was incorporated into the design of the navigation filter, in order to create an EKF that was adaptive to the changing operating environment of the Electra transceiver throughout the final approach phase.

6.1.1 Conclusions of the Dynamic Analysis

The analysis of the relative approach dynamics between the MAV and the MNO during the final approach was facilitated by a MATLAB simulation tool, which included a rigid-body spacecraft model and an occultation model. The analysis revealed the maximum Doppler shift and Doppler rate and the number of occultations and their average duration as a function of orbital geometry. For a scientific orbiter, such as MRO, which is characterized by a near-circular, near-polar orbit, the Doppler shift and Doppler rate are primarily functions of the difference in RAAN between the orbits of the MAV and MNO. Maximum values of Doppler shift and Doppler rate were found to be approximately 10.5 kHz and 8.5 Hz/s, respectively. Furthermore, it was found that there were, on average, six occultations, with each occultation lasting approximately 40 minutes. For other missions such as MTO or MEX, which utilize highly-eccentric orbits, the relative approach dynamics depend not only on the RAAN, but also on the argument of periapsis and the true anomaly. In this case, the relative approach dynamics are, in general, less severe due to the lower orbital velocity over most of the orbit. In addition, the number of occultations are generally less than two, however, each occultation may last up to 200 minutes for some unfavorable orbit geometries.

6.1.2 Conclusions of the Link Analysis

The two-way link budget between the MAV and the MNO during the final approach was also analyzed using a MATLAB simulation tool, which in-

cluded a spacecraft attitude model and an antenna radiation pattern model. The model of the spacecraft attitude allowed the antenna boresight vectors to be determined, which in turn, allowed the proper antenna gain to be determined when used in conjunction with the model of the antenna radiation patterns. The analysis revealed the total received power and the SNR of the received signal as a function of the range between the MAV and the MNO. The analysis revealed that the link can be closed at a range of approximately 110,000 km, which corresponds to 10 hours prior to atmospheric entry. (This result is based on laboratory tests of the Electra transceiver to determine the minimum power required to close the link.) For a scientific orbiter such as MRO, this corresponds to six passes where tracking data can be collected, with each pass lasting approximately one hour. Furthermore, the analysis revealed that the SNR of the received signal is strongly dependent on the signal data rate. For a BPSK modulated signal with a data rate of 1 ksps, the SNR varied from −10 dB to +20 dB throughout the final approach. At higher data rates, the SNR decreases substantially. To aid long range signal acquisition, the Electra can also transmit a carrier-only signal. The link analysis revealed that the SNR for a carrier-only signal varied from +20 dB to +50 dB throughout the final approach.

6.1.3   Conclusions of the Performance Analysis

The performance of the Electra transceiver was analyzed with respect to the maximum range at which the link can be closed and with respect to the

ability of the tracking loop to acquire and track the Electra signal for different signal and tracking loop parameters. The link analysis, described above, revealed that the link can be closed at a range of approximately 110,000 km. The performance analysis showed that either increasing the transmitted power above the nominal value of 8.5 W or increasing the transmitter antenna gain above the nominal value of 3.5 dB are both viable options for substantially increasing the range at which the link can be closed. For example, the link closure range could be increased to 135,000 km, which corresponds to approximately 12 hours prior to atmospheric entry, by either increasing the transmitted power to 12 W or increasing the transmitter antenna gain to 5 dB. The performance analysis also showed that the SNR could be substantially improved by reducing the system noise temperature below the nominal value of 526 K. Increasing the SNR would enable signals with higher data rates to be transmitted.

A Monte Carlo analysis was performed to determine the acquisition performance of the Electra transceiver for carrier-only, residual carrier, and suppressed carrier signals for different signal and tracking loop parameters. The analysis revealed that the acquisition performance is strongly dependent on the SNR but independent of the Doppler shift up to 10 kHz. Specifically, the analysis revealed that the acquisition performance for a carrier-only signal is greatest when the tracking loop bandwidth is on the order of 0.1 kHz, in which case the carrier-only signal can be acquired reliably when the SNR is -4 dB or higher. On the other hand, for a residual carrier signal and a suppressed

carrier signal, the analysis revealed that the tracking loop bandwidth required to maximize the acquisition performance depends on the data rate. For data rates on the order of 128 ksps, a tracking loop bandwidth on the order of 1 kHz is required to maximize the acquisition performance, while a tracking loop bandwidth on the order of 0.1 kHz is required for data rates on the order of 1 ksps. Finally, the analysis showed that a residual carrier signal can be acquired reliably when the SNR is 0 dB or higher, while a suppressed carrier signal can be acquired reliably when the SNR is 3 dB or higher. Consequently, the Electra transceiver can only acquire a carrier-only signal at the maximum range of 110,000 km, which is the point when the link can initially be closed. It is not until a range of approximately 35,000 km, which corresponds to just 2 hours prior to atmospheric entry, that the Electra transceiver can reliably acquire a 1 ksps residual carrier or suppressed carrier signal.

A Monte Carlo analysis was also performed to determine the tracking performance of the second-order tracking loop for a tracking loop bandwidth of 0.1 kHz. The analysis revealed that the tracking performance is dependent on the time interval between the carrier phase measurements used to formulate the integrated Doppler observable and that a time interval of at least 1 s is required in order to meet the navigation performance requirements of a maximum range rate error of 0.1 mm/s on a 20 second count interval. Furthermore, the analysis revealed that the error in the measurement of the Doppler shift and the variance of the error are dependent on the SNR but independent of the Doppler shift up to 10 kHz.

6.1.4 Conclusions of the Navigation Filter Design

A navigation filter based on the Electra transceiver and suitable for Mars final approach was designed. The filter design was based on a standard EKF, where the dynamic model included the Mars gravitational potential, the Mars J_2 perturbation, and the Mars atmospheric perturbation. The measurement model was based on the range rate formulation of the Doppler shift, which provided an explicit relationship between the spacecraft states and the Doppler measurement. The measurement model included a model of the error in the Doppler measurement, which was determined by the tracking performance analysis. The tracking performance analysis revealed the characteristics of the steady-state tracking error. The bounds on the error and the variance of the error as a function of the SNR were modeled and included in the EKF design. The resulting navigation filter is adaptive to the changing operating environment.

The performance of the navigation filter was analyzed for different Mars Network orbiters and for different orbital geometries. The analysis revealed that the information content in the Doppler measurement depends on the relative geometry between the MAV and MNO orbits and that for some unfavorable orbits, the information content is not sufficient to overcome the growth in covariance from the natural system dynamics. Furthermore, the analysis revealed that the information content is higher for a low-altitude orbiter such as MRO than for a dedicated telecommunications orbiter such as MTO. Consequently, from a purely navigational point of view, a low altitude orbiter is

161

preferable to a high-altitude orbiter, even when occultations are included in the analysis. (This is in contrast to the tracking requirements of the transceiver, where a high-altitude orbiter is preferable due to the less severe dynamics.)

6.2   Future Work

There exist significant opportunities for further work on the topic of real-time navigation for Mars final approach using the Mars Network and the Electra transceiver. The main areas in which the dissertation research could be expanded upon include:

1. Extending the capabilities of the Electra MATLAB model in order to increase the tracking times and to include Doppler rates in the simulations.

2. Hardware testing the Electra engineering development unit in order to verify the performance analysis.

3. Increasing the fidelity of the Doppler measurement model in the navigation filter design to account for the carrier phase measurements and the time delays.

There exists also the remote possibility of collecting flight data between any of the current or future Mars missions, such as the 2001 Mars Odyssey orbiter, the 2005 MRO orbiter, the 2007 Phoenix Mars mission, and the 2009 MSL mission. The flight data could be transmitted to Earth and

post-processed in a navigation filter in order to verify the performance of the filter design.

6.2.1 Improving the Electra MATLAB Model

The Electra MATLAB model is currently limited by the long simulation run-times and the large memory storage requirements. The long run-times are a consequence of the sample period of the tracking loop, which is on the order of 50 ns. To simulate a tracking time on the order of one second, requires a simulation run-time on the order of 1000 seconds. This becomes significant in a Monte Carlo-style analysis, where hundreds or thousands of simulation runs may be performed. As a result of the short tracking times, Doppler rates are not included in the simulations, although they represent the operating conditions more closely than a constant Doppler shift. This omission is negligible for the approach analysis, where the Doppler rates are fairly benign since they are generally less than 8.5 Hz/s. The same cannot be said for the surface positioning of landed assets on Mars, where the dynamics associated with an overhead satellite pass result in Doppler rates of up to 60–70 Hz/s. In this case, the effect of Doppler rates on the acquisition and tracking performance of the Electra transceiver could be significant. Thus, increasing the tracking time and including Doppler rates in the simulation would allow the performance for surface positioning to be analyzed. Furthermore, the benefit of increasing the tracking loop order from second- to third-order to eliminate the steady-state tracking error associated with a Doppler rate could be investigated.

6.2.2 Hardware Testing of the Electra EDU

The performance analysis of the Electra transceiver presented in the dissertation is based on software simulations of the Electra MATLAB model. Although the model is a high-fidelity model that represents a bit-to-bit mapping of the functions implemented in the actual flight FPGA and includes correct levels of quantization, it is still an approximation of the actual transceiver. As such, there are certain limitations to the model. In order to verify the performance analysis and ensure the accuracy of the results, it is necessary to test the Electra transceiver in hardware using the Electra engineering development unit. The same set of analysis presented in the dissertation should be repeated for the Electra EDU.

6.2.3 Improving the Navigation Filter Measurement Model

The Doppler measurement model in the navigation filter is a simple model, based on the range rate between the Mars approach vehicle and the Mars Network orbiter. A more detailed model of the Doppler measurement, based on the carrier phase measurements and the time delays associated with the signal transmission, should be developed and included in the EKF design. This would increase the fidelity of the navigation results and lead to a more realistic analysis of the navigation performance.

Appendices

Appendix A

Electra Modulation Architecture

A binary phase-shift keying (BPSK) signal can represented as:

$$x(t) = A \cos \left[2\pi f_c t + \delta d(t) + \theta(t) \right] \quad \text{for } 0 < t < T_s \qquad \text{(A.1)}$$

where

$$
\begin{aligned}
f_c &= \quad \text{Carrier frequency} \\
A &= \quad \text{Signal amplitude} \\
\delta &= \quad \text{Modulation index} \\
d(t) &= \quad \text{Binary valued } (\pm 1) \text{ data corresponding to either NRZ or} \\
&\qquad \text{Manchester encoded data} \\
\theta(t) &= \quad \text{Input phase offset} \\
T_s &= \quad \text{Bit duration}
\end{aligned}
$$

Equation A.1 can be expanded as follows:

$$x(t) = A \cos \delta d(t) \cos \left[2\pi f_c t + \theta(t) \right] - A \sin \delta d(t) \sin \left[2\pi f_c t + \theta(t) \right] \qquad \text{(A.2)}$$

Equation A.2 can be simplified using the even symmetry of the cosine function and the odd symmetry of the sine function:

$$x(t) = A \cos \delta \cos \left[2\pi f_c t + \theta(t) \right] - A d(t) \sin \delta \sin \left[2\pi f_c t + \theta(t) \right] \qquad \text{(A.3)}$$

The power associated with the transmitted signal $x(t)$ is given by:

$$P = \frac{1}{T} \int_0^T |x(t)|^2 dt \qquad (A.4)$$

where T is the period of the signal. Equation A.3 can be squared and substituted into Equation A.4, giving:

$$P = \frac{A^2 \cos^2 \delta}{T} \int_0^T \cos^2 \left[2\pi f_c t + \theta(t) \right] dt + \frac{A^2 \sin^2 \delta}{T} \int_0^T \sin^2 \left[2\pi f_c t + \theta(t) \right] dt$$

$$- \frac{A^2 d(t) \sin \delta \cos \delta}{T} \int_0^T \sin 2 \left[2\pi f_c t + \theta(t) \right] dt \quad (A.5)$$

Since the rates at which the binary data $d(t)$ and the phase angle $\theta(t)$ change are much less than the carrier frequency f_c, they can be considered constant over the period T of the signal. Using this observation, Equation A.5 reduces to:

$$P = P_c + P_d = \frac{A^2 \cos^2 \delta}{2} + \frac{A^2 \sin^2 \delta}{2} \qquad (A.6)$$

The first term corresponds to the power P_c associated with the carrier signal, while the second term corresponds to the power P_d associated with the data component.

The transmitted signal $x(t)$ is a residual carrier signal when the modulation index is given by $0 < \delta < \pi/2$ rad. In this case, the transmitted signal can be represented by:

$$x(t) = \sqrt{2P_c} \cos \left[2\pi f_c t + \theta(t) \right] - \sqrt{2P_d} \, d(t) \sin \left[2\pi f_c t + \theta(t) \right] \qquad (A.7)$$

where the first term corresponds to the residual carrier and the second term corresponds to the data signal.

Conversely, when the modulation index is $\delta = \pi/2$ rad, the transmitted signal $x(t)$ is a suppressed carrier signal. In this case, the transmitted signal can be represented as:

$$x(t) = \sqrt{2P_d}\, d(t) \cos\left[2\pi f_c t + \theta(t)\right] \tag{A.8}$$

Note that the residual carrier power in Equation A.6 is zero for the suppressed carrier signal where $\delta = \pi/2$ rad, as expected.

The binary-valued data $d(t)$ can be encoded in one of two data formats, either nonreturn-to-zero (NRZ) or Manchester data format. The two data formats are illustrated in Figure A.1. The NRZ format uses a positive pulse to represent a $+1$ bit and a negative pulse to represent a -1 bit, while the Manchester format uses a bit transition from $+1$ to -1 to represent a $+1$ bit and a bit transition from -1 to $+1$ to represent a -1 bit. Consequently, the bit rate is equal to the symbol rate for the NRZ encoded data, while the bit rate is twice the symbol rate for the Manchester encoded data.

The power spectral density associated with the NRZ and Manchester encoded data pulses are given by [63]:

$$P(f) = \begin{cases} T_s \frac{\sin^2 \pi f T_s}{(\pi f T_s)^2} & \text{for NRZ} \\[2ex] T_s \frac{\sin^4 \pi f T_s/2}{(\pi f T_s/2)^2} & \text{for Manchester} \end{cases} \tag{A.9}$$

where T_s is the bit duration. The power spectra for both the NRZ and the Manchester data formats are shown in Figure A.2 for $T_s = 10\,\mu s$, which shows that for a given data rate $R_s = 1/T_s$, the main lobe width of the NRZ encoding is half of the main lobe width of the Manchester encoding. Hence, NRZ

168
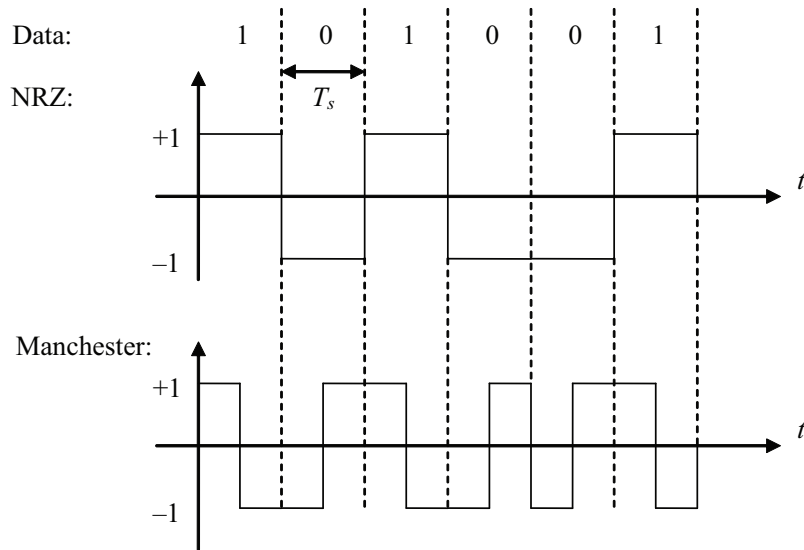
Figure A.1: Nonreturn-to-zero (NRZ) and Manchester data formats
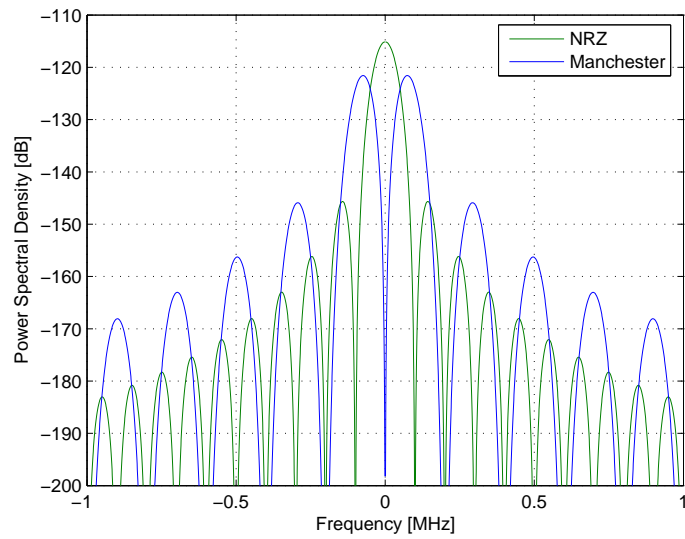
Figure A.2: Power spectral density for NRZ and Manchester data encoding with $T_s = 10\,\mu s$

169

encoding is generally preferable to Manchester encoding. However, there is a spectral null in the middle of the Manchester spectra. This enhances residual carrier tracking by removing the interference from the data component of the signal. Consequently, NRZ encoding is used for suppressed carrier transmission while Manchester encoding is used for residual carrier transmission.

The BPSK signal given by Equation A.1 can also be represented in complex baseband form. Here $z(t)$ is the complex baseband BPSK signal before it has been mixed up to the desired carrier frequency.

$$z(t) = Ae^{j[\delta d(t)+\theta(t)]} = A\big[\cos\delta + jd(t)\sin\delta\big]e^{j\theta(t)} \qquad \text{(A.10)}$$

The complex baseband representation given in Equation A.10 can be extended to include quadriphase-shift keying (QPSK) modulation in addition to BPSK [47]. The complex baseband QPSK signal is now given by:

$$z(t) = A\big[\cos\delta d_I(t) + j\sin\delta d_Q(t)\big]e^{j\theta(t)} \qquad \text{(A.11)}$$

where $d_I(t)$ and $d_Q(t)$ are independent, binary-valued data corresponding to either NRZ or Manchester encoded data. For residual carrier BPSK modulation,

$$d_I(t) = 1, \quad d_Q(t) = d(t) \quad \text{and} \quad \delta = \pi/3\,\text{rad.} \qquad \text{(A.12)}$$

For suppressed carrier BPSK modulation either

$$d_I(t) = 1, \quad d_Q(t) = d(t) \quad \text{and} \quad \delta = \pi/2\,\text{rad} \qquad \text{(A.13)}$$

or

$$d_I(t) = d_Q(t) = d(t) \quad \text{and} \quad \delta = \pi/4\,\text{rad.} \qquad \text{(A.14)}$$

170
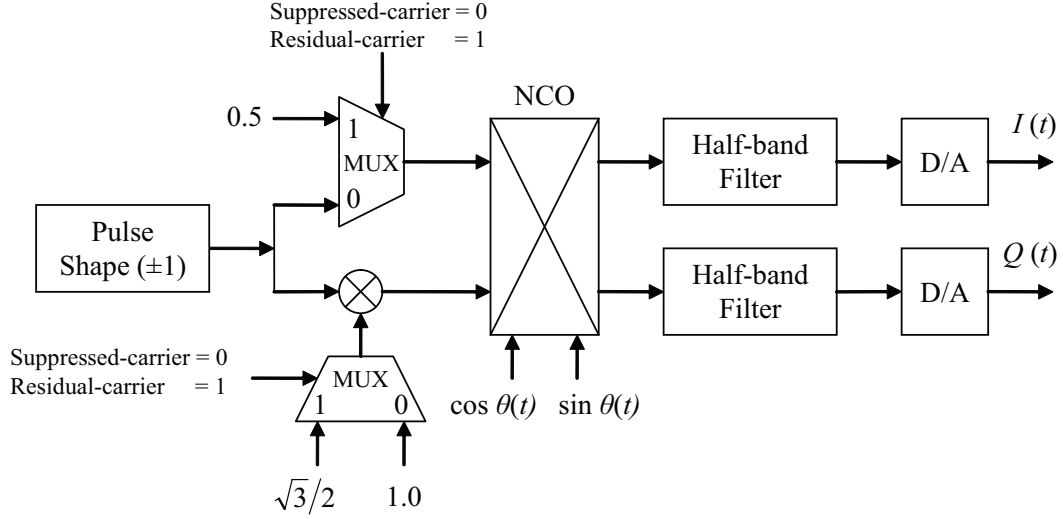
Figure A.3: Electra modulator architecture

The latter option rotates the BPSK modulation by 45 degs. Hence for balanced QPSK modulation, $d_I(t)$ and $d_Q(t)$ are set to independent data streams and $\delta = \pi/4$ rad. Figure A.3 shows the Electra modulation architecture for generating both the residual carrier and suppressed carrier BPSK signal [48].

When the Electra modulator operates in the residual carrier mode, the in-phase and the quadrature-phase data components are set to:

$$\cos \delta d_I(t) = 0.5 \quad \text{and} \quad \sin \delta d_Q(t) = \pm \sqrt{3}/2, \tag{A.15}$$

as shown in Figure A.3. The data components are then complex multiplied with the phase angle $\theta(t)$ from the NCO. Note that the modulator NCO may include Doppler turnaround when the Electra operates in transponder mode.

The digital baseband signals are sent through digital 10th-order half-band filters for purposes of bandlimiting and then through a D/A converter, resulting in:

$$
\begin{aligned}
I(t) &= \text{Re}\big[z(t)\big] \\
&= 0.5\cos\theta(t) \mp \sqrt{3}/2\sin\theta(t) && \text{(A.16)} \\
Q(t) &= \text{Im}\big[z(t)\big] \\
&= 0.5\sin\theta(t) \pm \sqrt{3}/2\cos\theta(t) && \text{(A.17)}
\end{aligned}
$$

The analog baseband signals are then mixed-up (I/Q-modulated) to the nominal carrier frequency f_c for UHF transmission:

$$
\begin{aligned}
x(t) &= I(t)\cos 2\pi f_c t - Q(t)\sin 2\pi f_c t \\
&= 0.5\cos\big[2\pi f_c t + \theta(t)\big] \mp \sqrt{3}/2\sin\big[2\pi f_c t + \theta(t)\big] \\
&= \cos\big[2\pi f_c t + \theta(t) \pm \pi/3\big] && \text{(A.18)}
\end{aligned}
$$

Conversely, when the Electra modulator operates in the suppressed carrier mode, the in-phase and quadrature-phase data components are set to:

$$
\cos\delta d_I(t) = \sin\delta d_Q(t) = \pm 1.0, \qquad\qquad \text{(A.19)}
$$

as shown in Figure A.3. After complex multiplication with the modulator NCO phase angle $\theta(t)$, digital lowpass filtering, and D/A conversion, the analog

baseband signals are given by:

$$I(t) = \mathrm{Re}\big[z(t)\big]$$

$$= \pm \cos \theta(t) \mp \sin \theta(t) \tag{A.20}$$

$$Q(t) = \mathrm{Re}\big[z(t)\big]$$

$$= \pm \cos \theta(t) \pm \sin \theta(t) \tag{A.21}$$

The analog baseband signals are then mixed-up (I/Q-modulated) to the nominal carrier frequency f_c for UHF transmission:

$$x(t) = I(t) \cos 2\pi f_c t - Q(t) \sin 2\pi f_c t$$

$$= \pm \cos \big[2\pi f_c t + \theta(t)\big] \mp \sin \big[2\pi f_c t + \theta(t)\big]$$

$$= \pm \sqrt{2} \cos \big[2\pi f_c t + \theta(t) + \pi/4\big] \tag{A.22}$$

Appendix B

Phase-Locked Loops

B.1   Introduction

The Electra transceiver uses a standard digital PLL to track the frequency and phase of the received signal, when the signal is a residual carrier signal. Conversely, when the received signal is a suppressed carrier signal, the Electra transceiver uses a Costas PLL to track the frequency and phase of the signal. The following sections will provide a brief introduction to both standard PLLs and Costas PLLs. To simplify the analysis, the continuous-time case will be examined. The extension to discrete-time is straight forward.

B.2   Phase-Locked Loops

A general PLL consists of a phase detector, a loop filter, and a voltage controlled oscillator (VCO) as shown in Figure B.1. There are several different types of phase detectors, each with different operating properties. It will assumed in the following analysis that the phase detector consists of a multiplier, a lowpass filter that removes the second harmonic of the carrier signal, and an inverter to remove the negative sign.

A simplified model of the residual carrier signal that is received at the

174
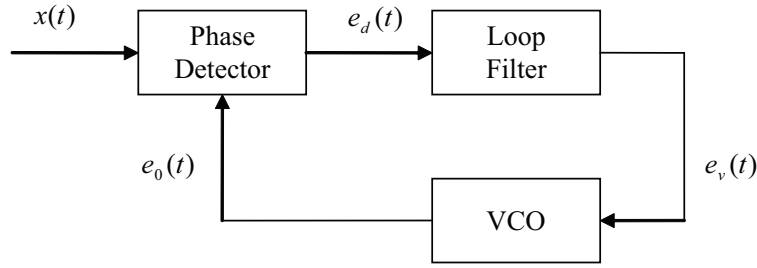
Figure B.1: Block diagram of a PLL

input to the PLL can be represented by:

$$x(t) = A_c \cos \left[\omega_c t + \phi(t) \right] \tag{B.1}$$

where A_c is the amplitude, ω_c is the carrier frequency, and $\phi(t)$ is the phase angle, which contains the data signal. The instantaneous phase angle $\phi_i(t)$ and the instantaneous frequency $\omega_i(t)$ are given by:

$$\phi_i(t) = \omega_c t + \phi(t) \tag{B.2}$$

$$\omega_i(t) = \omega_c + \dot{\phi}(t) = \omega_c + df \tag{B.3}$$

where df is the Doppler shift. The result of the Doppler shift is to change the instantaneous frequency of the received signal. However, this can be modeled equivalently as a change in the phase angle, as given by:

$$\phi(t) = \phi(t_0) + 2\pi \int_0^t df \, dt \tag{B.4}$$

The VCO is essentially a frequency modulator, where the frequency deviation of the VCO output signal $\dot{\theta}(t)$ is proportional to the VCO input

175
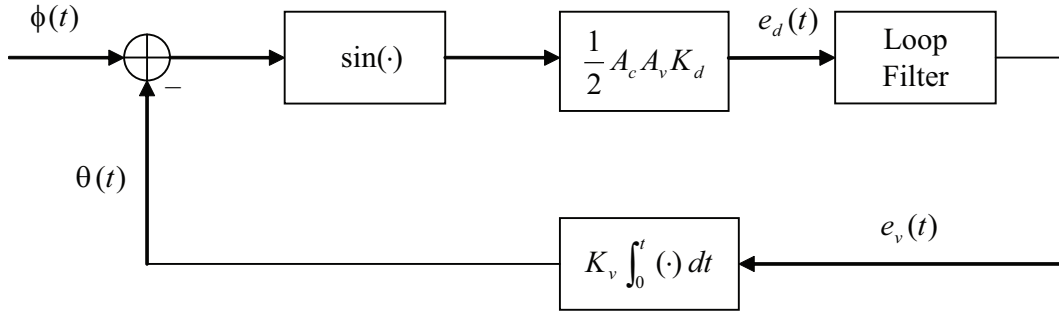
Figure B.2: Nonlinear model of a PLL

signal, as shown below:

$$\dot{\theta}(t) = K_v e_v(t) \tag{B.5}$$

$$\theta(t) = K_v \int_0^t e_v(\tau) d\tau \tag{B.6}$$

where K_v is the VCO multiplier constant. Then the output of the VCO can be modeled as:

$$e_0(t) = A_v \sin \left[\omega_c t + \theta(t)\right] \tag{B.7}$$

The output of the phase detector, which is assumed to consist of a multiplier, a lowpass filter, and an inverter is given by:

$$e_d(t) = \frac{1}{2} A_c A_v K_d \sin \left[\phi(t) - \theta(t)\right] \tag{B.8}$$

where K_d is the phase detector multiplier constant. The output of the phase detector depends only on the phase error between the phase $\phi(t)$ of the input to the PLL and the phase $\theta(t)$ of the output of the VCO. Consequently, the PLL can be modeled without regard to the carrier frequency ω_c. The resulting

176
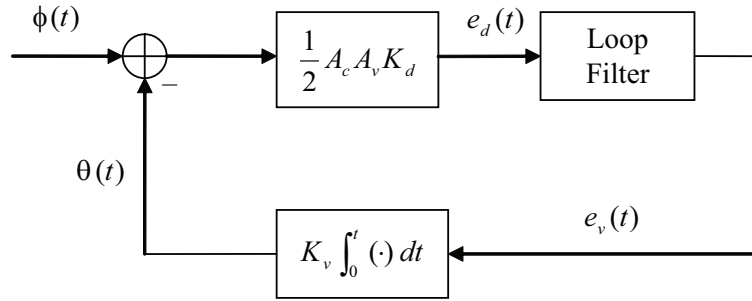
Figure B.3: Linearized model of a PLL

nonlinear model of the PLL is shown in Figure B.2, where the nonlinearity is a result of the sine function.

When the PLL is operating in lock, the phase $\theta(t)$ of the VCO output is a good estimate of the phase $\phi(t)$ of the input. Hence, the phase error is small and the following approximation can be made:

$$\sin\left[\phi(t) - \theta(t)\right] \cong \phi(t) - \theta(t) \tag{B.9}$$

which leads to the linearized model of the PLL shown in Figure B.3

So far no comments have been made in regards to the loop filter. It is the order and type of the loop filter that will determine the overall order of the PLL and its transient and steady-state performance. In the following sections, first-, second-, and third-order loop filters will be developed and the overall performance of the PLL will be analyzed and compared.
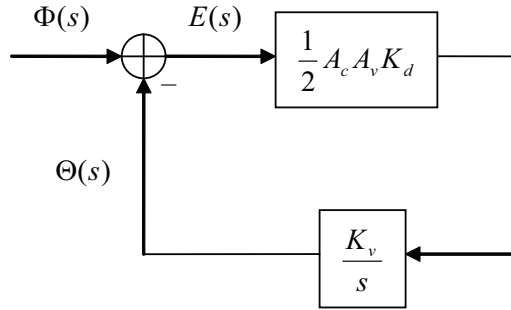
Figure B.4: Linearized, first-order PLL

B.2.1 First-Order PLL

A first-order PLL is the simplest type of PLL and contains no loop filter. The PLL is considered first-order due to the integrator associated with the VCO. A block diagram of the linearized, first-order PLL is shown in Figure B.4. Note that the PLL variables are now shown in terms of their Laplace transforms, where s is the Laplace variable.

The closed-loop transfer function of the PLL is given by:

$$H(s) = \frac{G}{s + G} \tag{B.10}$$

where G is the total effective loop gain, given by:

$$G = \frac{1}{2} A_c A_v K_d K_v \tag{B.11}$$

The phase error is then given by:

$$E(s) = \frac{s}{s + G} \Phi(s) \tag{B.12}$$

178

Table B.1: Steady-state error for a first-order PLL

Input Type	Laplace Transform	Steady-State Error
Phase step	$\frac{\Delta\Phi}{s}$	0
Frequency step	$\frac{\Delta\omega}{s^2}$	$\frac{\Delta\omega}{G}$
Frequency ramp	$\frac{\Delta R}{s^3}$	∞

The final value theorem, given by:

$$e_{ss}(t) = \lim_{s \to 0} sE(s) \tag{B.13}$$

can be used to calculate the steady-state phase error $e_{ss}(t)$ associated with several different types of inputs. The steady-state phase errors for inputs corresponding to a phase step, a frequency step, and a frequency ramp are summarized in Table B.1. The table shows that the first-order PLL can track a phase step input with zero steady-state error and a frequency step input with a finite steady-state error.

The steady-state error associated with a frequency step input can be made arbitrarily small by increasing the total effective loop gain G. However, this can lead to stability problems. A root locus analysis of the closed-loop transfer function $H(s)$ of the linearized PLL, given by Equation B.10, indicates that the requirement for stability is $G > 0$. However, a phase plane analysis of the nonlinear first-order PLL shows that phase lock can be achieved as long
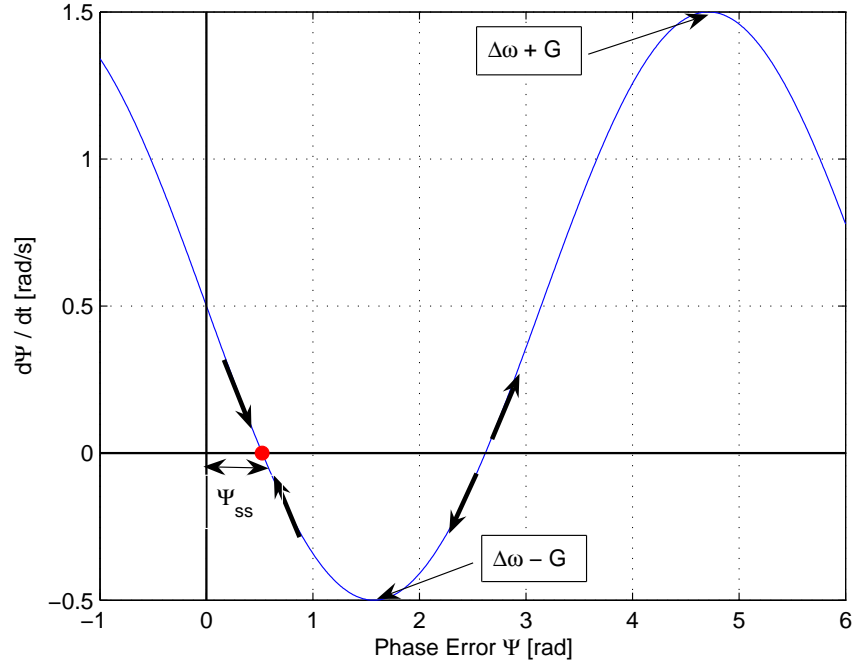
Figure B.5: Phase plane portrait for a first-order PLL

as $\Delta\omega < G$. To show this, consider the phase error $\psi(t)$, given by:

$$\psi(t) = \phi(t) - \theta(t) \tag{B.14}$$

$$\dot{\psi}(t) = \dot{\phi}(t) - G\sin\psi(t) \tag{B.15}$$

where, in the nonlinear model, $\dot{\theta}(t) = G\sin\psi(t)$. For a frequency step of $\dot{\phi}(t) = \Delta\omega$, the resulting phase portrait is shown in Figure B.5. The PLL achieves lock when $\dot{\psi}(t) = 0$. The lock point, indicated by the red dot in Figure B.5, is a stable equilibrium point as small perturbations to either side will tend to return the PLL to the equilibrium point, as indicated by the

180

arrows. In order to achieve lock, the curve must intersect with the $\dot{\psi}(t) = 0$ axis. Consequently, the requirement for lock is $\Delta\omega < G$. Hence, G is the lock range for a first-order PLL. The steady-state error in the nonlinear case is then given by:

$$\psi_{ss}(t) = \sin^{-1}\left(\frac{\Delta\omega}{G}\right) \tag{B.16}$$

Note that when $G < 0$, stable lock points still exist, even though the linear analysis does not indicate their existence. In this case, the stable lock points are displaced by π rad from the stable lock points when $G > 0$.

The case corresponding to the frequency ramp input is interesting as it corresponds to the approach of a spacecraft, where the accelerated motion between the transmitter and receiver leads to a changing Doppler frequency. This corresponds to the type of signal that the Electra will encounter and will need to track. Since a frequency ramp input yields an unbounded steady-state error, a first-order PLL is unable to track this type of input. Consequently, a first-order PLL is unsuitable for the Electra transceiver.

B.2.2 Second-Order PLL

A linear, second-order PLL is shown in Figure B.6 and contains a loop filter that is a perfect integrator. The closed-loop transfer function of the second-order PLL is given by:

$$H(s) = \frac{G(s + \alpha)}{s^2 + Gs + G\alpha} = \frac{2\zeta\omega_n s + \omega_n^2}{s^2 + 2\zeta\omega_n s + \omega_n^2} \tag{B.17}$$
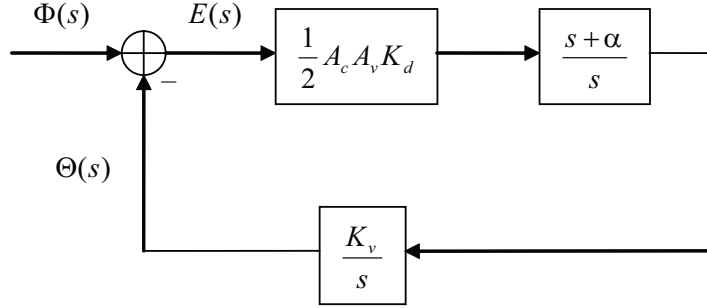
Figure B.6: Linearized, second-order PLL

where the natural frequency ω_n and damping ratio ζ are given by:

$$\omega_n = \sqrt{G\alpha} \qquad\qquad \zeta = \sqrt{\frac{G}{4\alpha}} \qquad\qquad \text{(B.18)}$$

The phase error is given by:

$$E(s) = \frac{s^2}{s^2 + Gs + \alpha}\Phi(s) \qquad\qquad \text{(B.19)}$$

The steady-state phase errors for inputs corresponding to a phase step, a frequency step, and a frequency ramp are found by using the final value theorem, given by Equation B.13. The results are summarized in Table B.2, which shows that a second-order PLL is able to track both a phase step input and a frequency step input with zero steady-state error. Furthermore, the second-order PLL will also track a frequency ramp input, which corresponds to the Electra operating conditions. However, there is a finite steady-state error, whose magnitude depends on the value of the filter constant α.

The root locus for the linear, second-order PLL is shown in Figure B.7, where an arbitrary value of $\alpha = 2$ has been used to generate the root locus

182

Table B.2: Steady-state error for a second-order PLL

Input Type	Laplace Transform	Steady-State Error
Phase step	$\frac{\Delta\Phi}{s}$	0
Frequency step	$\frac{\Delta\omega}{s^2}$	0
Frequency ramp	$\frac{\Delta R}{s^3}$	$\frac{\Delta R}{\alpha}$

plot. The root locus shows that the linear, second-order PLL is stable for all values of the loop gain G. A typical value for the damping ratio of $\zeta = 0.707$ is chosen in order to achieve a fast response, while minimizing the overshoot.

A phase plane analysis of the nonlinear, second-order PLL reveals some interesting characteristics. Figure B.8 shows the phase plane trajectories for frequency steps of 20 Hz, 35 Hz, 40 Hz, and 45 Hz. The trajectories were generated via a numerical simulation of the nonlinear equations for the second-order PLL [65]. The trajectories show that the second-order PLL has an infinite lock range. However, the steady-state error is only zero for the 20 Hz step. For the other steps, the steady-state phase error is an integer multiple of 2π. This phenomenon is called cycle-slip and only arises in the nonlinear analysis.
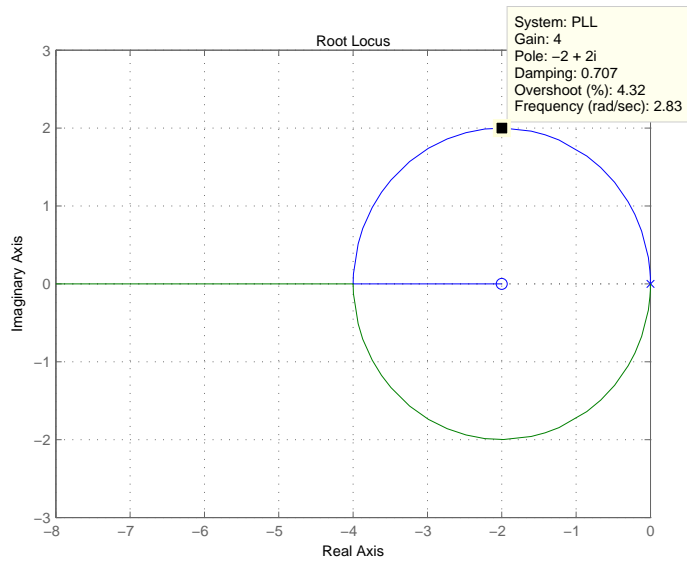
Figure B.7: Root locus for a second-order PLL
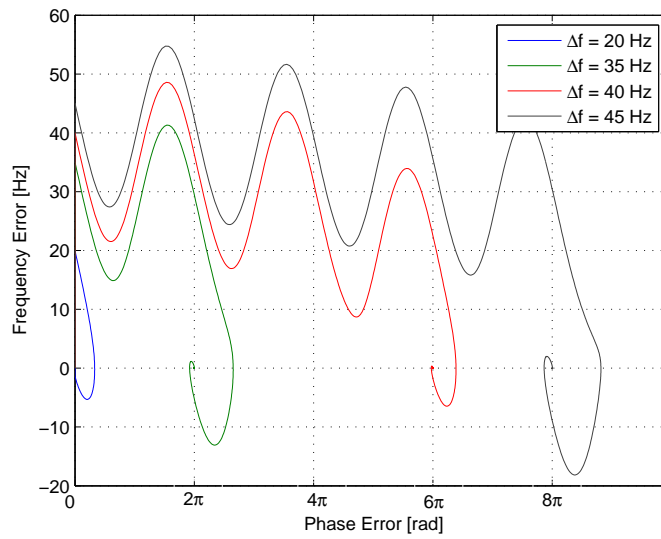
Figure B.8: Phase plane portrait for a second-order PLL

184

B.2.3 Third-Order PLL

A linear, third-order PLL is shown in Figure B.9 and contains a second-order loop filter. The closed-loop transfer function of the third-order PLL is given by:

$$H(s) = \frac{G(s^2 + \alpha s + \beta)}{s^3 + G(s^2 + \alpha s + \beta)} \tag{B.20}$$

The phase error is given by:

$$E(s) = \frac{s^3}{s^3 + G(s^2 + \alpha s + \beta)} \Phi(s) \tag{B.21}$$

The final value theorem given in Equation B.13 can then be used to show that a third-order PLL can track a phase step input, a frequency step input, and a frequency ramp input with zero steady-state error. Thus, a third-order PLL is ideally suited to track a spacecraft signal, where the accelerated motion between the transmitter and receiver causes a continually changing Doppler frequency. However, the increased complexity associated with the analysis and design of a third-order PLL means that a second-order PLL is often used in practice instead.

The stability of the linear, third-order PLL can be analyzed by considering the Routh-Hurwitz criterion, as applied to the characteristic equation. The characteristic equation is the denominator of the closed-loop transfer function $H(s)$, given by Equation B.20. The Routh-Hurwitz criterion leads to the following stability requirements:

$$\alpha > 0, \qquad \beta > 0, \qquad \text{and} \qquad G > \frac{\beta}{\alpha} \tag{B.22}$$
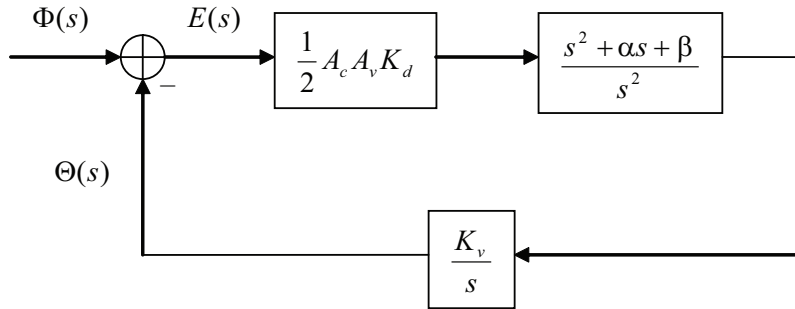
Figure B.9: Linearized, third-order PLL

Consequently, unlike first and second-order loops that are unconditionally stable, a third-order loop requires that the total effective loop gain G be greater than the minimum value given by Equation B.22. The root locus of the closed-loop transfer function $H(s)$ when the two zeros are coincident ($\beta = \alpha^2/4$) is shown in Figure B.10. The cross-over point on the imaginary-axis occurs at the stability boundary, which for coincident roots occurs when $G = 1$.

B.3 Costas Phase-Locked Loops

A Costas PLL is the accepted method of recovering the phantom carrier in a suppressed carrier signal [55] and tracking the phase and frequency of that signal. A typical Costas PLL is shown in Figure B.11 and is similar to a standard PLL, except that the loop consists of two arms, namely, an in-phase arm and a quadrature-phase arm that are phase shifted by 90 deg with respect to each other.

A simplified model of the suppressed carrier signal that forms the input
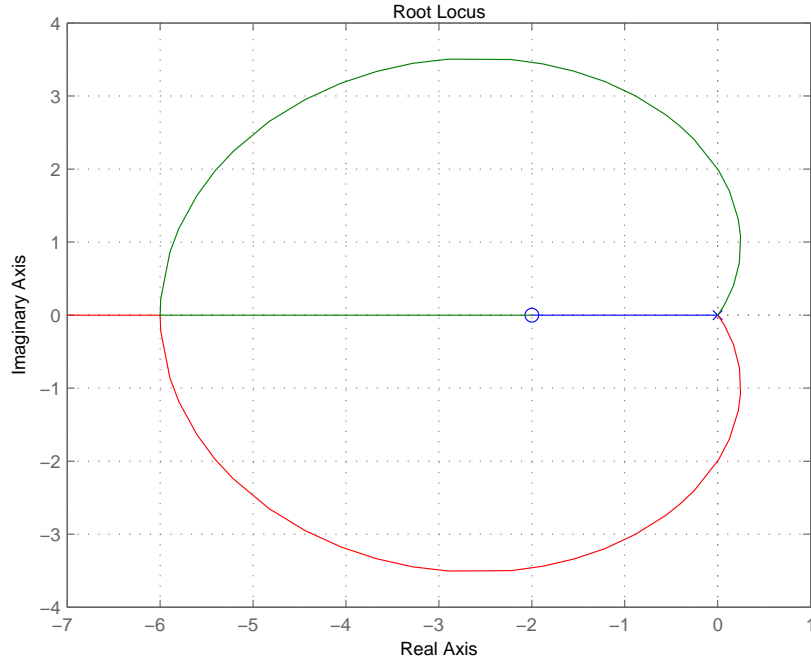
Figure B.10: Root locus for a third-order PLL

to the Costas PLL can be represented by:

$$x(t) = d(t) \cos \left[\omega_c t + \phi(t) \right] \tag{B.23}$$

where $d(t)$ is the data modulation (± 1 digital waveform), ω_c is the carrier frequency, and $\phi(t)$ is the phase angle. The input $x(t)$ is multiplied by the output of the VCO and a 90 deg phase-shifted version of it to form:

$$e_Q(t) = 2d(t) \cos \left[\omega_c t + \phi(t) \right] \cos \left[\omega_c t + \theta(t) \right] \tag{B.24}$$

$$e_I(t) = 2d(t) \cos \left[\omega_c t + \phi(t) \right] \sin \left[\omega_c t + \theta(t) \right] \tag{B.25}$$

where $\theta(t)$ is the phase of the VCO.

187
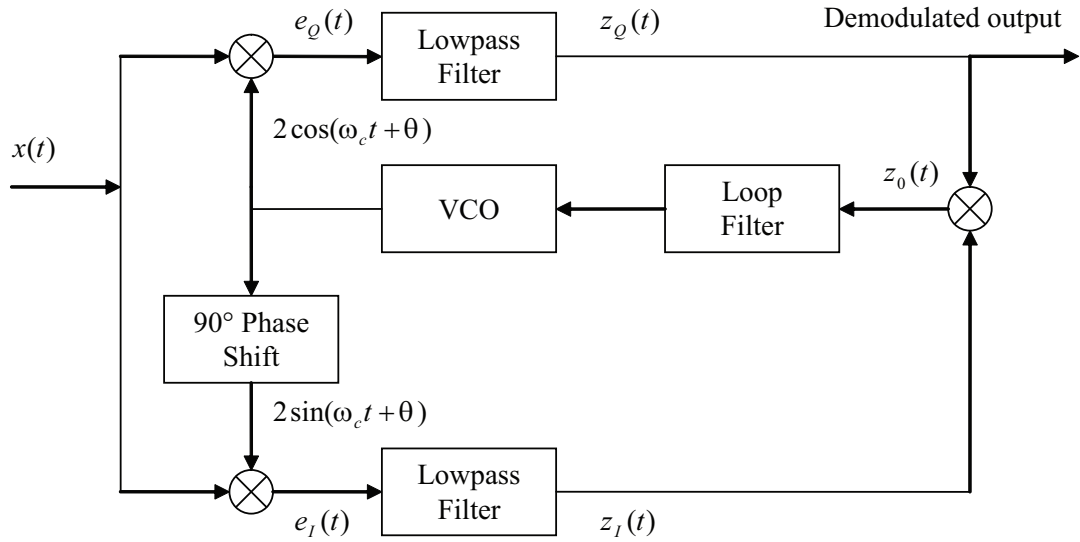
Figure B.11: Block diagram of a Costas PLL

The output of the lowpass filter, which removes the second-harmonic terms of the carrier frequency, is then given by:

$$z_Q(t) \quad = \quad d(t) \cos \left[\theta(t) - \phi(t) \right] \qquad (B.26)$$

$$z_I(t) \quad = \quad d(t) \sin \left[\theta(t) - \phi(t) \right] \qquad (B.27)$$

The dynamic error signal, which forms the input to the loop filter, is the product of the two lowpass filter outputs and is given by:

$$z_0(t) = \frac{1}{2} d(t)^2 \sin 2 \left[\theta(t) - \phi(t) \right] \qquad (B.28)$$

The VCO attempts to drive the phase error $\theta(t) - \phi(t)$ to zero, in which case the signal $z_Q(t)$ becomes the demodulated output of the Costas PLL.

188

Appendix C

Partial Derivatives

The nonlinear equation of motion of the spacecraft is given by:

$$\ddot{\boldsymbol{r}} = \nabla U + \boldsymbol{a}_{Drag} \tag{C.1}$$

where $\ddot{\boldsymbol{r}}$ is the spacecraft inertial acceleration vector, U is the gravitational potential, and $\boldsymbol{a}_{Drag}$ is the atmospheric drag perturbation. If the state vector $\boldsymbol{X}(t)$ is given by the inertial spacecraft position and velocity components, then the nonlinear dynamic model is represented by:

$$\boldsymbol{X}(t) = \begin{bmatrix} x \\ y \\ z \\ \dot{x} \\ \dot{y} \\ \dot{z} \end{bmatrix} \qquad \boldsymbol{F}(\boldsymbol{X}(t)) = \begin{bmatrix} \dot{x} \\ \dot{y} \\ \dot{z} \\ a_{U_x} - \beta\,\rho\,v_{rel}\,a \\ a_{U_y} - \beta\,\rho\,v_{rel}\,b \\ a_{U_z} - \beta\,\rho\,v_{rel}\,c \end{bmatrix} \tag{C.2}$$

where a_U are the acceleration components due to the gravitational potential, which are given by:

$$a_{U_x} = -\frac{\mu}{r^3}x\left\{1 - \frac{3}{2}\left(\frac{R_m}{r}\right)^2 J_2\left[5\left(\frac{z}{r}\right)^2 - 1\right]\right\} \tag{C.3}$$

$$a_{U_y} = -\frac{\mu}{r^3}y\left\{1 - \frac{3}{2}\left(\frac{R_m}{r}\right)^2 J_2\left[5\left(\frac{z}{r}\right)^2 - 1\right]\right\}, \tag{C.4}$$

$$a_{U_z} = -\frac{\mu}{r^3} z \left\{ 1 - \frac{3}{2} \left(\frac{R_m}{r} \right)^2 J_2 \left[5 \left(\frac{z}{r} \right)^2 - 3 \right] \right\}, \tag{C.5}$$

where μ is the Mars gravitational parameter, R_m is the Mars mean equatorial radius, J_2 is the Mars second zonal harmonic coefficient, and r is the radial distance of the spacecraft from the center of Mars.

The ballistic coefficient β is given by:

$$\beta = \frac{1}{2} \frac{C_D A}{M}, \tag{C.6}$$

where C_D is the drag coefficient, A is the spacecraft cross-sectional area, and M is the spacecraft mass.

The atmospheric density ρ is given by the exponential model:

$$\rho = \rho_0 \, e^{-\gamma \, (r - r_0)} \tag{C.7}$$

where ρ_0, γ, and r_0 are constant parameters associated with the exponential model.

The spacecraft velocity relative to the atmosphere v_{rel} is given by:

$$v_{rel} = \sqrt{a^2 + b^2 + c^2}, \tag{C.8}$$

where

$$a = \dot{x} + \omega_m y, \qquad b = \dot{y} - \omega_m x, \qquad c = \dot{z} \tag{C.9}$$

and where ω_m is the angular velocity of Mars, which is assumed to be aligned with the inertial z-axis.

The Jacobian of the dynamic model with respect to the state vector is then given by:

$$
\boldsymbol{A}(t) = \left.\frac{\partial \boldsymbol{F}(t)}{\partial \boldsymbol{X}(t)}\right|_{\boldsymbol{X}^*} =
\begin{bmatrix}
0 & 0 & 0 & 1 & 0 & 0 \\
0 & 0 & 0 & 0 & 1 & 0 \\
0 & 0 & 0 & 0 & 0 & 1 \\
A_{41} & A_{42} & A_{43} & A_{44} & A_{45} & A_{46} \\
A_{51} & A_{52} & A_{53} & A_{54} & A_{55} & A_{56} \\
A_{61} & A_{62} & A_{63} & A_{64} & A_{65} & A_{66}
\end{bmatrix}
\tag{C.10}
$$

where the components of the Jacobian are:

$$
A_{41} = \frac{a_{U_x}}{x} + \frac{\mu x^2}{r^5}\left[3 - \frac{15}{2}\left(\frac{R_m}{r}\right)^2 J_2\left(\frac{7z^2}{r^2} - 1\right)\right] + \beta\rho a\left(\frac{b\omega_m}{v_{rel}} + \frac{v_{rel}\gamma x}{r}\right)
$$

$$
A_{42} = \frac{\mu xy}{r^5}\left[3 - \frac{15}{2}\left(\frac{R_m}{r}\right)^2 J_2\left(\frac{7z^2}{r^2} - 1\right)\right] + \beta\rho\left(\frac{-a^2\omega_m}{v_{rel}} - v_{rel}\omega_m + \frac{v_{rel}\gamma a y}{r}\right)
$$

$$
A_{43} = \frac{\mu xz}{r^5}\left[3 - \frac{15}{2}\left(\frac{R_m}{r}\right)^2 J_2\left(\frac{7z^2}{r^2} - 1\right)\right] + \frac{\beta\rho v_{rel}\gamma a z}{r}
$$

$$
A_{44} = -\beta\rho\left(v_{rel} + \frac{a^2}{v_{rel}}\right)
$$

$$
A_{45} = -\frac{\beta\rho a b}{v_{rel}}
$$

$$
A_{46} = -\frac{\beta\rho a c}{v_{rel}}
$$

$$
A_{51} = \frac{\mu xy}{r^5}\left[3 - \frac{15}{2}\left(\frac{R_m}{r}\right)^2 J_2\left(\frac{7z^2}{r^2} - 1\right)\right] + \beta\rho\left(\frac{v_{rel}\gamma b x}{r} + \frac{\omega_m b^2}{v_{rel}} + v_{rel}\omega_m\right)
$$

191

$$A_{52} = \frac{a_{U_y}}{y} + \frac{\mu y^2}{r^5}\left[3 - \frac{15}{2}\left(\frac{R_m}{r}\right)^2 J_2\left(\frac{7z^2}{r^2} - 1\right)\right] + \beta\,\rho\,b\left(\frac{v_{rel}\,\gamma\,y}{r} - \frac{a\,\omega_m}{v_{rel}}\right)$$

$$A_{53} = \frac{\mu yz}{r^5}\left[3 - \frac{15}{2}\left(\frac{R_m}{r}\right)^2 J_2\left(\frac{7z^2}{r^2} - 1\right)\right] + \frac{\beta\,\rho\,v_{rel}\,\gamma\,b\,z}{r}$$

$$A_{54} = -\frac{\beta\,\rho\,a\,b}{v_{rel}}$$

$$A_{55} = -\beta\,\rho\left(v_{rel} + \frac{b^2}{v_{rel}}\right)$$

$$A_{56} = -\frac{\beta\,\rho\,b\,c}{v_{rel}}$$

$$A_{61} = \frac{\mu xz}{r^5}\left[3 - \frac{15}{2}\left(\frac{R_m}{r}\right)^2 J_2\left(\frac{7z^2}{r^2} - 3\right)\right] + \beta\,\rho\,c\left(\frac{v_{rel}\,\gamma\,x}{r} + \frac{b\,\omega_m}{v_{rel}}\right)$$

$$A_{62} = \frac{\mu yz}{r^5}\left[3 - \frac{15}{2}\left(\frac{R_m}{r}\right)^2 J_2\left(\frac{7z^2}{r^2} - 3\right)\right] + \beta\,\rho\,c\left(\frac{v_{rel}\,\gamma\,y}{r} - \frac{a\,\omega_m}{v_{rel}}\right)$$

$$A_{63} = \frac{a_{U_z}}{z} + \frac{\mu z^2}{r^5}\left[3 - \frac{15}{2}\left(\frac{R_m}{r}\right)^2 J_2\left(\frac{7z^2}{r^2} - 5\right)\right] + \frac{\beta\,\rho\,v_{rel}\,\gamma\,c\,z}{r}$$

$$A_{64} = -\frac{\beta\,\rho\,a\,c}{v_{rel}}$$

$$A_{65} = -\frac{\beta\,\rho\,b\,c}{v_{rel}}$$

$$A_{66} = -\beta\,\rho\left(v_{rel} + \frac{c^2}{v_{rel}}\right)$$

Bibliography

[1] Mars Program Pinpoint Landing System Study. Technical report, Jet Propulsion Laboratory, Pasadena, CA, 2003.

[2] Solar System Exploration. Technical Report JPL 400-1077, NASA Office of Space Sciences, May 2003.

[3] Mars Relay Description for Scout Proposals. Technical report, NASA Langley Research Center, Hampton, VA, April 2006.

[4] Charles H. Acton. Processing Onboard Optical Data for Planetary Approach Navigation. *Journal of Spacecraft and Rockets*, 9(10):746–750, 1972.

[5] Bradford Arnold. MRO Electra Navigation Service and Open Loop Recording Test Procedures. Technical Report TP 519138, Jet Propulsion Laboratory, Pasadena, CA, April 2004.

[6] Bradford Arnold. MSL Electra Lite Acquisition Test Procedure. Technical Report JPL D-35844 / MSL-656-1391, Jet Propulsion Laboratory, Pasadena, CA, January 2007.

[7] David J. Bell et al. Mars Network: A Mars Orbiting Communications and Navigation Satellite Constellation. In *IEEE Aerospace Conference Proceedings*, volume 7, Big Sky, MT, March 2000.

[8] Tim Brand et al. GN&C Technology Needed to Achieve Pinpoint Landing Accuracy at Mars. In *Proceedings of the AIAA/AAS Astrodynamics Specialist Conference and Exhibit*, number 2004-4748, Providence, RI, August 2004.

[9] Robert G. Brown and Patrick Y. C. Hwang. *Introduction to Random Signals and Applied Kalman Filtering*. Wiley, New York, third edition, 1997.

[10] P. Daniel Burkhart. Approach Navigation for the 2009 Mars Large Lander. In *Advances in the Astronautical Sciences*, volume 114, pages 2183–2198, San Diego, CA, 2003. Univelt.

[11] P. Daniel Burkhart et al. Real-Time EDL Navigation Performance using Spacecraft to Spacecraft Radiometric Data. In *Proceedings of the AIAA Guidance, Navigation, and Control Conference and Exhibit*, Keystone, CO, August 2006.

[12] A. Bruce Carlson. *Communication Systems*. McGraw Hill, New York, third edition, 1986.

[13] T. C. Duxbury, G. H. Born, and N. Jerath. Viewing Phobos and Deimos for Navigating Mariner 9. *Journal of Spacecraft and Rockets*, 11(4):215–222, April 1974.

[14] Thomas C. Duxbury and William G. Breckenridge. Mariner Mars 1969 Optical Approach Navigation. In *AIAA 8th Aerospace Sciences Meeting*,

number 1970-70, New York, January 1970.

[15] Karl T. Edquist. Afterbody Heating Predictions for a Mars Science Laboratory Entry Vehicle. In *Proceedings of the 38th AIAA Thermophysics Conference*, number 2005-4817, Toronto, Canada, June 2005.

[16] Todd A. Ely. Electra Two-Way Doppler Measurement Model including Error Budget. Interoffice Memorandum Electra-03-018, Jet Propulsion Laboratory, Pasadena, CA, January 2003. Revision 2.

[17] Todd A. Ely. Mars Network Radiometric Measurement Models and Data Interfaces for the Electra and CE-505 Radios. Interoffice Memorandum Electra-343K-****, Jet Propulsion Laboratory, Pasadena, CA, November 2005. Draft 2.

[18] Todd A. Ely et al. Strategies for Telecommunications and Navigation in Support of Mars Exploration. *Acta Astronautica*, 48:661–668, March 2001.

[19] Todd A. Ely et al. Real-Time Mars Approach Navigation aided by the Mars Network. In *Proceedings of the AIAA Guidance, Navigation, and Control Conference and Exhibit*, Keystone, CO, August 2006.

[20] Todd A. Ely and Joseph Guinn. Mars Approach Navigation using Mars Network-Based Doppler Tracking. In *Proceedings of the AIAA/AAS Astrodynamics Specialist Conference and Exhibit*, number 2002-4816, Monterey, CA, August 2002.

[21] Pasquale Esposito and Duane Roth. Mars Observer Orbit Determination Analysis. *Journal of Spacecraft and Rockets*, 28(5):530–535, October 1991.

[22] Yanming Feng. Applications of GPS in Space Programs . *GPS Solutions*, 6(1-2):126–127, November 2002.

[23] Floyd M. Gardner. *Phaselock Techniques.* Wiley, New York, third edition, 2005.

[24] Arthur Gelb. *Applied Optimal Estimation.* The M.I.T. Press, Cambridge, MA, 1974.

[25] Gaillet Guillaume. Preliminary Study of a Filter for a Precision Landing on Mars. Master Thesis, The University of Texas at Austin Center for Space Research, Austin, TX, 1997.

[26] T. W. Hamilton and W. G. Melbourne. Information Content of a Single Pass of Doppler Data from a Distant Spacecraft. Space Programs Summary 37-39, Vol. III, Jet Propulsion Laboratory, Pasadena, CA, May 1966.

[27] R. C. Hastrup et al. Mars Network for Enabling Low-Cost Missions. In *Acta Astronautica*, volume 52, pages 227–235. Elsevier, January 2003.

[28] Eugene B. Hogenauer. An Economical Class of Digital Filters for Decimation and Interpolation. *IEEE Transactions on Acoustics, Speech, and Signal Processing*, ASSP-29(2), April 1981.

[29] Greg N. Holt. Generalized Approach to Navigation of Spacecraft Formations using Multiple Sensors. Ph.D. Dissertation, The University of Texas at Austin, Austin, TX, August 2006.

[30] Ben Jai et al. The Mars Reconnaissance Orbiter Mission Operations: Architecture, Approach and Status. In *SpaceOps 2006 Conference*, number 2006-5956.

[31] Navin Jerath and Hiroshi Ohtakay. Mariner IX Optical Navigation Using Mars Lit Limb. *Journal of Spacecraft and Rockets*, 11(7):505–511, July 1974.

[32] P. H. Kallemeyn. EDL UHF Patch Antenna. Private communication, November 2005.

[33] Věnceslav F. Kroupa. *Phase Lock Loops and Frequency Synthesis*. Wiley, England, 2003.

[34] E. Glenn Lightsey et al. Expected Performance of the Electra Transceiver for Mars Missions. In *Proceedings of the AIAA Guidance, Navigation, and Control Conference and Exhibit*, San Francisco, CA, August 2005.

[35] William C. Lindsey. Optimal Design of One-Way and Two-Way Coherent Communication Links. *IEEE Transactions on Communication Technology*, Com-14(4):418–431, August 1966.

[36] Daniel T. Lyons. Mars Reconnaissance Orbiter: Aerobraking Reference Trajectory. In *Proceedings of the AIAA/AAS Astrodynamics Specialist Conference and Exhibit*, number 2002-4821, Monterey, CA, August 2002.

[37] Raman K. Mehra. On the Identification of Variances and Adaptive Kalman Filtering. *IEEE Transactions on Automatic Control*, AC-15(2):175–184, April 1970.

[38] Heinrich Meyer and Gerd Ascheid. *Synchronization in Digital Communications*, volume 1. Wiley, New York, 1990.

[39] Andreas E. Mogensen, Thomas Campbell, and E. Glenn Lightsey. Performance Analysis of the Tracking Loop Design of the Electra Transceiver. In *Proceedings of the Institute of Navigation National Technical Meeting*, Monterey, CA, January 2006.

[40] Andreas E. Mogensen and E. Glenn Lightsey. Tracking Loop Performance of the Electra UHF Transceiver. In *Proceedings of the AIAA Guidance, Navigation, and Control Conference and Exhibit*, Keystone, CO, August 2006.

[41] Douglas J. Mudgway. *Uplink-Downlink: A History of the Deep Space Network 1957-1997*. NASA History Series, Washington DC, 2001.

[42] Alan V. Oppenheim and Ronald W. Schafer. *Discrete-Time Signal Processing*. Prentice Hall, New Jersey, second edition, 1999.

[43] Elizabeth Quintanilla. Mars Final Approach, Entry, and Descent Navigation using the Mars Network. Master Thesis, The University of Texas at Austin, Austin, TX, December 2004.

[44] S. Ritter. An Optimum Phase Reference Detector for Fully Modulated Phase-Shift Keyed Signals. *IEEE Transactions on Aerospace and Electronic Systems*, AES-5(4):627–631, July 1969.

[45] Martin S. Roden. *Digital Communication Systems Design*. Prentice Hall, New Jersey, 1988.

[46] Ed Satorius. Contribution of Front-End PLL Electra Transceiver Phase Errors to the Two-Way Range Rate Error at UHF. Interoffice memorandum, Jet Propulsion Laboratory, Pasadena, CA, August 2001.

[47] Ed Satorius. Residual Carrier Modulation for the Electra Transceiver. Interoffice Memorandum Electra-01-009, Jet Propulsion Laboratory, Pasadena, CA, October 2001.

[48] Ed Satorius. Modulator Modifications for the Electra Transceiver. Interoffice Memorandum Electra-02-087, Jet Propulsion Laboratory, Pasadena, CA, October 2002.

[49] Ed Satorius. SNR and RSSI Analysis of Power Detector Data. Interoffice memorandum, Jet Propulsion Laboratory, Pasadena, CA, September 2003.

[50] Ed Satorius and Tom Jedrey. DTTL Lock Detector, SNR Estimator, and Viterbi Sync Detection. Interoffice memorandum, Jet Propulsion Laboratory, Pasadena, CA, April 2004.

[51] Ed Satorius and John Ye. Demodulator Modifications for the Electra Transceiver. Interoffice Memorandum Electra-02-089, Jet Propulsion Laboratory, Pasadena, CA, November 2002. Draft.

[52] Edgar H. Satorius, Zhong Ye, and Todd A. Ely. Carrier Acquisition and Tracking Requirements for Doppler Navigation. In *Aerospace Conference Proceedings*, volume 4, pages 1631–1638. IEEE, March 2003.

[53] Dan Simon. *Optimal State Estimation*. Wiley, New Jersey, 2006.

[54] M. K. Simon and S. Million. Residual Versus Suppressed-Carrier Coherent Communications. *Telecommunications and Data Acquisition Progress Report*, 127:1–9, November 1996.

[55] Marvin K. Simon and William C. Lindsey. Optimum Performance of Suppressed Carrier Receivers with Costas Loop Tracking. *IEEE Transactions on Communications*, Com-25(2):215–227, February 1977.

[56] J. Mark Steber. PSK Demodulation: Part 1. Technical Note 2, Watkins-Johnson Company, March - April 1984.

[57] John L. Stensby. *Phase-Locked Loops*. CRC Press, New York, 1997.

[58] Byron D. Tapley et al. The Gravity Recovery and Climate Experiment: Mission Overview and Early Results. *Geophysical Research Letters*, 31(9), May 2004.

[59] Catherine L. Thornton and James S. Border. *Radiometric Tracking Techniques for Deep Space Navigation*. JPL Deep Space Communications and Navigation Series. Wiley, New Jersey, 2003.

[60] Sam W. Thurman and Jeffrey A. Estefan. Mars Approach Navigation using Doppler and Range Measurements to Surface Beacons and Orbiting Spacecraft. In *Spaceflight Mechanics 1991; Proceedings of the 1st AAS/AIAA Annual Spaceflight Mechanics Meeting*, pages 227–247, Houston, TX, February 1991.

[61] Sam W. Thurman and Jeffrey A. Estefan. Doppler Navigation of Interplanetary Spacecraft using Different Data Processing Modes. *NASA STI/Recon Technical Report A*, 95, 1993.

[62] David A. Vallado. *Fundamentals of Astrodynamics and Applications*. McGraw Hill, New York, 1997.

[63] Fuqin Xiong. *Digital Modulation Techniques*. Artech House, Norwood, MA, 2000.

[64] John Ye and Edwin Grigorian. Electra Xilinx Functional and Interface Description. Interoffice Memorandum Electra-01-017, Jet Propulsion Laboratory, Pasadena, CA, March 2002.

[65] Rodger E. Ziemer and William H. Tranter. *Principles of Communications.* Wiley, New York, fifth edition, 2002.

Vita

Andreas Enevold Mogensen was born in Copenhagen, Denmark on November 2, 1976, the son of Jens H. Mogensen and Lisa C. Bjerregaard. He attended school in Denmark, Singapore, and California. After completing high school at Copenhagen International School in 1995, he attended Imperial College in London, where he graduated with a Master of Engineering degree in aeronautical engineering in 1999. While working on his thesis, he spent a semester at the Insituto Superior Téchnico in Lisbon, Portugal. After graduating, Andreas worked as a drilling services engineer for Schlumberger in the offshore oil industry in the Republic of Congo and Angola. In 2001, he began working as a control systems engineer at Vestas Wind Systems in Denmark. In 2003, he entered the Graduate School at The University of Texas at Austin, where he began working towards his Ph.D. in aerospace engineering. He has worked as a research assistant at the Center for Space Research while completing his studies.

Permanent address: Vintervej 7
DK-2920, Charlottenlund
Denmark

This dissertation was typeset with LaTeX[†] by the author.

[†]LaTeX is a document preparation system developed by Leslie Lamport as a special version of Donald Knuth's TeX Program.